
Master's Thesis

# "Determination of the chemical activity of components on ash layered bed materials"

carried out for the purpose to achieve the academic degree "Diplom-Ingenieur" (MSc.)

under the supervision of

Univ. Prof. Dipl.-Ing. Dr. techn. Hermann Hofbauer
Vienna University of Technology, Institute of Chemical Engineering, Vienna, Austria

and co-supervision of

Univ.Lektor. Dipl.-Ing. Dr.techn Matthias Kuba
BEST - Bioenergy and Sustainable Technologies GmbH, Graz, Austria

and

Prof. Dr. hab. Joanna Łojewska
Faculty of Chemistry, Jagiellonian University, Kraków, Poland

submitted at
"Technische Universität Wien", Faculty of Mechanical and Industrial Engineering
by

**Kouessan AZIABA**

Mat.Nr.: 01125202
Laudongasse 58/7
1080 Vienna
Austria

Vienna, December 2019

# Affidavit

I, Kouessan Aziaba, declare in lieu of an oath

1. that I am the sole author of this Master's thesis. I performed the associated research by myself, using only literature cited in this volume. I have not used any source or tool than those referenced.
2. that I have not prior to this date submitted this thesis as any examination in Austria or abroad.
3. that going to press of this thesis needs the confirmation of the examination committee.

Vienna, December 2019

Kouessan Aziaba

# Acknowledgment

First of all, I would like to thank Dr. Matthias Kuba, who gave me the opportunity of this work under his supervision. The research stay at the Jagellonian University in Krakow, Poland as a part of this work was enabled by his suggestions and cooperative work to a considerable extent. In particular, his highly developed expertise in combination with his interpersonal skills were always helpful and pathleading at the same time. Further, I would like to thank the research group BEST (Bioenergy and Sustainable Technologies, formerly Bioenergy 2020+) for the friendly integration into the working group. Thomas and Katharina were always very helpful with good suggestions for the improvement of my work, which I am very grateful for. I spent my time in the research laboratory in Krakow with Daniel. I would like to sincerely thank you for your balanced mix of professional impressions and the fun factor that is so important. I will keep those memories in mind with this tag (E2-38).

Furthermore, I would like to thank Prof. Hofbauer for the very good supervision. Not only his professional expertise, but also his interpersonal behavior was a high motivation for me to work with him.

The five weeks in Krakow were extremely valuable in my personal and professional development, which is also owed to Prof. Joanna Łojewska to an enormous extent. She and her team hosted us wonderfully which I am very grateful for. Especially, Damian was incredibly helpful in the measurements. Without his help significantly less results would have been obtained, for which I would like to thank him.

Special thanks also go to my fellow students Thomas, Stefan, Martin, Viktoria, Johannes, Christin, Ana-Rita and Laurin. The motivation to complete my studies was continuously sparked by them.

At this point, I would like to thank my friends. Many of them have been at my side for well over a decade now, but my new friendships are also inspiring to me. I am looking forward to see where this common path will take us.

My greatest gratitude is dedicated to my parents Amevi and Anani and also to my siblings, who supported me and believed in me in every situation in my life so far.

# Danksagung

Mein Dank gilt zunächst Dr. Matthias Kuba, welcher mir erst die Möglichkeit dieser Arbeit unter seiner Betreuung gab. Der Forschungsaufenthalt an der Jagellonen Universität in Krakau, Polen im Rahmen dieser Arbeit wurde zu einem erheblichen Anteil durch seine Vorschläge und Mitarbeit ermöglicht. Insbesondere sein sehr ausgeprägtes Fachwissen in Kombination mit seinen zwischenmenschlichen Kompetenzen waren stets hilfreich und zugleich richtungsweisend. Ein weiteres Dankeschön gilt der Forschungsgruppe BEST (Bioenergy and Sustainable Technologies, ehemals Bioenergy 2020+) für die freundliche Eingliederung in die Arbeitsgruppe. Thomas und Katharina waren dabei stets mit guten Verbesserungsvorschlägen sehr hilfreich. Dafür möchte ich mich ebenfalls bedanken. Meine Zeit im Forschungslabor in Krakau verbrachte ich mit Daniel. Ich möchte mich herzlich für seine ausgewogene Mischung aus fachlichen Eindrücken und auch dem dabei wichtigen Spaßfaktor bedanken.

Weiters möchte ich mich bei Prof. Hofbauer für die sehr gute Betreuung bedanken. Nicht nur seine fachliche Expertise, sondern auch sein zwischenmenschliches Auftreten waren für mich eine hohe Motivation für eine Zusammenarbeit mit ihm.

Die fünf Wochen in Krakau waren in meiner persönlichen und fachlichen Entwicklung äußerst wertvoll, was auch zu einem ebenfalls erheblichen Anteil Prof. Joanna Łojewska geschuldet ist. Sie und auch ihr Team nahmen uns wunderbar auf wofür ich sehr dankbar bin. Bei den Messungen war vor allem Damian unglaublich hilfreich. Ohne sein Zutun wären deutlich weniger Ergebnisse zustande gekommen wofür ich mich nochmals herzlich bedanken möchte.

Besonderer Dank gilt auch meinen Studienkollegen Thomas, Stefan, Martin, Viktoria, Johannes, Christin, Ana-Rita und Laurin. Die Motivation mein Studium abzuschließen wurde durch sie mitentfacht.

Meinen Freunden möchte ich auch an dieser Stelle meinen Dank aussprechen. Viele von euch sind schon seit deutlich mehr als einer Dekade an meiner Seite doch auch meine neuen Freundschaften sind für mich inspirierend. Ich freue mich darauf zu sehen wohin dieser gemeinsame Weg uns führen wird.

Meine größte Dankbarkeit gilt meinen Eltern Amevi und Anani und auch meinen Geschwistern, die mich in jeder bisherigen Lebenslage aufs Neue mit allem unterstützt und an mich geglaubt haben.

# Kurzfassung

Mit dem stetig steigenden Energiebedarf einer wachsenden Bevölkerung sind immer effizientere und nachhaltige Maßnahmen zur Energiegewinnung gefragt. Besonders in Hinblick auf die Herausforderung, eine durch fossile Brennstoffe induzierte globale Erwärmung des Klimas zu begrenzen, gewinnen jene Technologien an Bedeutung, die auf der Umsetzung von Biomasse basieren. Dabei nimmt die Vergasung von Biomasse neben der Verbrennung ebenfalls eine bedeutende Rolle ein. Die Vergasung von Biomasse bietet ein Produkt mit vielfältigen Anwendungsmöglichkeiten. Beispielsweise kommt das Produktgas bei der Synthese von Chemikalien und Treibstoffen sowie bei der Erzeugung von thermischer und elektrischer Energie zum Einsatz. Nachteilig auf die Qualität des Produktgases wirken sich im Rahmen der Biomassevergasung entstehende Teere die kostenintensiv kompensiert werden muss. Weiters birgt das Ascheschmelzverhalten eine ernst zu nehmende Herausforderung der Biomassevergasung, deren Lösung noch nicht vollständig geklärt ist und im schlimmsten Fall zum Erliegen des Vergasungsbetriebes führen kann.

Von zentraler Bedeutung bei einem Vergasungsprozess sind die Eigenschaften des eingesetzten Bettmaterials. Diese akkumulieren mit fortschreitendem Verlauf der Einsatzzeit Aschekomponenten, die sich in weiterer Folge zu Ascheschichten auf der Oberfläche der Partikel ausbilden, welche katalytisch aktive Eigenschaften in der Vergasung aufweisen. Diese begünstigen in weiterer Folge die Produktgasqualität.

Die beiden potentiellen Bettmaterialien Olivin als auch K-Feldspat wurden ungenutzt sowie nach ihrer Anwendung als Bettmaterial mit holzartiger Biomasse und Hühnermist mit spektroskopischen Analysemethoden auf ihre chemische Zusammensetzung, Struktur und Aktivität untersucht. Insbesondere die Untersuchung der Oberfläche mit Hilfe der Raman- und FT-IR Spektroskopie lässt auf Calziumoxid mit besonders dominanten Vorkommen schließen. Weitere Messungen unter einer kontrollierten Atmosphäre bei Temperaturen bis zu 500 °C wurden eingesetzt mit dem Ziel weitere Informationen chemischer Aktivität im Rahmen der Wasser-Gas-Shift Reaktion zu erlangen. Ebenso wurden einzelne Metalloxide der akkumulierten Ascheschicht auf aktive Zentren untersucht. Teilweise konnte eine Aktivität dieser festgestellt werden. Dies weist in weiterer Folge auf eine Aktivität der untersuchten Bettmaterialien hin.

# Abstract

With the increasing energy consumption of a growing population, more and more efficient and sustainable efforts are demanded to cover the global energy demand. In particular, the man-induced global warming of the climate poses a rising challenge to humankind. Thus, technologies that rely on the utilization of biomass are gaining importance. The gasification of biomass plays a central role alongside to combustion. The gasification of biomass offers a product with a variety of applications such as the synthesis of chemical compounds and, fuels as well as the generation of thermal and electric power. Nevertheless, the formation of tars in the context of biomass gasification is a serious drawback resulting in their costly removal from the product gas and the equipment. Further, the ash melting behavior poses serious challenges to biomass gasification, whose solution cannot yet be fully clarified. The worst-case scenario of the ash melting behavior involves the risk of an ultimate failure followed by the shut-down of the gasification operation.

The properties of the applied bed material within the gasifier have a major influence on the process. Bed materials accumulate ash layers which demonstrate increasing catalytically active properties during the gasification as the operating time progresses. These subsequently improve the product gas quality.

Both potential bed materials, olivine and, K-feldspar were applied during a gasification/combustion process with woody biomasses and chicken manure. Layered and non-layered fresh bed materials were analyzed with the focus on their chemical composition, structure and activity. Notably, the investigation of the surface with Raman and FT-IR spectroscopy suggests calcium oxide with particularly dominant occurrences. Further measurements under a controlled atmosphere of temperatures up to 500 °C were used to obtain further information on chemical activity in the context of the water-gas-shift reaction. Similarly, isolated metal oxides of the accumulated ash layer were investigated for active sites. Some modelled compounds revealed an activity. This, subsequently, indicates an activity of the examined bed materials.

# List of Abbreviations

| | |
|---|---|
| **ATR** | Attenuated total reflectance |
| **B8** | K-Feldspar bed-material with combusted Bark - 8h duration |
| **B32** | K-Feldspar bed-material with combusted Bark - 32h duration |
| **CM8** | K-Feldspar bed-material with combusted Chicken Manure – 8h duration |
| **DFB** | dual fluidized bed |
| **DRIFTS** | Diffuse Reflectance Fourier Transform Spectroscopy |
| **FB** | Fluidized bed |
| **FBC** | Fluidized bed combustion |
| **FBG** | Fluidized bed gasification |
| **FF** | Fresh K-feldspar |
| **FT-IR** | Fourier Transform Infrared Spectrometer |
| **MeOH** | Methanol |
| **K** | Potassium |
| **M8** | 70% B8 & 30% CM8 mixture |
| **M40** | 70% B40 & 30% CM40 mixture |
| **MS** | Mass Spectrometer |
| **m/z** | mass-to-charge ratio |
| **$NO_x$** | Nitrogen oxides |
| **OF** | Fresh olivine bed-material |
| **OU** | Olivine bed-material used in Fluidized Bed Combustion |
| **$SiO_4$** | Orthosilicate |
| **TPR** | Temperature-programmed reduction |
| **UV-VIS** | Ultraviolet-visible spectroscopy |

**WGS** Water-Gas-Shift

**XPS** X-ray photoelectron spectroscopy

**XRD** X-ray diffraction

**XRF** X-ray fluorescence

# Contents

# 1. Introduction

## 1.1. Motivation

The continuously rise of the world's population as well as emerging of non-industrialized economies are expected to continue the trend of an increasing global energy demand. The industrial sector reportedly contributes 50% of the global energy consumption, which is also forecasted to rise disproportionally strong. The consumption of the industrial sector of the EU-28 accounts for 25%. Even though the industrial energy demand has decreased by 25% since 1990, the total consumption has slightly risen by 2% recently. [24, 42]

However, this issue conflicts with a variety of problems, such as the increased exposure of particulate matter and the production of greenhouse gas emissions as a result of the utilization of fossil fuels. Especially, with regard to the anthropogenic change of climate followed by a series of impacts such as a concourse of droughts, heatwave induced fatalities, floods, harvest losses, forest fires, species extinctions, and economic losses a shift of the energy mix toward sustainable and renewable resources is demanded by a rising share of the population. Further, an expected future depletion of coal and oil reserves inherits the risk of economic and political conflicts. [7, 43] Biomass has been already used as an energy carrier since pre-industrial times and contributes about 7% of the EU-28 consumed energy today. [24]

The extraction of power and heat from biomass by direct combustion was outperformed and surpassed by fossil fuels and nuclear power to some extent. Therefore, different routes of biomass conversion are exploited to increase the utilizable energy output.

Alongside the conventional wood-burning furnace and grate combustion, biomass also offers the possibility of being processed in a gasifier. By having product gas as the yield of a gasifier, several routes of biorefinery processes are available. Furthermore, it is possible to implement gasification into a combined heat and power plant and is thus suitable for a zero-emission process. The co-generation of heat and power provides a significantly increased efficiency compared to the single production of electricity. [13]

Especially fluidized bed gasifiers offer a high flexibility in regard to the used fuel. The used fuels include coal, wood and woody fuels, wastes, and sludges. The operation of FBG is still efficient despite the considerable heterogeneity of biomass and their possibly substantial amounts of moisture and inorganic compounds. [46]

Challenges like the moisture content of the feedstock, a high energy demand, and an expensive gas-separation unit to extract the product gas from the $N_2$ environment were overcome by the introduction of the dual fluidized bed gasifier. It operates two connected fluidized bed reactors, which provide the flexibility to separate the gasification

and combustion reactions. The autothermal production of high-quality product gas becomes possible as a consequence. [46]

The gasification of biomass is consequently regarded as a highly promising and alternative to the gasification of fossil fuels. Thus, it may contribute to an increased share of the global energy consumption in future scenarios. At the same time, it is an effective route to face the current and upcoming challenges of climate change.

## 1.2. Previous Studies

The further development of the DFB was focused on problems arising from the ash content of biomass related to corrosion, slagging, fouling, and bed material agglomeration, finally leading to a shutdown of the operation. [70]

However, also positive effects of the process were observed arising from the ash content. Kirnbauer et al. [48] reported Ca-rich layers on olivine caused by biomass ash and bed material interaction. Ca-rich layers are associated with an elevated catalytic activity within the gasification process.

Research focusing on the water-gas shift reaction under the utilization of calcite, fresh, and layered olivine as bed materials was conducted. Calcite was revealed to yield CO conversions up to 61.5%, followed by used olivine which contribution is close to 50%. Fresh olivine was significantly lower with a CO conversion rate of less than 20%. [47]

More recent investigations revealed that K-feldspar and Quartz build up catalytically active layers as well during the thermochemical conversion of biomass. Also, a correlation between the activity and the amount of produced ash and the quality of ash was indicated. Another factor was the exposure time inside of the reactor. The layer formation processes of olivine, K-feldspar, and quartz were proposed. [37–39, 53, 88]

## 1.3. Target of this work

A better understanding of the layer-formation process and its impact on an enhanced gasification process is an abundant condition to make use of its advantage on an industrial scale. In regard to this target, this work focuses on a more detailed characterization of layered as well as non-layered bed materials, including a further identification of surface components of layered bed materials. The main focus is the ascertainment of the observed catalytic activity. For this purpose, a variety of analyses (TPR, UV-VIS, XRF, XRD, XPS, FT-IR, Raman) were deployed. Especially Raman and FT-IR were considered to have a high potential to deliver more specific information about molecular interactions between bed materials and gaseous phases. The significant advantage of Raman and FT-IR spectroscopy over other spectroscopic methods is the applicability during in situ conditions in combination with a comparably high offered content of information. In conclusion, the main targets of this work are:

- a further characterization of the ash components on layered bed materials regarding their molecular configuration
- a closer characterization of the catalytic activity of layered and non-layered bed materials in respect of the WGS reaction

Both objectives could have a positive long-term effect on biomass gasification processes.

# 2. Fundamentals

## 2.1. Biofuels

Biomass is a sustainable material originating from biological sources, including anthropogenic materials. Besides forestry, also residual-, agricultural-, industrial-, and municipal waste are common biomass sources. Biomass mainly contains cellulose (23 - 53%), lignin (10% - 33%) and hemicellulose (15% - 35%) as its main components. [17, 30, 63]

Cellulose $(C_6H_{10}O_5)_n$ is a linear long-chain polysaccharide-molecule residing in the cell walls of wooden fibers giving them their chemical durability. Cellulose itself consists of up to several thousand glucose molecules. They are connected within a compact, crystalline, and strong matrix by β-(1-4)-glycosidic bonds and hydrogen linkages. [17, 59, 78]

Lignin gives plant-based materials their mechanical and microbial resistance. It fills up the spaces between cellulose and hemicellulose within the fibers and is dominantly located in the outer layers. It consists of a complex three-dimensional phenol polymer composed out phenyl propionic alcohol such as coumaryl, coniferyl, and sinapyl alcohol. [17, 59, 78]

Hemicellulose is also a polysaccharide-molecule. In difference to cellulose, it is a heterogeneous amalgamation of pentoses (xylose, arabinose), hexoses (mannose, glucose, galactose), and uronic acids (glucuronic, methyl galacturonic and galacturonic acids). It serves a connecting piece unit between cellulose and lignin. Hemicellulose can occur as a branched component. The most abundant hemicellulose component is xylan. [30, 78]

A schematic overview of the main components of biomass and their chemical structure is portrayed in figure 2.1. Further, their interaction is illustrated.

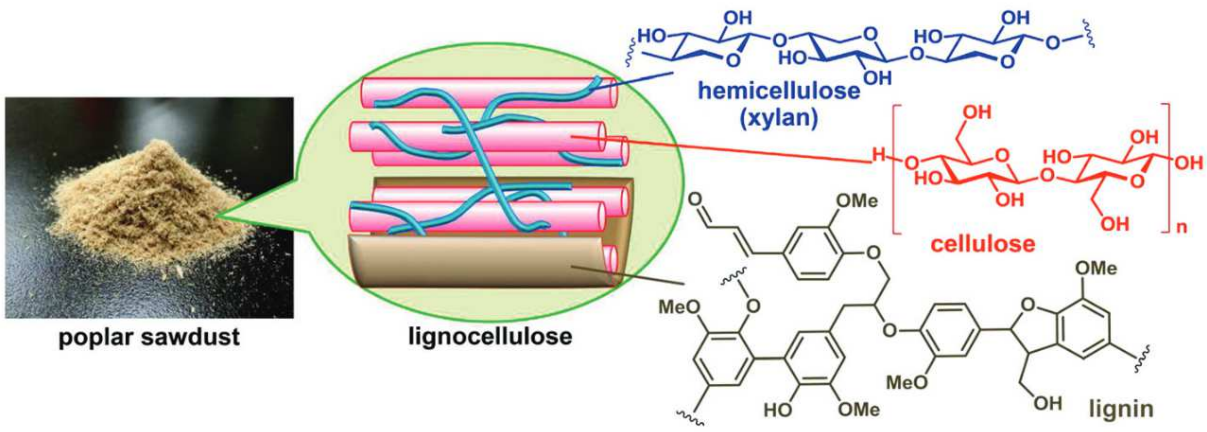


Figure 2.1.: Schematic overview of the main constituents of Biomass [40]

Further components of biomass are comparably low quantities of further organic but negligible materials (4%) and minerals consisting of Si, Ca, K, Mg, S, P, Fe, Mn, Al, and Na. Depending on the source, also organic pollutants and toxic inorganic compounds (wastewater sludge) as well as heavy metals are a component of biomass. [17, 78]

In terms of thermal stability, lignin is the by far most stable component. Because of its aromatic structure and interconnectedness, the provided temperatures must be comparably high to convert them into smaller hydrocarbons. A temperature range between 200 °C – 500 °C initiates the thermal degradation, which can exceed over 1000°C. A temperature range between 320 °C and 380 °C implies the pyrolytic degradation on cellulose. Hemicellulose is the thermally least stable component. An initial thermal degradation starts in a temperature range between 200 °C and 260 °C. [35]

Biofuels compromise unprocessed biomass as well as refinery products from biological origins. They are commonly divided into unprocessed primary biofuels and refined secondary biofuels. Literature reveals many routes to convert biomass into valuable energy carriers such as fermentation, transesterification, hydrolysis, gasification and pyrolysis. A further schematic classification of biofuels is portrayed in figure 2.2. [10, 65]

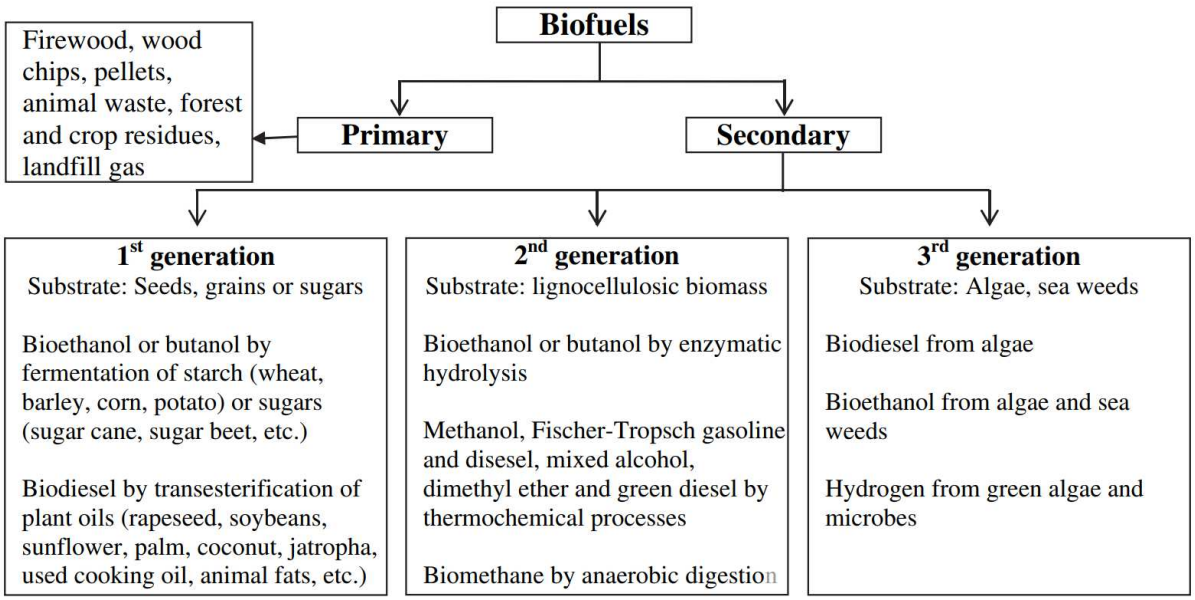


Figure 2.2.: Classification of Biofuels [65]

The operation of photosynthesis consumes $CO_2$ in order to grow plant products. Simultaneously, the application of biofuels releases the same quantities of $CO_2$ into the atmosphere. [17]

For the purpose of biomass evaluation, the proximate analysis was introduced. It breaks down biomass into fixed carbon, volatile matter, moisture, and ash as primary quality criteria. While moisture and ash cannot be used as energy carriers, fixed carbon and volatile matter are the combustible main contributors to the calorific value of biomass. [17]

Table 2.1.: Chemical ash composition in wt% of different biomass fuel types based on high-temperature ash analyses [83]

| Biomass [wt%] | $Al_2O_3$ | CaO | $Fe_2O_3$ | $K_2O$ | MgO | $SiO_2$ | $P_2O_5$ | $SO_3$ | Others |
|---|---|---|---|---|---|---|---|---|---|
| Beech bark | 0.12 | 68.20 | 1.10 | 2.60 | 11.50 | 12.40 | 2.30 | 0.80 | 0.98 |
| Birch bark | 0.55 | 69.06 | 2.24 | 8.99 | 5.92 | 4.38 | 4.13 | 2.75 | 1.98 |
| Forest residue | 2.99 | 47.55 | 1.42 | 10.23 | 7.20 | 20.65 | 1.42 | 2.91 | 5.63 |
| Oak wood | 4.27 | 15.56 | 4.20 | 31.99 | 5.92 | 29.93 | 1.90 | 3.84 | 2.39 |
| Hazelnut shells | 3.10 | 15.40 | 3.80 | 30.40 | 7.90 | 33.70 | 3.20 | 1.10 | 1.40 |
| Land clearing wood | 14.85 | 5.79 | 5.27 | 2.19 | 1.81 | 65.82 | 0.66 | 0.36 | 3.25 |
| Pine bark | 7.20 | 56.83 | 2.79 | 7.78 | 6.19 | 9.20 | 5.02 | 2.83 | 2.16 |
| Willow | 1.96 | 46.09 | 0.74 | 23.40 | 4.03 | 6.10 | 13.01 | 3.00 | 1.67 |
| Spruce bark | 0.68 | 72.39 | 1.90 | 7.22 | 4.97 | 6.13 | 2.69 | 1.88 | 2.14 |
| Spruce wood | 9.40 | 17.20 | 8.30 | 9.60 | 1.10 | 49.30 | 1.90 | 2.60 | 0.60 |
| Sawdust | 2.27 | 44.11 | 1.82 | 10.83 | 5.34 | 26.17 | 2.27 | 2.05 | 5.14 |
| Wood residue | 12.64 | 11.66 | 6.24 | 4.85 | 3.06 | 53.15 | 1.37 | 1.99 | 5.04 |
| Corn straw | 5.06 | 14.73 | 2.53 | 18.53 | 4.49 | 49.95 | 2.42 | 1.84 | 0.45 |
| Wheat straw | 1.54 | 8.21 | 0.88 | 24.89 | 2.74 | 50.35 | 3.54 | 4.24 | 3.61 |
| Sunflower husks | 8.75 | 15.31 | 4.27 | 28.53 | 7.33 | 23.66 | 7.13 | 4.07 | 0.95 |
| Chicken litter | 1.01 | 56.85 | 0.45 | 12.19 | 4.11 | 5.77 | 15.40 | 3.59 | 0.63 |
| Sewage sludge | 12.91 | 13.04 | 15.70 | 1.60 | 2.49 | 33.28 | 15.88 | 2.05 | 3.05 |
| minimum value | 0.12 | 5.79 | 0.45 | 1.60 | 1.10 | 4.38 | 0.66 | 0.36 | |
| mean value | 5.25 | 34.00 | 3.74 | 13.87 | 5.06 | 28.23 | 4.96 | 2.46 | |
| maximum value | 14.85 | 72.39 | 15.7 | 31.99 | 11.5 | 65.82 | 15.88 | 4.24 | |

## 2.2. Ash Components

The focus of this work was set on the interaction between ash forming components and bed materials during the application of thermochemical conversion. Common influences regarding thermal exposure will be specified. Depending on their activity and abundance, the major ash forming constituents are categorized as in the following.

### 2.2.1. Relative Abundance

Depending on the specific source, some ash components can have a wide relative abundance. Table 2.1 lists the most common biomass ash elements as oxides. As a brief remark it is pointed out that the elements Na, Mn, and Ti were neglected due to a comparably low abundance in biomass ash. In total, 17 biomass types were picked out of a variety of the most commonly used fuels in gasification plants. [2, 54, 73, 83]

Thus, it appears that CaO and $K_2O$ contribute significant proportions to biomass ash. Depending on the biomass fraction, also significant amounts of $SiO_2$ can be uttered. However, it is commonly counted as a minor constituent. Further minor constituents are $P_2O_5$, $Al_2O_3$, MgO, $Fe_2O_3$ and $SO_3$. This indication is merely averaged and highly dependent on the investigated biomass type. To the greatest extent, ash components exist as oxides. Nevertheless, also a considerable variety of organic and inorganic compounds are found

in biomass ash. [83]

Currently, the available information of ash forming components of biomass is quite limited. A determining factor for this is its highly variable composition, caused by miscellaneous growing conditions of the biomass. [83]

**Aluminium (Al)** mainly occurs as $Al_2O_3$. Its contribution to biomass ash varies from 0.12 - 14.85%. However, higher values exceeding 25% were also discovered in an investigation. It is presumed that a high $Al_2O_3$ content might be a direct consequence of the application of additives containing Al such as kaolinite within the paper production. $Al_2O_3$ can be applied in combination with $Fe_2O_3$ in order to improve the yield of the WGS reaction by an increase of the available surface area of $Fe_2O_3$. [9, 86]

**Calcium (Ca)** emerging as CaO commonly is a major ash component. Besides table 2.1 also other publications list CaO as a major biomass ash component. Especially wood, animal and, anthropogenic biomass show high CaO contents. The supply of hydroxyapatite as a fertilizer may cause increased CaO contents of biomass. Besides CaO, the chemical manifestations are highly diverse. [61,83] Alongside Vassilev et al. [85], higher Ca contents are associated with a higher ash fusion temperature. Magdiarz et al. [61] states that Ca combined with K and Si may form eutectics at lower temperatures.

**Iron (Fe)** emerging as $Fe_2O_3$ contributes a minor share to the composition of biomass ash. $Fe_2O_3$ can be transformed to $Fe_3O_4$ during the WGS reaction. $Fe_3O_4$ possesses a catalytic activity on the WGS reaction of biomass tar. Further, its application improves the $H_2$ and $CO_2$ contents of the product. [86] [9, 66]

**Potassium (K)** mainly occurring as $K_2O$ contributes a comparably large part to the biomass ash composition after CaO. Commonly herbaceous, agricultural, and animal biomass show high K contents. K fertilizers may be a reason which increases the $K_2O$ content to a greater extent. Increased K contents during thermochemical conversion applications are associated with significant drawbacks. Initially, decreased ash melting temperatures resulting in increased fouling and slagging rates are observed. Further, corrosion, increased amounts of aerosols, and particulate matter are significant drawbacks at the expense of the conversion process. [86] The transformation of K into the gaseous phase as KCl is also a reported issue. [25, 61, 85] . A further study reveals $K_2CO_3$ to have a catalytic activity during the steam gasification of biomass. [90]

**Magnesium (Mg)**, commonly occurring as MgO, has its largest appearances in woody, animal, and human biomass. MgO has been found to be active in tar-reforming reactions in cooperation with Fe and Ni catalysts. It is reported that MgO has a diminishing effect on K ash melting behavior alongside to CaO during gasification of biomass [21,50,86]

**Silicon's (Si)** contribution to the share of biomass ash is substantial. The largest contents can be found on contaminated, animal and human biomass ash. The most common compound is $SiO_2$, but also a variety of silicates are found. It is assumed that significant amounts of silicates that are observed in biomass ash are derived from the plant's uptake out of the soil. [84, 86]

**Phosphorus (P)** commonly emerges as $P_2O_5$ and various phosphates on a comparably lower scale. Significant contributions of P are observed in animal, human, herbaceous, and agricultural biomass. The application of hydroxyapatite or super triple phosphate as fertilizers is jointly responsible for increased abundances of P in biomass. P is associated with having a reverse effect of K by increasing the melting point of biomass ash mixtures. The formation of alkali phosphates results in a higher melting-point. Due to its limited availability, P is subject to several investigations that aim the recovery of P from biomass ash. [58, 80, 84, 86]

## 2.3. Thermochemical Conversion

Combustion, gasification and pyrolysis are the three major thermochemical conversion processes that are considered to take significant relevance among technical applications. All three combine the utilization of unspecific biomass or organic waste as a feedstock to yield high-valued hydrocarbons. [46]

The air/fuel ratio $\lambda$ is an essential parameter that gives a satisfying opportunity to divide the available processes apart. [46]

Combustion is an exothermic reaction characterized by complete oxidation of a fuel into its final thermodynamic stable product. A stoichiometric excess of air ($\lambda \geq 1$) leads to a comparably higher amount of oxidative agent. The desired primary yield of this process is heat. [46]

Gasification is the hypo stoichiometric ($0 < \lambda < 1$) energy demanding conversion of solid fuels into gaseous fuels. It requires a gasifying agent that contains oxygen. Therefore, Air, $CO_2$ and $H_2O$ can be used. [46]

Pyrolysis converts organic feedstocks in absence of air ($\lambda = 0$) in order to achieve gaseous, liquid, and solid fuels. This process is entirely endothermic and causes degradations of the molecular structure of hydrocarbons. [46] Torrefaction is a mild variant of slow pyrolysis to remove the moisture and other volatiles. [20]

A schematic overview of the three conversion processes is portrayed in figure 2.3. A classic combustion process initially evaporates volatiles and degrades hydrocarbons into molecular fragments. Depending on the air/fuel ratio, the intermediate product will be gasified or combusted in the following. [46]

### 2.3.1. Combustion

Approximately 11% of the global primary energy is provided by the combustion of biomass. Its main purposes are found in daily heat consumption, district heating applications, and in combined heat and power plants (CHP). A schematic overview of the main purposes

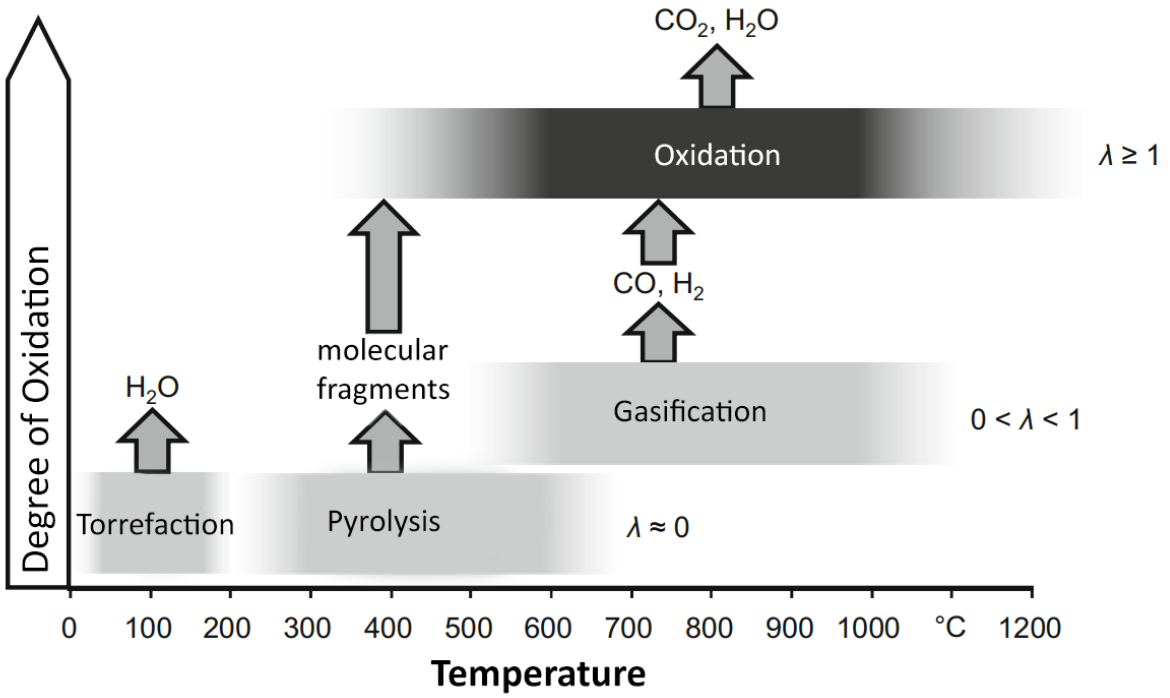


Figure 2.3.: Schematic overview of the demanded air/ratios and operating temperature ranges in dependence of the degree of oxidation of thermochemical conversion processes (translated) [46]

of combustion is portrayed in figure 2.4. [56]

The combustion is an exothermic complete oxidation of the fuel. The released thermal energy covers the endothermic consumption of the pyrolysis and gasification which occur simultaneously. In order to provide optimal conditions for the oxidation reaction, three more criteria must be fulfilled:

- Time: sufficient time to achieve complete oxidation
- Temperature: sufficient oxidation temperature
- Turbulence: a good mixture of the oxidant and the fuel

Both heterogeneous and homogeneous oxidations occur during combustion. Solid carbon particles get partially oxidized to CO or directly to $CO_2$ in the firebed with oxygen. The homogeneous oxidation takes place as soon as the gaseous products of the prior gasification and pyrolysis part get in contact with oxygen. CO will be further oxidized to $CO_2$, and hydrocarbon molecules end up being entirely degraded to $CO_2$ and $H_2O$. The variety of oxidation reactions are described in the equations (2.1) - (2.6). The given enthalpy of reaction $\Delta H_{R,T[K]}$ is given for a temperature of 298 and 1123K. [46]

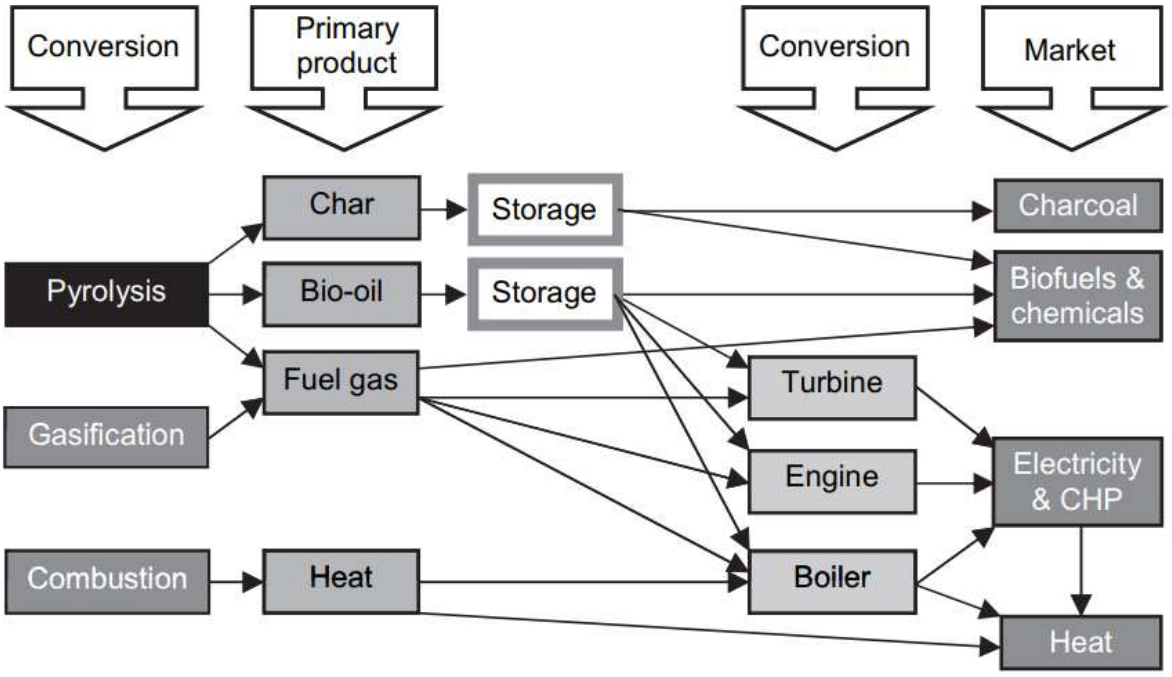


Figure 2.4.: Products and purposes of thermochemical biomass conversion [13]

$$heterogeneous\ reactions\ (solid-gas): \qquad \Delta H_{R,298}/\Delta H_{R,1123}$$

$$C + O_2 \rightarrow CO_2 \qquad -393.4/-394.4 \qquad (2.1)$$

$$C + \frac{1}{2}O_2 \rightarrow CO \qquad -110.5/-87.6 \qquad (2.2)$$

$$homogeneous\ reactions\ (gas-gas):$$

$$CO + \frac{1}{2}O_2 \rightarrow CO_2 \qquad -282.9/-366.8 \qquad (2.3)$$

$$H_2 + \frac{1}{2}O_2 \rightarrow H_2O \qquad -241.8/-224.1 \qquad (2.4)$$

$$CH_4 + 2O_2 \leftrightarrow CO_2 + 2H_2O \qquad -808.2/-801.0 \qquad (2.5)$$

$$C_mH_n + \left(m + \frac{n}{4}\right)O_2 \rightarrow mCO_2 + \frac{1}{2}nH_2O \qquad (2.6)$$

The velocity of the combustion is another essential parameter that has to be regarded. The kinetics of the oxidation reactions are highly dependent on the temperature. Until about 600°C, the supply of oxygen is just sufficient in order to maintain the reaction. Beginning from 600 °C, diffusion forces determine the rate of the oxidation in the boundary layer of the solid particle. The actual reaction takes place in the pore of the solid particle which is followed by the diffusion of the product out of the boundary layer. [46]

### 2.3.2. Gasification

Gasification was initialized in order to transform organic wastes, low-priced or negative-value feedstocks into more valuable chemicals. Some obtainable products are product-gas, alcohols, and phenolics. The moisture content is a significant drawback of combustion. However, the effect of a high moisture content is comparably lower on gasification applications than on combustion. As a side effect the landfill of solid wastes, $CH_4$ emission and groundwater contamination were reduced. A schematic overview of the main purposes of gasification is portrayed in figure 2.4 [46, 56]

The main factor for the gasification process is the available oxygen content, which is operated under a hypo stoichiometric fuel/air ratio. The application of oxygen containing gasification agents like air, $CO_2$, steam or even pure oxygen is mandatory. Depending on the gasification agent, a considerable variety of heterogeneous as well as homogeneous reactions take place. Alongside the oxidation reactions in the equations (2.1) - (2.6), the following major reactions also occur. [46, 68]

$$heterogeneous\ reactions\ (solid-gas): \qquad \Delta H_{R,298}/\Delta H_{R,1123}$$

$$C + H_2O \rightarrow CO + H_2 \qquad +131.3/+135.7 \tag{2.7}$$

$$C + CO_2 \rightarrow 2CO \qquad +172.4/169.4 \tag{2.8}$$

$$homogeneous\ reactions\ (gas-gas):$$

$$CO + H_2O \rightarrow CO_2 + H_2 \qquad -41.2/-33.6 \tag{2.9}$$

$$CH_4 + H_2O \leftrightarrow CO + 3H_2 \qquad +206.2/+226.8 \tag{2.10}$$

$$CH_4 + CO_2 \leftrightarrow 2CO + 2H_2 \qquad +247.3/+260.4 \tag{2.11}$$

$$C_mH_n + mH_2O \rightarrow mCO + \left(m + \frac{1}{2}n\right)\ H_2 \tag{2.12}$$

Following the reactions, it can be anticipated that the gasification agent directly influences the thermal balance of the gasification. The application of air and pure oxygen leads to more exothermic reactions. Following this, the gasification runs autothermal in this case. However, the thermal losses which come with the $N_2$ content must be considered as a drawback. $CO_2$, as well as steam, have a positive enthalpy of reaction in aggregate but the operation with them must be thermally supported. [46, 68]

Another essential impact of the used gasification agent can be discovered on the emerging products. While the application of pure oxygen results in the formation of steam and mainly $CO_2$, the utilization of air can result in the formation of $NO_x$. However, the utilized fuel also releases nitrogen-compounds ($NH_3 > 50\%$) depending on the temperature and pressure in the gasifier. The application of Steam or $CO_2$ results in the formation of $CO_2$ and the product gas components $H_2$ and CO. The conversion of tar is a further result of the application of steam as a gasifying agent. Tar is transformed into light hydrocarbons in the presence of steam, catalysts and high temperatures (>800°). [46, 68]

The kinetic properties of the gasification are determined by the transport of the gasification agent to the surface of the solid fuel particle. Driven by diffusion forces, the particle migrates through the boundary layer into the pore of the particles where the actual reaction takes place. The newly formed product diffuses out of the pore and consequently leaves the boundary layer of the solid particle. [46]

### 2.3.3. Pyrolysis

Finally, pyrolysis is the thermochemical treatment of organic materials like waste or biomass in a total absence of oxygen. It mainly delivers liquid, but also gaseous and solid fuels depending on the temperature and residence time. The main advantage of the liquid product lies in its straightforward storability. Elevated temperatures imply a row of decomposition reactions of high or medium length hydrocarbons into short length hydrocarbons. A schematic overview of the main purposes of pyrolysis is portrayed in figure 2.4 [35]

The pyrolytic degradation of biomass is given by the following equation [68]:

$$\overbrace{(CH_2)_x}^{Biomass} + \Delta H \rightarrow yCO + wCO_2 + \overbrace{(CH_2)_u}^{Char} + \overbrace{vCH_4}^{Biogases} + zH_2 \tag{2.13}$$

Its main purpose is the precipitation of moisture and other volatiles, the production of charcoal, and particularly the production of bio-oil as a liquid product. Bio-oil can serve as a valuable parent substance such as for phenol in the resins industry, for the pharmaceutical industry, fiber synthesis, fertilizing industry, and flavoring agents. [20] Likewise, the depolymerization of synthetic material for the recovery of monomers is applied on a lab-scale. [11, 71]

The composition of the feedstock extensively determines the obtained yield. Besides the

temperature and pressure, the yield is significantly determined by the heating rate and the residence time of the feedstock. [1]

- The application of slow pyrolysis treats the feedstock with lower temperature ranging up to about 400 °C by utilizing slow heating rates. The residence times vary between several hours up to several days. The majority of the product is solid while up to 35 wt.% gas and 30 wt.% liquid can be obtained. It can be assumed that the evaporated products mainly consist of moisture. Further products are obtained due to the light decomposition of the biomass structure. Slow pyrolysis is considered to serve as a production technique for activated carbon. [13, 20]

- For the purpose of bio-oil production fast pyrolysis gains more and more relevance today. A high heat-transfer-rate is combined with a brief residence time (< 2 seconds) are applied. The temperature ranges between 400 – 600 °C. The majority of the yield consists of liquid and gaseous products. However, the feedstock has to be grinded into small particles in order to increase the heat transfer. [18]

## 2.4. Applied Gasifier Types

Biomass is a very heterogeneous fuel compared to conventional fossil fuels. Thus, it is challenging to provide ideal conditions for an ideal conversion. Depending on the types of gasified biomass, mass- and heat transfer Kaltschmitt et al. introduced an appropriate classification of gasifiers. [46]

### 2.4.1. Fixed bed Gasifier

Fixed bed gasifiers expose the gasifying agent to a fuel that is located on a permeable layer of bed material or fuel. The gas stream of the gasifying agent is not able to elevate the fuel with slow flow rates. The fuel will be decomposed while it moves from the top, where it is usually submitted to the bottom. The specific design of the reactor determines where the actuals decomposition of the fuel occurs. Two different designs of fixed bed reactors will be introduced in the following [46]:

**Updraft Gasifier** The updraft gasifier is the oldest design that is still in operation. The fuel is submitted at the top, where it moves downwards due to gravity. The inlet for the gasifying agent is on the bottom of the reactor. It flows counter currently towards the fuel. As the first step, the sinking particle enters the drying zone where moisture is removed. The gasifying agent leaves the reactor here on lower temperatures between 100°C and 200°C. In the following, further volatiles are removed from the particle, leaving char behind which proceeds to the reduction zone. The reduction zone is a part of the actual gasifying zone where CO, $CH_4$ and $H_2$ are produced. Finally, the residuals of the fuel reach the oxidation zone, where it gets entirely oxidized to complete the gasifying zone. The last step delivers the necessary energy demand for the full gasification process.

A schematic cross-section of the described reaction zones is portrayed in figure 2.5. [46,60]

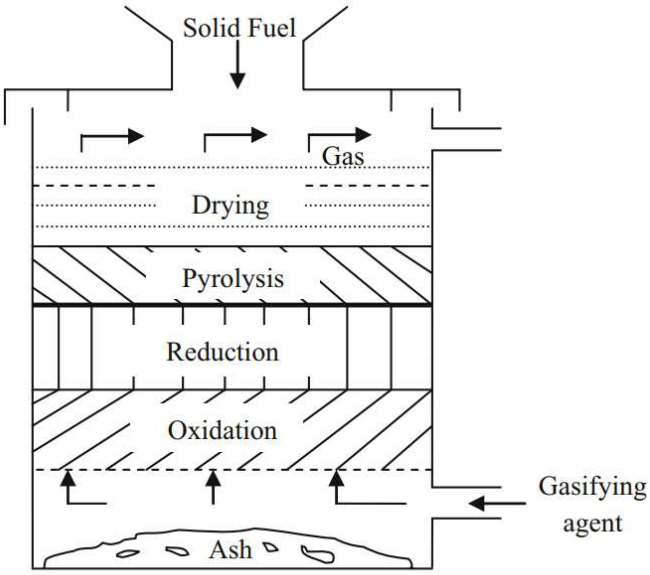


Figure 2.5.: Schematic cross-section of an updraft gasifier [60]

A significant advantage of the updraft gasifier is a high thermal efficiency coupled with comparably low demanded expenses for the preparation of the fuel. Unfortunately, the design of the process does not promote the internally produced tar to pass the reduction zone. This results in a high tar output compared to the downdraft gasifier. Further advantages and drawbacks are listed in table 2.2 [46]

Table 2.2.: A comparison between the advantages and drawbacks of an updraft gasifier [46, 56]

| Advantages | Drawbacks |
|---|---|
| + counter-current flow induces efficient heat transfer | − tar output |
| + low pressure drops | − limited scale-up opportunities |
| + suitable for small-scale applications | − high moisture content in product gas |
| + insensitive to high moisture contents of the fuel (<60%) | − char removal difficulties |
| + can handle coarse fuel particles (2 – 20 cm) | − long residence time |
| + simple and inexpensive process | |
| + low particulate matter in product gas | |

**Downdraft Gasifier** The characteristic difference to the updraft gasifier is the flow direction of the gasifying agent. In this case, it flows collectively with the fuel towards the bottom of the gasifier. Initially, the fuel passes the drying zone, followed by the pyrolysis zone, where tar containing volatiles and char are formed. The gasifying agent carries the char in combination with the formerly produced volatiles into the oxidation zone. As soon

as the char arrives in the oxidation zone, the exothermic reaction takes place by partially cracking down long-chain hydrocarbons and volatiles. This cracking process generates temperatures exceeding 1000°C. Finally, the residual volatiles will be reduced by the char forming CO out of $CO_2$. A schematic overview is portrayed in figure 2.6. [46, 60]

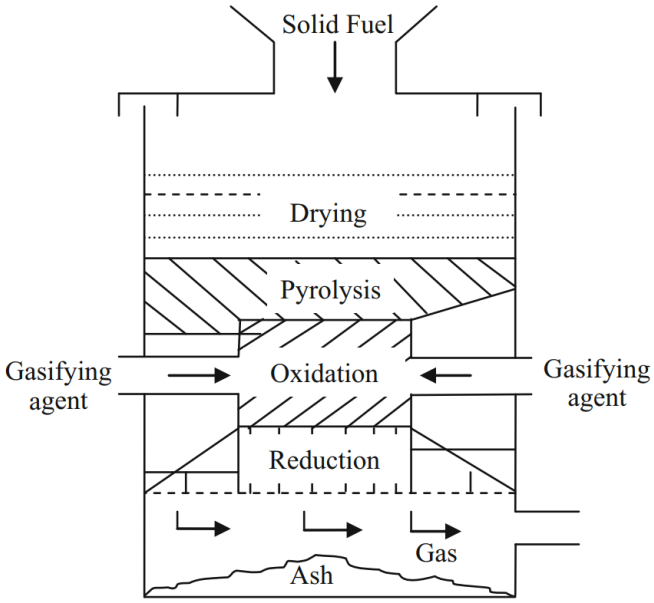


Figure 2.6.: Schematic cross-section of a downdraft gasifier [60]

Notably, the downdraft gasifier delivers a product gas with temperatures between 600 up to 800 °C. It is commonly used to preheat the gasifying agent up to 300 – 400 °C. Nevertheless, the overall efficiency is inferior to the updraft gasifiers. A further comparison of advantages and drawbacks is listed in table 2.3 [46, 60]

Table 2.3.: A comparison between the advantages and drawbacks of a downdraft gasifier [46, 56, 60]

| Advantages | Drawbacks |
|---|---|
| + high quality product gas with low soot, ash and tar contents | – fuel particle size dependency |
| + increased controllability opportunities over downdraft gasifier | – moisture content of the fuel must remain under 20% |
| + less gas cleaning efforts mandatory | – less thermal efficiency |
| + simple and low-cost process | – heat recovery system necessary |
| + low particulate matter and ash content in product gas | – ash melting behavior |
| | – limited scale-up opportunities |

### 2.4.2. Fluidized bed Gasifier

Fluidized bed gasifiers are designed with bed materials such as quartz sand or olivine, which is located on a distributor plate over the flow path of the gasifying agent. Ordinarily, the fuel is initially grinded down to small particles, submitted to the reactor by a spiral conveyor, and further mixed up within the bed material. This provides favorable heat transfer conditions. Contrary to the fixed bed gasifier, all stages of thermochemical conversion occur simultaneously, distributed all over the reactor. The average temperature of the reactor ranges between 700 – 900 °C. The pressure can vary from a vacuum up to 70 bar. According to the velocity of the gasifying agent, fluidized bed gasifiers are classified into bubbling fluidized bed (1 – 2 m/s) and circulating fluidized bed (5 – 10 m/s) gasifiers. In general, fluidized bed gasifiers are considered to offer a better controllability of reaction conditions than fixed bed gasifiers. Figure 2.7 portrays a scheme of both designs. [46, 60]

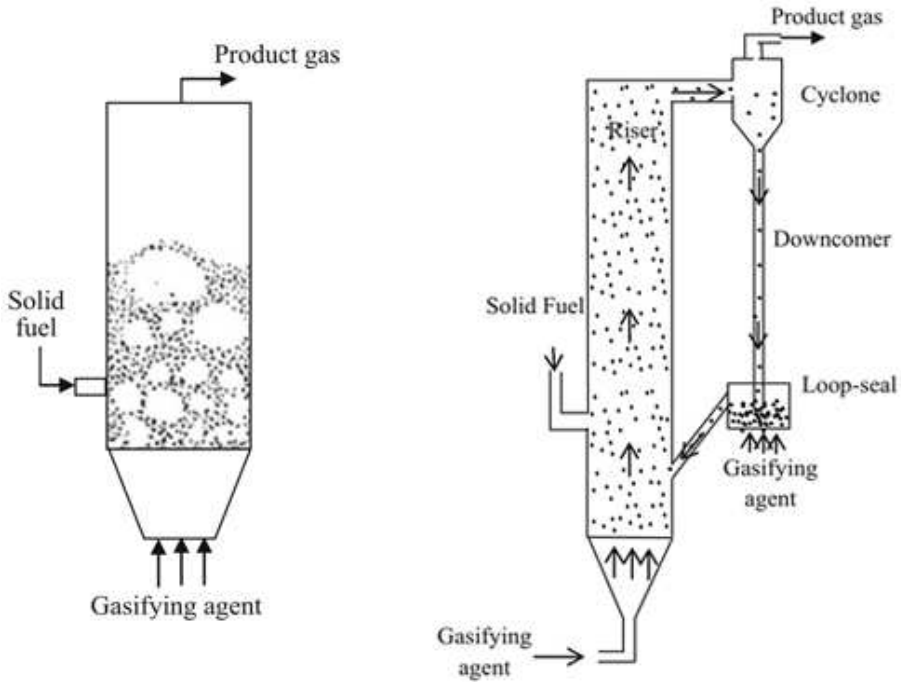


Figure 2.7.: Comparison of a bubbling fluidized bed (left) and a circulating fluidized bed reactor design (adapted from [60])

It can be observed that the design of the bubbling fluidized bed gasifier excludes several units that can be found on typical circulating fluidized bed equipment. The primary criterion to maintain the state of a bubbling fluidized bed is the velocity of the gasifying agent. Different velocities will result in different grades of fluidization. Thus, the main request is to maintain the velocity between the minimum fluidization and just under a velocity which would entrain particles and bed materials out of the reactor. As a result, a floating surface containing fuel and bed material is formed. In this respect, the comparable simple design of the bubbling fluidized bed is reasonable. [46, 60]

The circulating fluidized bed gasifier operates with high gasifying agent velocities on purpose. Therefore, fuel and bed material are distributed all over the reactor irregularly.

Particles, as well as bed material, get entrained by the gasifying agent. This results in the necessity of a cyclone in order to separate the gaseous from the solid phase. The solid particles are resubmitted to the reactor through a loop-seal after passing the cyclone. The separated gas after the cyclone contains product gas. [46, 60]

Table 2.4.: A comparison between the advantages of bubbling and circulating fluidized bed gasifier [46, 56, 60]

| Advantages | Drawbacks |
|---|---|
| + homogeneous temperature distribution | − effortful setup (CFB) |
| + high heat transfer rates | − limited ability to handle moisture in fuel (BFB) |
| + less tar and unconverted hydrocarbon contents | − high energy demands (CFB) |
| + brief residence times | − gas bypassing due to bubble formation (BFB) |
| + good controllability of the process | − abrasive effect due to high gas velocities (CFB) |
| + scale-up | − product gas diluted in gasifying agent |
| + very high output (CFB) | |
| + low quality demands on fuel | |

**Dual Fluidized Bed Gasifier.** The basic principle of a DFB gasification system is the separation of a single reactor environment into two independent reactors. Thus, the reactors can be operated as BFB, CFB, or both simultaneously. Consequently, the flexibility to cope with various operating conditions increases which allows the production of $N_2$-free product gas without a gas separation unit. A schematic illustration of the working principle is portrayed in figure 2.8. It is adapted from a DFB gasifier in Güssing, Austria, which was scientifically exploited by the Technical University in Vienna. [46, 60]

The fuel was submitted into the gasification reactor, which was operating as a BFB reactor. The temperature was ranging between 800 and 850 °C. The gasification reactor is the component where the biomass is transformed into the product gas. Meanwhile, the bed material particles, as well as the residual char particles, slip down into the combustion reactor via a chute. In the following, the submitted char is fully combusted in the presence of the bed material, which will be transferred back to the gasification reactor through a loop seal. [46, 52, 60]

The hot flue gas leaves the reactor in a cyclone following the combustion reactor. The hot bed material provides the necessary thermal energy in order to conduct the gasification reactions. Therefore, the whole process can be regarded as autothermal. The loop seal is used to lock air out of the gasification reactor. Additional steam keeps the solid components of the loop seal fluidized. Gaseous components inside of the loop seal get lifted up towards the cyclone as a result of the steam flow, while solid particles remain fluidized. [46, 52]

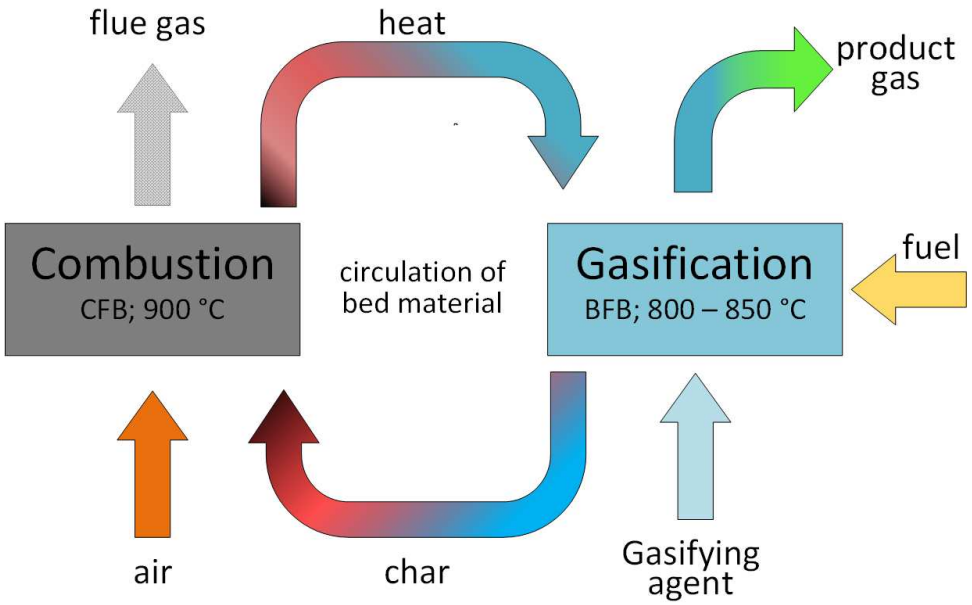


Figure 2.8.: Schematic working principle of a dual fluidized bed gasifier (adapted from [46, 52])

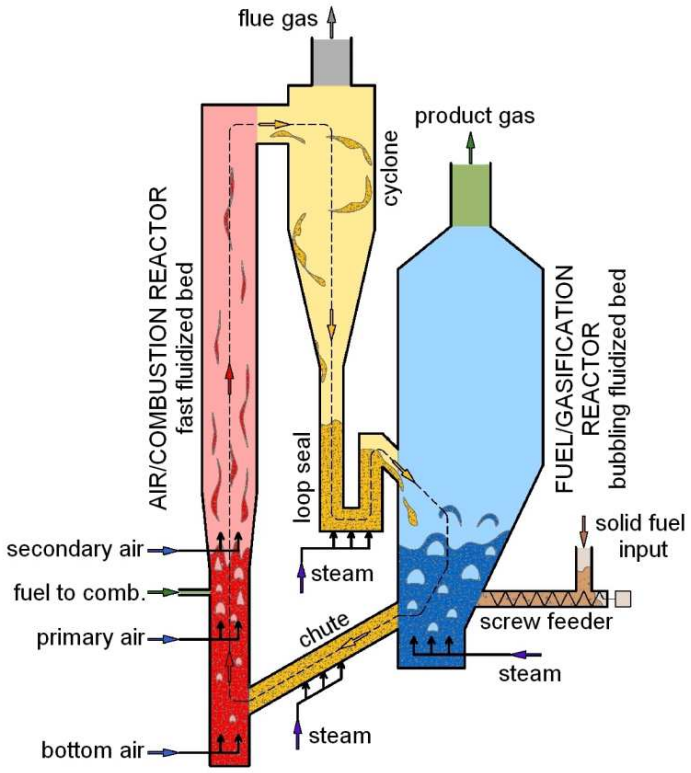


Figure 2.9.: Schematic illustration of the DFB reactor [36]

### 2.4.3. Entrained flow gasifiers

Entrained flow gasifiers operate in a co-current setup on very high temperatures (1200 – 2000°C) and residence times of just a couple of seconds. The velocity of the gasifying agent surpasses the conditions on fluidized bed reactors. Commonly, oxygen is used as a gasifying agent. However, also air can be used. The fuel must be submitted as finely grinded fuel or as a pyrolytic product. This setup allows a full gasification within the reactor. Very high temperature levels keep the tar formation low. Slagging of ash components is handled by its removal as a liquid phase. Entrained flow gasifiers handle large workloads, providing almost complete conversion rates and high-quality product gas. However, entrained flow reactors face some drawbacks such as a costly operation induced by enormous thermal energy demands, considerable gasifying agent streams, intensive required pre-treating of the fuel, and the formation of sulfur or chlorine-containing acids. The removal of ash in a liquid state is also effortful. Figure 2.10 portrays a schematic illustration of the entrained flow gasifier. [46, 56, 60]

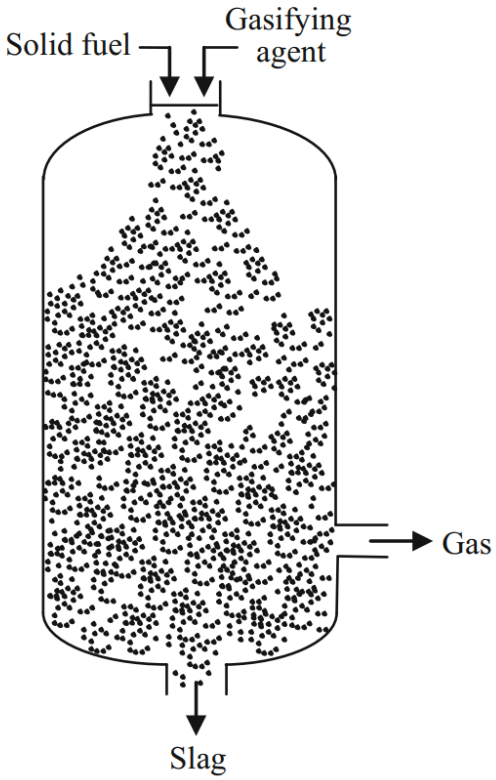


Figure 2.10.: Schematic cross-section of a downdraft entrained flow gasifier [60]

## 2.5. Applied Industrial Catalysts

The performance of a reaction is a function of the kinematic and thermodynamic conditions. The kinematic factor of a reaction is highly dependent on the temperature. Equation (2.14) is commonly referred to as the expression of Arrhenius. It provides

a mathematic relation for surface reactions between the reaction rate constant $k$, pre-exponential factor $A$, activation energy $E_a$, universal gas constant R and temperature $T$. [51]

$$k = Ae^{\frac{-E_a}{(RT)}} \tag{2.14}$$

However, in gasification, high temperatures are related to several issues such as high costs, formation of $NO_x$, $SO_x$, slagging, and possibly unsuitable thermodynamic conditions.

Alternatively, a catalyst can enhance the kinematic conditions and the selectivity of desired reactions. As a result, the reaction rates rise without affecting the thermodynamic conditions of the reaction. A heterogeneous catalyst participates in a gas-phase reaction without being consumed in a periodical manner. It breaks or undermines the intramolecular bonding power of its gaseous reactants. As the next step the adsorbed species react with each other. This step can comprise several intermediate reactions. Finally, the product gets released from the catalyst, recovering its site to conduct the next reaction. The overall demanded activation energy decreases due to this mechanism significantly. [4,64,82]

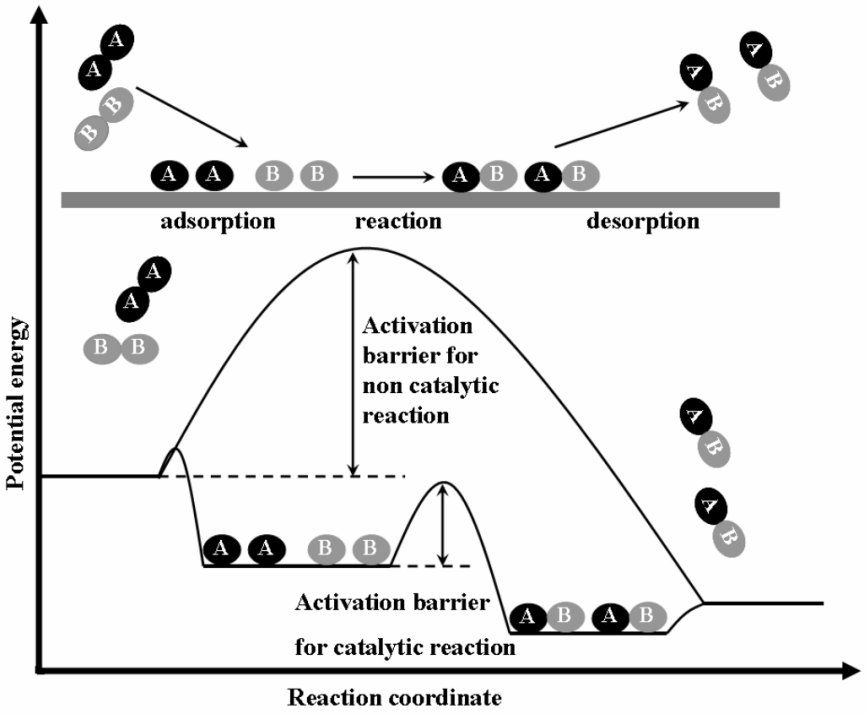


Figure 2.11.: Schematic illustration of a non-catalytic and a heterogeneous catalytic potential diagram [4]

## 2.6. Bed Material Type

Bed Materials provide an appropriate distribution of feedstock particles and offer stable thermodynamic conditions in the reactor. The heat-transfer roughly occurs due to gas- as well as particle convection and thermal radiation [79]. Commonly, bed material does not take part in the reactions themselves. However, some bed materials offer capabilities to act contrary to several consecutive incidents like defluidization followed by bed agglomeration and tar formation. A catalytic activity has also been reported. On the opposite, some bed materials are costly or contain inconvenient components. In order to identify the best match between the operation of the reactor, costs, and substance-based properties, olivine, as well as K-feldspar, are described in further detail in the following. The description focuses on its chemical composition and structures. Further, also the proposed layer formation processes during the utilization in the reactor are described. [48, 74, 79]

### 2.6.1. Olivine

The olivine mineral group $(Mg,Fe,Mn,Ni)_2[SiO_4]$ is a main constituent of the earth's upper mantle. Some sources report a high probability for olivine to be the most common mineral below the earth's crust. [34] However, the deposits in the earth's crust reach approx. 3 Vol.-%. They commonly appear as inclusions in basaltic rocks and as a component in Peridotites. Among the Peridotites, Dunite nearly consists of pure olivine, followed by Harzburgite, Wehrlite, and Lherzolite with lower shares of olivine. [67]

Olivine belongs to the group of Orthosilicates, which are also commonly referred to as Nesosilicates. The crystal structure is formed by a $Si^{4+}$ surrounded by $O^{2-}$ ions forming a tetrahedron with shared electrons. Each $O^{2-}$ ion is connected to a cation forming the minerals lattice similar to a hexagonal close-packed arrangement. [34, 67]

The olivine mineral itself is commonly referred to as a mixture of the two endmembers Forsterite ($Mg_2SiO_4$) and Fayalite ($Fe_2SiO_4$). The proportion between Mg and Fe regarding the size is comparable. They form solid solutions without any miscibility gaps and commonly occur as a mixture where Forsterite dominates the crystal with 70 – 90 mol.-%. It has a Mohs hardness of 6.5 – 7 and a density between 3.2 up to 4.3 g/cm$^3$. [34, 67]

An oxygen-rich environment can be a driving factor of $Fe^{2+}$ in the lattice to be reduced to $Fe^{3+}$. This would result in a loss of cations due to the shifted state of charge and the precipitation of $Fe_3O_4$. The presence of $O_2$ oxidizes $Fe_3O_4$ to $Fe_2O_3$. [3]

Olivine is already used as bed material in FB reactors due to its natural catalytic activity in desired gasification reactions as an advantage over sand. [46]

Further applications of olivine are the utilization as a raw material within the production of fire-resistant tools and furnaces, abrasives [31], slag formation agent in the steel production industry [31] and as a gemstone. [67]

**Layer formation process:**

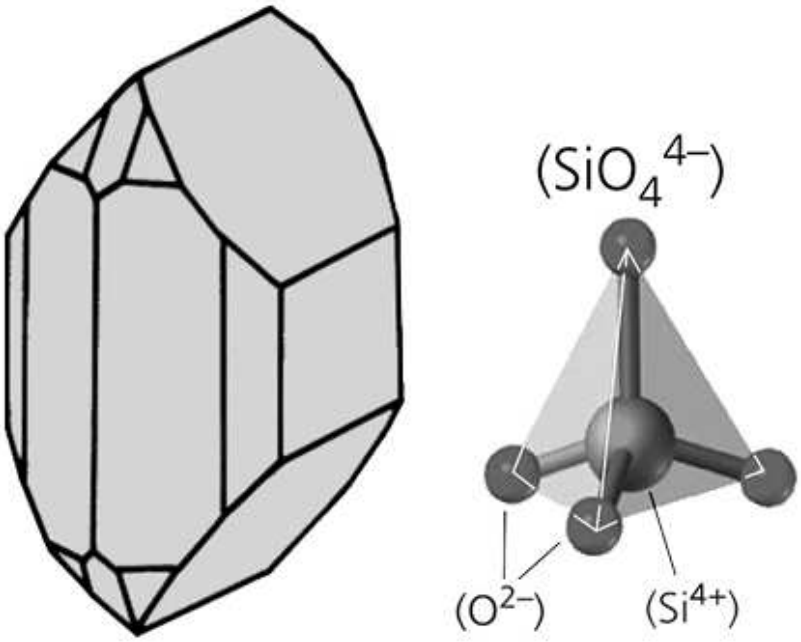


Figure 2.12.: Olivine's crystal structure (left) [67] and the orthosilicate compound (right) [34]

A layer formation process on olivine particles was proposed by Kuba et al. Wood, and woody biomass was processed in a DFB gasifier. The altered bed material was sampled after 4, 8, 16, 24, 32, 48, 72, 180, and 400 hours and investigated. The first modification was already observed after 4 hours, even though it was marginal. A slight ash layer was adhering to some parts of the particle, leaving the rest of it unaffected. This phenomenon was increasingly observed on all samples beginning with an exposure time of 16 h. By the rise of the exposure time in the reactor also the volume of the ash layer increased. The segregation of two major layers was initially observed after an exposure time of 24 h. The outer layer displays a greater relation to the operating time of the process by its growth. Beginning from this point, the inner layer does not grow significantly. An ESEM image of the investigated olivine bed material is portrayed in figure 2.13. The ash layers are clearly visible as bright areas on the image. [53]

The underlying mechanism of the layer formation is initially based on a reaction between CaO and olivine. Both $Mg^{2+}$ and $Fe^{2+}$ get substituted by $Ca^{2+}$. However, $Fe^{2+}$ is more likely to be replaced first by $Ca^{2+}$. The replacement forms some intermediate silicate compounds ($CaMgSi_2O_8$, $Ca_3MgSiO_4$) before $Ca_2SiO_4$ is ultimately formed. A further introduction of $Ca^{2+}$ results in the formation of CaO within the layer. The separation into two layers was affiliated to an enrichment of Ca-compounds in the inner layer while MgO was accumulated in the outer layer. The overall share of $Fe_2O_3$ compounds decreases with an increasing molar Ca/K ratio. A diagram displaying the quantities of crystalline materials is portrayed in dependence of the molar Ca/K ratio in figure 2.14. [53]

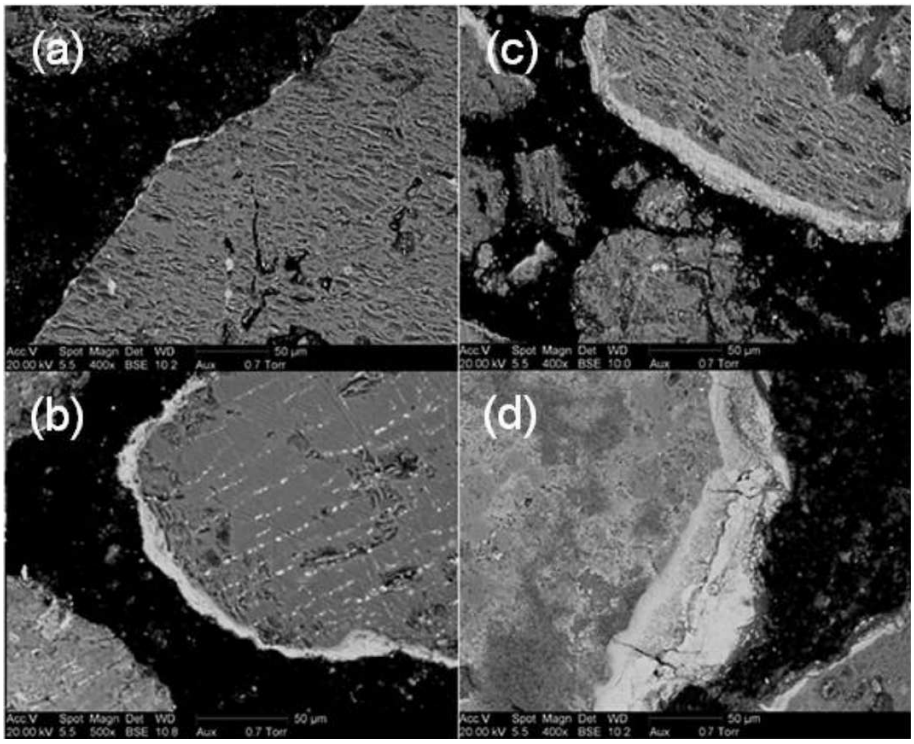


Figure 2.13.: ESEM images of olivine particle cross-sections sampled after 8h (a), 24h (b), 48 (c), and 180h (d) [27]

Further, parallel and vertical cracks towards the border of the particle were also increasingly observed with a rising exposure time of the particles. Especially the vertical cracks show an enrichment of MgO. [53]

### 2.6.2. Potassium-Feldspar (K-feldspar)

According to Okrusch et al. [67] Feldspars are the most abundant mineral in the earth's crust, contributing 51 Vol.-% of the total share. 12 Vol.-% of the total share corresponds to the group of the Alkali Feldspars. However, the earth's mantle does not show any Feldspar content at all. With Orthoclase and Microcline, two low-temperature K-feldspar (K[AlSi3O8]) configurations are available. Orthoclase is a monoclinic metastable intermediate product during the diffusive formation process of the triclinic stable Microcline. Both phases can co-exist alongside each other [67]

K-Feldspar is categorized as a Tectosilicate (also referred to as framework silicate). The tetrahedral $SiO_4$ form a 3-dimenional framework. This framework offers two O-atoms for each Si-atom, which would result in a common chemical formula as Quartz ($SiO_2$), a stable compound. The substitution of a single $Si^{4+}$ ion with $Al^{3+}$ in a tetrahedron results in a shift from $K[Si_4O_8]$ to $[AlSi_3O_8]^{-1}$, giving the framework a negative charge. K compensates the negative charge. [67]

Due to the more voluminous framework, K-feldspar has a density of 2.5 – 2.6 g/cm$^3$, which is comparably low among the minerals. The Mohs-hardness is 6. [67]

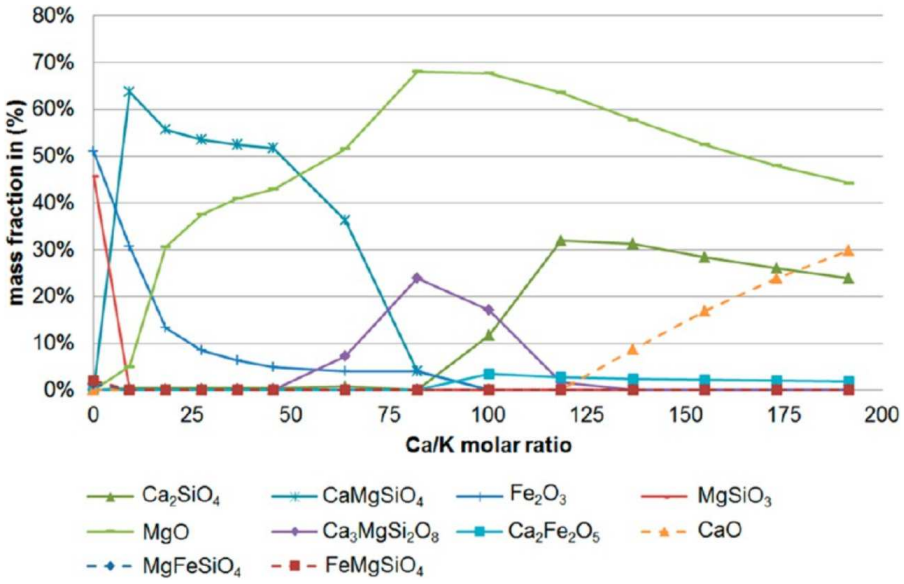


Figure 2.14.: Mass fraction trends of (Ca,Mg,Fe) silicates and oxides in dependence of the molar Ca/K ratio [53]

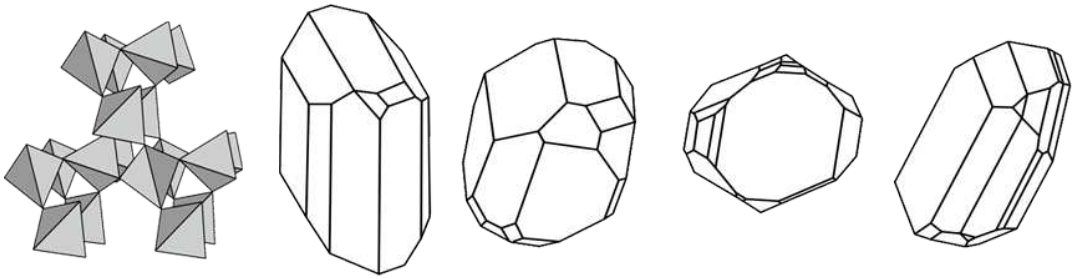

Figure 2.15.: The tectosilicate arrangement (left) and 4 triclinic Feldspar crystal structures(adapted from [62])

K-Feldspar is an important base material within the production of glass, vitreous enamel, ceramics [67] but also in the electro, abrasive, iron, steel, and the chemical industry. [31]

**Layer formation process:**
The layer formation process of K-feldspar was investigated and first proposed by He et al. K-Feldspar was submitted to a BFB, and a CFB combustion reactor fed with wood and woody biomass and sampled after 1, 3, 5, 13 and 23 days. [39]

The application of the BFB combustor already resulted in an initial development of an ash layer surrounding the particle after a day. A strong growth of the layer thickness was observed on the first days. However, it was continuously declining with the bed materials exposure time in the reactor. A separation of the initial layer into an inner homogeneous and an outer particle rich layer was discovered after three days of exposure time. Unlike the layer formation on olivine, both layers were significantly growing in dependence of time. The development of cracks in both layers kicks off with the separation of two layers. [39]

Similar results were obtained during the application of a CFB reactor. The main difference was an overall slower development of ash layers. An initial formation of ash was also observed after a day; however, the segregation into two layers in comparison with the formation of cracks in the outer layer was detected after five days. [39]

A specific layer formation mechanism was proposed arranged in the steps:

- K-melt originating from fuel ash gets attached to the K-feldspar particles. The K-melt enables the diffusion of Ca-compounds into the melt. This is followed by the formation of crystalline Al-Ca-Si compounds, which grow towards the core of the particle. Ash particles which are not exposed to diffusion towards the core of the particle will be incorporated into the outer layer.
- The K-melt disappears as a result of $Ca^{2+}$ diffusion, followed by the appearance of an outer layer after 3-5 days.
- The layer formation drastically slows down after an exposure time of 13 days. The barrier $Ca^{2+}$ must overcome by diffusion was rising proportionally with the time. This results in slow diffusion rates of $Ca^{2+}$.

A schematic illustration of all three phases is portrayed in figure 2.16.

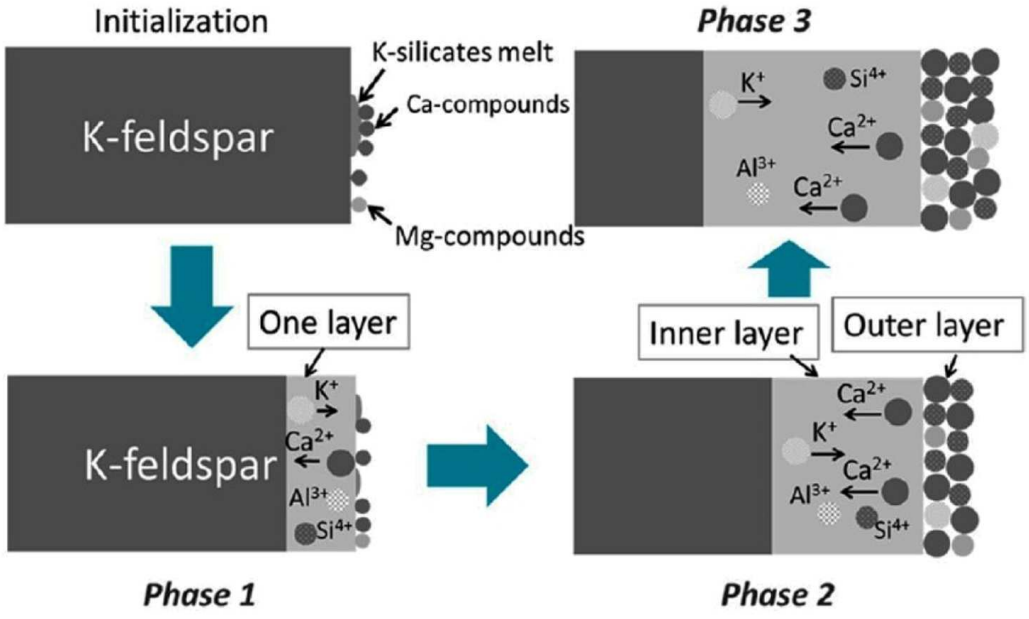


Figure 2.16.: Schematic illustration of the layer formation process on K-feldspar which was processed with wood and woody biomass [39]

A conducted SEM/EDS analysis of the bed material resulted in the discovery of larger crystalline Al-Ca-Si compounds quantities in the inner layer. Cracks in a K-rich area are enriched with Al-Ca-Si compounds. The outer layer, however, shows high Mg-Ca-Si contents. The average molar composition of the ash layers is illustrated in figure 2.17. All samples have a continuous decrease of the K- and Al-quantities in common within every

layer. The Ca-quantities strongly rise simultaneously in dependence of time, especially in the outer layer. Regarding Mg-compounds, no quantities were observed in the inner layer. [39]

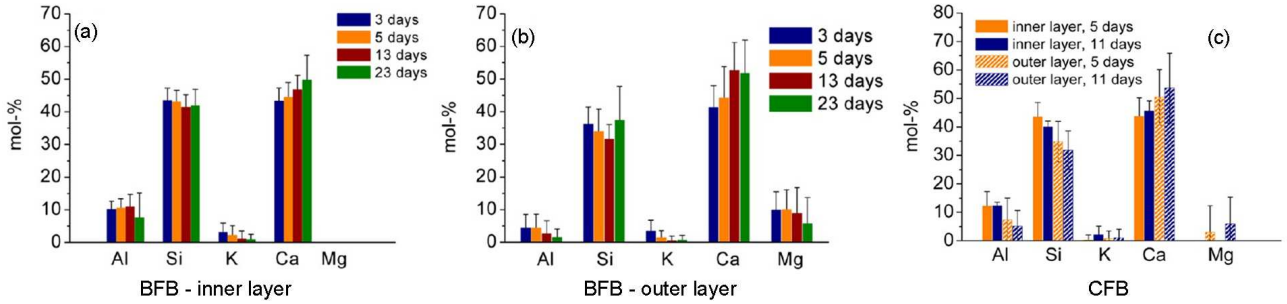


Figure 2.17.: Average molar composition (C- and O-free base) of the inner and outer ash layers on K-feldspar samples of both reactors (adapted from [39])

## 2.7. Vibrational Spectroscopy

For the purpose of the characterization of chemical properties of chemically active bed materials, an appropriate variety of methods is available. Assuming that the working conditions influence the chemical activity, in-situ measurements were the best matching opportunity to characterize the bed materials. As a result, vibrational spectroscopy methods such as Raman and infrared were chosen. Especially the observation of adsorption processes of gaseous phases onto surfaces is on focus. Their theoretical fundamentals will be described in the following. Each spectroscopic method can contribute a share of the demanded information in order to characterize solid particles. Thereby, a combination of the conclusions of various spectroscopic methods can be assembled to an extensive description of a particle's chemical properties, such as chemical structure. [64]

### 2.7.1. Molecular Vibrations

Molecular Vibrations in solid materials are either excited by the absorption of photons or the scattering of photons, neutrons, and electrons. Each molecule possesses characteristic energy levels which are coupled to their way of vibrational and rotational movement. These molecular movements are commonly referred to as modes. The absorption or scattering of photons carries out transitions between quantized energetic states of molecules. The inharmonic potential state of the constituent atoms can be approximated for marginal amplitudes of oscillation with Hooke's law. Equation (2.15) expresses the interatomic potential $V(r)$ as the distance between the moving atoms $r$ in relation with the force constant of the vibrating bond $k$ and the and the equilibrium distance between the atoms $r_{eq}$. [32,64]

$$V(r) = \frac{1}{2}k(r - r_{eq})^2 \tag{2.15}$$

With the condition that each level of molecular vibration is quantized, the interatomic potential can also be expressed in vibrational energy states $V_{iv}$. Equation (2.16) gives a mathematic expression between the vibrational energy states $V_{iv}$, the Planck's constant $h$, the fundamental frequency of the particular mode $\nu_i$ and the vibrational quantum number ($v_i \in \mathbb{N}^*$). [32, 64]

$$V_{iv} = h\nu_i \left(v_i + \frac{1}{2}\right) \tag{2.16}$$

Figure 2.18 portrays the potential energy of diatomic molecules over the displacement of their constituent atoms. Thus, it becomes clear that the quadratic character of the Hooke's law is only comparable to the inharmonic potential as long as the transitions between the modes are small. [32]

In most cases the energetic difference between the ground ($v_i = 0$) and first excited state

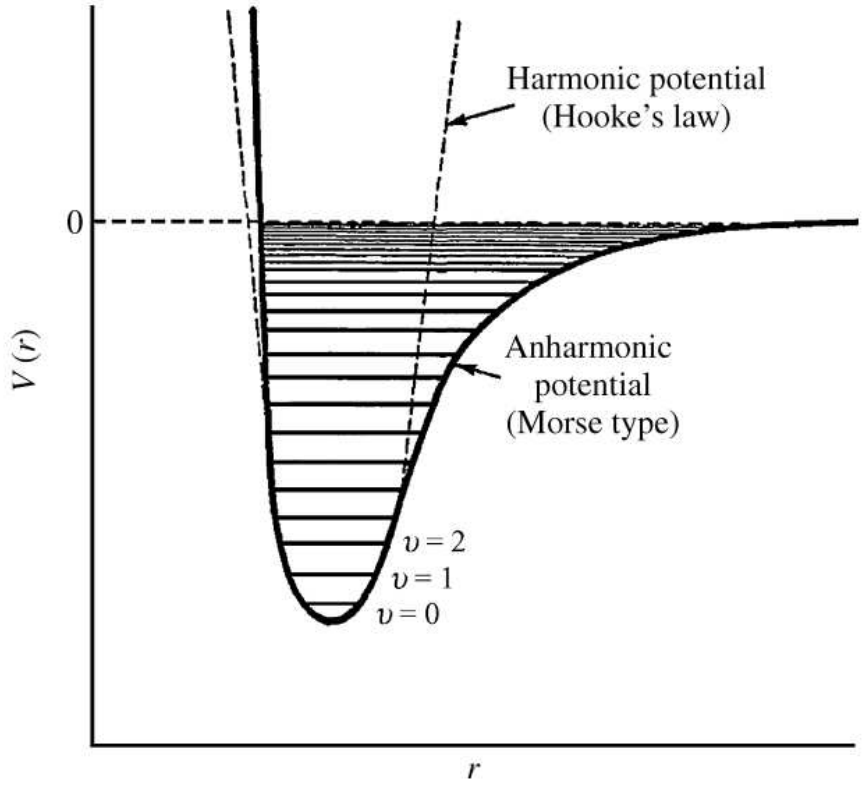


Figure 2.18.: Potential energy of a diatomic molecule during a vibration for a harmonic and inharmonic oscillator [32]

($v_i = 1$) corresponds to the radiation energy of the mid-infrared spectrum (400 $cm^{-1}$-4000 $cm^{-1}$). [32]

A connecting expression between the frequency of a particular mode $\nu_i$ and the masses $m_1$ and $m_2$ of the constituent atoms is given in equation (2.18). The expression is commonly simplified by the introduction of the reduced mass $\mu$, which is described in equation (2.17).

$$\nu_i = \frac{1}{2\pi} k\text{ţ} \tag{2.17}$$

$$\text{ţ} = \frac{m_1 m_2}{m_1 + m_2} \tag{2.18}$$

The number of different molecular vibrations derives from the reflection of each molecule with N atoms having 3N degrees of freedom. These include three translational degrees of freedom and three rotational degrees of freedom along the three principal axes. Linear molecules have only two rotational degrees of freedom, where no change of energy occurs during the rotation along the main axis. As a result, the total number of fundamental vibrations is 3N – 6 for non-linear and 3N – 5 for linear molecules. Overtones and combi-

nations of fundamental vibrations are further known molecular movements. Figure 2.19 gives a suitable overview of common molecular vibrations. [64]

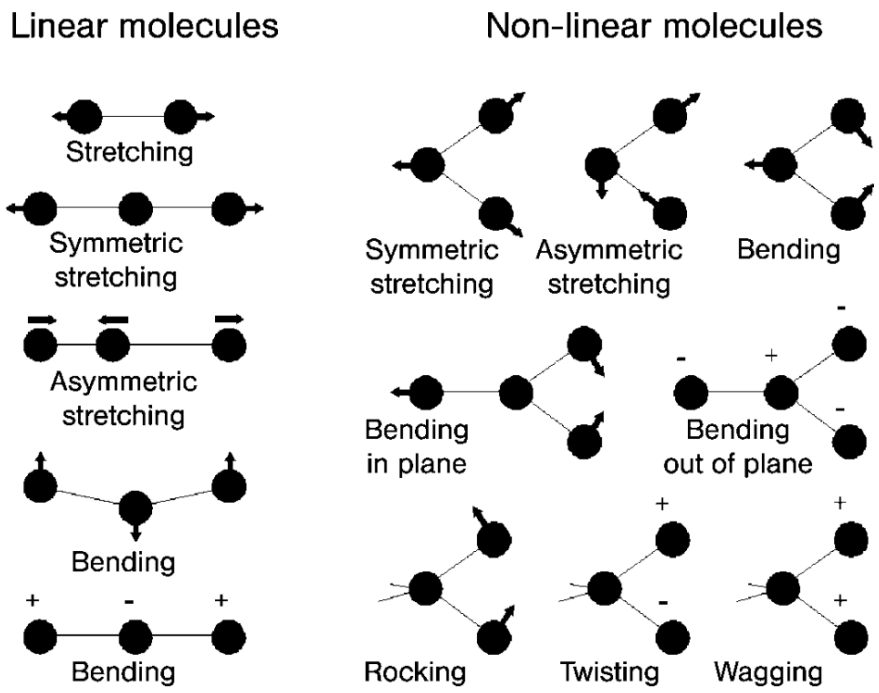


Figure 2.19.: Overview of several molecular vibrations [64]

A diatomic molecule exhibits only a single vibrational mode. Triatomic molecules are already divided into linear and non-linear molecules. Consequently, linear molecules exhibit four vibrational modes in total, which are distributed equally to two stretching and two bending modes. A non-linear molecule shows three vibrational modes, which are equally divided into a symmetric, an asymmetric, and a bending mode. [64]

As already indicated, vibrational modes can occur as a symmetric and an asymmetric form whenever a molecule has more than two constituents. The uniform vibration rhythm of a bond is significant for a symmetric mode. The asymmetric mode can be described by the simultaneous appearance of stretching and contraction of bonds a single vibration. Unfortunately, not every vibrational mode is observable. Especially symmetric and asymmetric modes are excited by different mechanisms. Following this, their visibility depending on the measurement is limited. [64]

### 2.7.2. The Raman Effect

Whenever a photon with the frequency $\nu_p$ approaches a molecule it will either be scattered, absorbed, or intromitted through the substance without any interaction.

$$E_{photon} = h\nu_p \tag{2.19}$$

Equation (2.19) expresses the energetic level of photons. The scattering of a photon only occurs in a ratio of $1 : 10^6$ compared to the transmission through the material. Inelastic scattering was found to occur by far more rarely ($1 : 10^{10} - 1 : 10^{12}$) that elastic scattering. Thus, inelastic scattering was not recognized until it was initially observed by C. V. Raman and K. S. Krishnan in 1928. Elastic scattering (also Rayleigh-scattering) refers to an extremely brief sequence of:

- Moving photons excite electrons around the nuclei onto a virtual (polarized) state with the energy $h\nu_0$. This is connected with a distortion of the cloud of electrons surrounding the nuclei.
- The molecule simultaneously transfers the same amount of excitation to photons again due to its electrons $h\nu_e$.
- The nuclei do not get affected by the change of the cloud of electrons.

In this case, $h\nu_p$ and $h\nu_e$ are equal, and the overall change of the light's energy is zero. However, in the case of an interaction between electrons and nuclei, the vibrational or rotational movement of the molecule will be modified. This results in a detectable difference in the energy electrons finally obtain due to photons. The energy is "lost" to the nuclei. [22, 64]

To be exact, a change of a dipole moment along a vibrational coordinate is triggered as a response to the incident radiation. Therefore, a polarizability of the affected molecule must be given to observe an effect. The electron which was promoted into its virtual state decays back into its default state. However, a small share of the energy obtained from the photon was consumed by the molecule. This is referred to as inelastic (or Raman) scattering. Excited molecules emit energy while (Anti-Stokes scattering, $\nu_e < \nu_p$) molecules in their initial state are excited (Stokes scattering, $\nu_p > \nu_e$). The illustrative variation of the molecular energy level is portrayed in figure 2.20. [22, 75]

A mathematic relation between the, induced dipole moment $\mu_{ind}$, polarizability $\alpha$ and the incident electric $E$ field is described with equation (2.20).

$$\mu_{ind} = \alpha E = \alpha E_0 cos\,(2\pi\nu_p t) \tag{2.20}$$

The polarizability $\alpha$ is dependent on its nuclear coordinates $Q_k$.and the vibrational modes of the molecule. In case of a small vibrational displacement of the nuclear, with the vibration frequency of the nuclear is $\nu_m$, and $\alpha_0$ is a function of $\alpha(Q_k = 0)$ a Taylor expansion can be applied to describe $\alpha$ as conducted in equation (2.21).

$$\alpha = \alpha_0 + \left(\frac{\partial\alpha}{\partial Q_k}\right)_0 Q_k \cos\,(2\pi\nu_m t) + ... \tag{2.21}$$

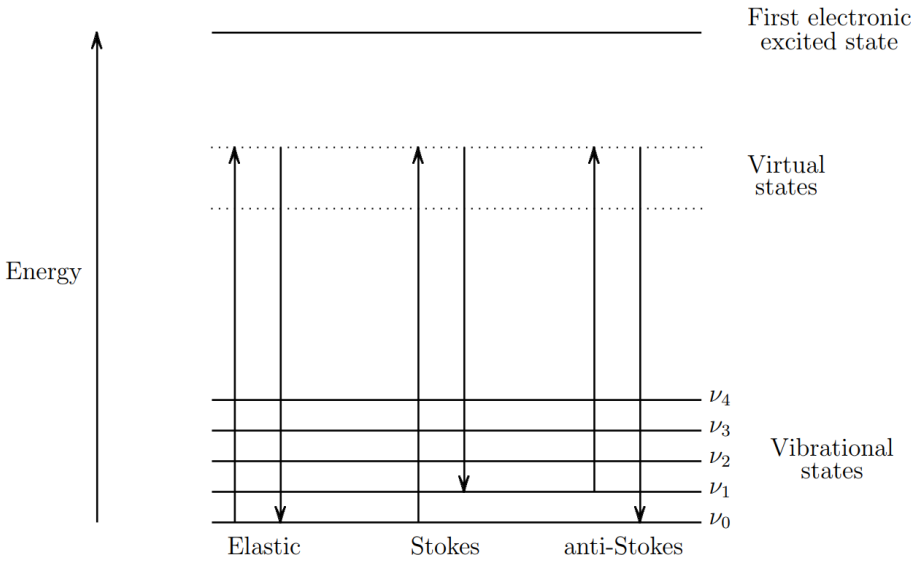


Figure 2.20.: Schematic illustration of energy levels after various scattering scenarios [15]

Introducing the equations (2.21) into (2.20) by considering trigonometric identities gives the mathematic expressions of Raman and Rayleigh-scattering in equation (2.22).

$$\mu_{ind} = \overbrace{\alpha_0 E_0 \cos(2\pi\nu_p t)}^{Rayleigh} + \frac{1}{2}(\frac{\partial\alpha}{\partial Q_k})_0 Q_k E_0 [\overbrace{\cos(2\pi(\nu_p - \nu_m)t)}^{Stokes} + \overbrace{\cos(2\pi(\nu_p + \nu_m)t)}^{anti-Stokes}] \tag{2.22}$$

The necessary condition of Raman scattering can be concluded from equation (2.21). Raman scattering can only occur when $\left(\frac{\partial\alpha}{\partial Q_k}\right)_0 \neq 0$. Therefore, only a change of polarization is observable. Usually, the change of polarization is conducted within a symmetric stretch resulting in its Raman activity which is illustratively portrayed in figure 2.21.

The relation between the scattering intensity $I$, the polarizability $\alpha$, the frequency of the laser light $\nu_p$ and the laser power $l_p$ is given in equation (2.23). [15]

$$I \propto l_p \alpha^2 \nu_p^4 \tag{2.23}$$

Raman-scattered light is favorably collected perpendicularly to the direction of propagation. Nevertheless, a collection is also possible in the positive and opposite direction of propagation. The excitation of strong bonds and light atoms generally rise to high vibrational frequencies. [22]

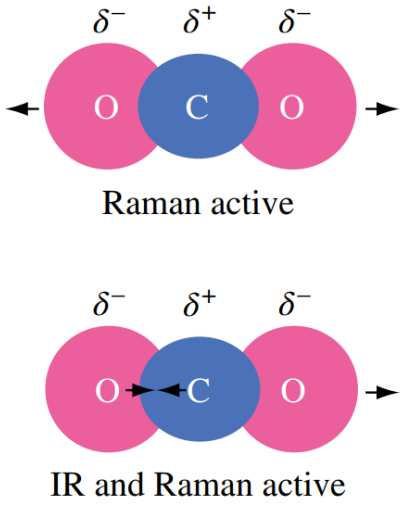


Figure 2.21.: Illustration of the electron cloud during a vibrational mode (symmetric stretch) [75]

Stokes and anti-Stokes spectra exhibit the same information with a single exception. The intensity of the anti-Stokes spectra is usually comparably low. This is contributed to the fact that molecules at room temperature are usually approached by a photon their ground state $E_0$ at room temperature. Following this, anti-Stokes scattering is a simply less common form of Raman-scattering. [15, 64]

As a major advantage Raman spectroscopy is the in-situ characterization of catalysts. Raman is able to detect interactions between the signals of adsorbed compounds and the gas phase. [64] However, fluorescence is a commonly occurring problem also being a reason why IR spectroscopy is commonly chosen over Raman spectroscopy. Fluorescence is a stronger effect than the Raman-effect. The fluorescence of impurities or sample components elevate spectral backgrounds over the original spectrum when it gets detected. [64, 75]

### 2.7.3. Infrared spectroscopy

IR-spectroscopy is also applied by the detection of molecular vibrations. Further, photons commonly in the range of mid-IR wavelength approach a molecule. Similar as in Raman spectroscopy, the wavelength of the photons and plays a central role as expressed in equation (2.19). In contrast to the Raman effect, the observed effect in infrared spectroscopy is the transition of the electric dipole moment. It must change in at least one component due to the exact uptake of the energy difference of the vibrational transition. Consequently, the obtained IR spectra derive from the transition of the quantized vibrational modes, whereas the intensity of the IR band is corresponding with the change of the dipole moment. Heteroatomic molecules such as CO, NO, and OH exhibit strong infrared bands, whereas homoatomic molecules such as $H_2$ and $N_2$ possess no observable infrared activity. The absence of a dipole moment on homoatomic molecules results in an IR-inactivity. Further, this results in an IR inactivity of linear molecules. [19, 64]

The design of the spectrometer itself occupies great importance. Most state-of-the-art spectrometers are based on a two-beam interferometer, which was initially designed by Michelson in 1891. With the improving performance of computers applied in spectroscopy, Fourier transformation (FT-IR) found application in IR spectroscopy. Major advantages of FT-IR spectroscopy are clearly more pronounced spectra. Further, detected signals can be simultaneously processed into interferograms, where they will be Fourier transformed into IR spectra. [19, 22, 64]

The upcoming listing gives an overview of the background of the applied FT-IR measurement techniques in this work.

**Diffuse reflectance infrared Fourier transform spectroscopy (DRIFTS)**
DRIFTS utilizes the effect of incident radiation on a powdered sample. The radiation gets absorbed as it refracts through each particle and is scattered by a combined mechanism consisting of reflection, refraction, and diffraction. A comparably low amount of that incident radiation emerges back from the surface of the sample. The re-emerging part of the incident radiation is defined to be diffusely reflected. [32]

DRIFTS is commonly applied as a technique to simply conduct quick measurements of powdered samples without high necessary efforts in sample preparation. Another field of application is measurements of samples in controlled atmospheres. [32]

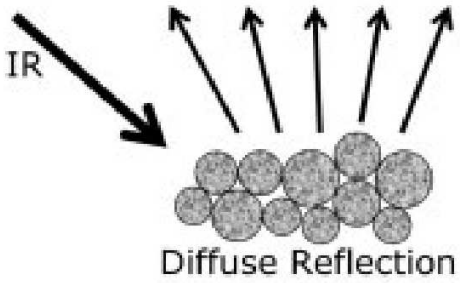


Figure 2.22.: Illustration of the DRIFTS technique (adapted from [64])

**Attenuated Total Reflection (ATR)**
ATR relies on the contact between the sample and a sensing element. The spectrum is recorded as a result of that contact. In opposite to other sampling techniques, ATR does not utilize transmitted radiation through the sample but the internally reflected radiation between the sample and the sensing element. Finally, the so-called evanescent radiation exceeds the surface of the crystal and is collected by the detector. ATR is a frequently applied technique due to its little or none demand for sample preparation. Further, more native results can be obtained as no changes in morphology occur due to sample preparation. Consistent results and a comparably low necessary expertise are further advantages. [32, 64]

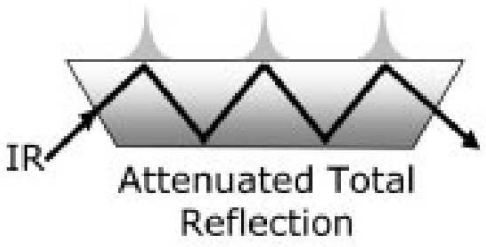


Figure 2.23.: Illustration of the ATR technique (adapted from [64])

## 2.8. Quadrupole Mass Spectrometer (QMS)

Mass spectrometers (MS) are commonly applied as qualitative and quantitative analysis method, which contributes to the general investigation of chemical compounds. Especially, the MS is commonly utilized to obtain knowledge about the mass and structure of chemical compounds including their fragments. The segregation of various occurring isotopes is also possible. [5]

The typical functional design of MS can be divided into three units, which will be elaborated for the QMS and for gaseous substances in the following.

Right after the entrance unit, the **ion source** produces gas-phase ions. There is a choice of ion source techniques where each of them comes with advantages and drawbacks of their own. In general, they are divided into soft and hard ion sources. Hard ion sources apply strong energetic forces such as highly accelerated electrons, which lead to the decay of the analyte. At least, some information can be obtained about the fragments as a result. Soft ion sources rely on electrons on a comparably low energetic state or thermal treatments. As a result, some information about the mass of the whole molecule can be obtained. [5,29]

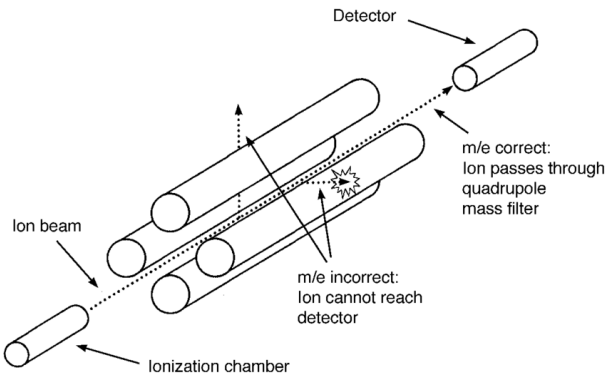


Figure 2.24.: Illustration of the ions trajectory [41]

A very central unit of the QMS is the **mass analyzer**. The mass analyzer classifies and separates the formerly produced gas phase ions according to their mass-to-charge ratio (m/z). The gas-phase ions are accelerated by an oscillating electric field, which is in control. Their path leads them perpendicular through 4 parallel metal rod electrodes where they are selectively stabilized or destabilized. Stabilized ions with chosen m/z ratios pro-

ceed to the detector while destabilized ions get trapped. [5, 29]

The **detector** collects the ions with the demanded m/z ratio by the registration of the intensity of the ion current. The current gets transferred into an electric signal in the following, which can be assigned computer-assisted. [5]

# 3. Materials and Methods

This work targets the investigation as well as the description of compounds that are localized on ash-layered and non-layered olivine and K-feldspar that were used in a gasifier and combustor.

## 3.1. Bed Materials

### 3.1.1. Olivine

Fresh and layered samples were provided by the combined heat and power DFB gasification plant in Senden, Germany (generates 5.1 $MW_{el}$ power and 6.4 $MW_{th}$ district heating). Logging residues and cut-off root ends and branches were used as fuel. Only 70% of the share is contributed by wood chips. Bark (15%) and needles contribute the rest of the fuel. The gasifier was operated at temperatures as high as 850 °C. After 1200h of operation time, samples were taken from the bottom of the combustion reactor. The composition of ash is a major contributor to the layer formation process on bed materials. A determination of the main ash components was deployed and is listed in Table 3.1. The composition of fine ash is similar to feedstock ash and the outer layers of olivine. Therefore, the comparison of the different ash fractions has been expanded in favor of the fine ash composition in table 3.1 [48, 52]
As already indicated in Table 2.1 for forest residues and barks, the investigated feedstock ash shows high contents of CaO, $SiO_2$, $K_2O$, and lower but clearly visible $P_2O_5$ contents.

### 3.1.2. K-Feldspar

The investigated fresh and layered K-feldspar samples were provided by a prior study with a bench-scale (5 kW) bubbling fluidized bed combustor. Bark, chicken manure, and a bark-chicken manure mixture were fed as a fuel. The bark-chicken manure mixture layered K-feldspar sample was obtained with a fuel ratio of 30% chicken manure and 70% bark based on the mass fraction. The operating temperature was kept in a range close to 800 °C. An operating time of 40 hours was not exceeded. Samples were taken after 4, 8, 16, 24 ,32 until the end of operating time if no defluidization took place. However, the share of the sampled bed materials, which are further emphasized in this work are [88]:

- non-layered K-feldspar
- layered K-feldspar
    - as a result of combustion with bark and sampled after 8 and 32 hours (B8 & B32)

Table 3.1.: Elemental composition (expressed as oxides) determined with XRF analysis [52]

| | Feedstock ash [wt.%] | Layered olivine [wt.%] | Fine ash [wt.%] |
|---|---|---|---|
| $Fe_2O_3$ | 0.7 % | 6.8 % | 2.0 % |
| CaO | 55.6 % | 13.8 % | 54.6 % |
| $K_2O$ | 12.6 % | 0.7 % | 2.9 % |
| $SO_3$ | 2.9 % | 0.1 % | 0.4 % |
| $P_2O_5$ | 4.8 % | 0.3 % | 1.5 % |
| $SiO_2$ | 13.4 % | 34.3 % | 22.8 % |
| $Al_2O_3$ | 3.3 % | 0.9 % | 3.1 % |
| MgO | 5.0 % | 39.5 % | 10.3 % |
| Others | 1.7 % | 3.6 % | 2.4 % |
| | 100.0 % | 100.0 % | 100.0 % |

Table 3.2.: Fuel ash composition given in mol/kg fuel on a dry base [88]

| | Bark [wt.% d.b.] | Chicken Manure [wt.% d.b.] | Bark-Chicken Manure mixture [wt.% d.b.] |
|---|---|---|---|
| Fe | 0.07 % | 0.03 % | 0.06 % |
| Ca | 0.15 % | 1.18 % | 0.65 % |
| K | 0.04 % | 0.36 % | 0.14 % |
| S | 0.03 % | 0.24 % | 0.07 % |
| P | 0.03 % | 1.14 % | 0.35 % |
| Si | 0.53 % | 0.24 % | 0.47 % |
| Al | 0.26 % | 0.08 % | 0.17 % |
| Mg | 0.07 % | 0.65 % | 0.26 % |
| Na | 0.06 % | 0.36 % | 0.13 % |
| Cl | 0.01 % | 0.29 % | 0.07 % |

- as a result of combustion with chicken manure and sampled after 8 hours (CM8)
- as a result of combustion with a bark-chicken manure mixture and sampled after 8 and 40 hours (M8 & M40)

The elemental composition of the obtained fuel ash is given in table 3.2 The composition of non-layered K-feldspar is listed in table 3.3.

Table 3.3.: Elemental composition of non-layered K-feldspar (expressed as oxides) determined with [88]

| | Non-layered K-feldspar [wt % on dry base] |
|---|---|
| $Fe_2O_3$ | 0.04 % |
| CaO | 0.03 % |
| $K_2O$ | 14.74 % |
| $P_2O_5$ | 0.09 % |
| $SiO_2$ | 65.70 % |
| $Al_2O_3$ | 17.90 % |
| MgO | 0.01 % |
| $TiO_2$ | 0.03 % |
| BaO | 0.33 % |
| L.O.I. | 0.25 % |

L.O.I. = loss on ignition

## 3.2. Analytical Equipment

**Temperature-programmed reduction (TPR)**

The purpose of a TPR was an evaluation of the bed materials activity in the presence of CO and steam in dependence of an elevated temperature. TPR experiments were performed with the Water-gas-shift reaction on a Hidden Analytical CATLAB-PCS microreactor. 25mg were submitted to the microreactor as the fixed bed material. All gases were analyzed with an attached Hiden QIC20 quadrupole mass spectrometer. The TPR operated at atmospheric pressure. 0.2 mol% CO (supplied by Air Products, ± 0.5% rel.) and 0.2mol% $H_2O$ (partial balanced in helium were fed to the microreactor. The flow velocity was set to 50 ml/min. The temperature-ramp was initially started from 50 °C to 800 °C with a heating rate of 10 °C/min. For each step (every 50 °C), the temperature was maintained in stationary conditions for 20 minutes. The mass spectrometer was prepared to record the mass to charge ratios of: CO (m/z = 28), $CO_2$ (m/z = 44), $CH_4$ (m/z = 15) and $H_2O$ (m/z = 18).

**Diffuse Reflectance Infrared Fourier Transform Spectroscopy**

All DRIFTS spectra were obtained with a THERMO/Nicolet 8700 spectrometer. Each sample was submitted, sieved to a particle class of 200 - 250 µm, into a Praying Mantis high-temperature reaction chamber (Harrick Scientific Co., Ossining, NY) equipped with ZnSe windows. The design of the high-temperature reaction is portrayed in figure 3.1

The spectrometer was equipped with a nitrogen-cooled mercury cadmium telluride (MCT) detector. The experiments were realized under the atmosphere of He or an adsorptive probe molecule (MeOH, acetic acid, CO, $NH_3$). Each probe molecule was applied at 40 °C for a period of 20 minutes followed by He with a flow speed of 30 mL/min. Imitated reaction temperatures were set in a range of 40 °C up to a maximum of 500 °C. The gas velocity was set to 30 mL/min for each applied experiment. The equipment was operated

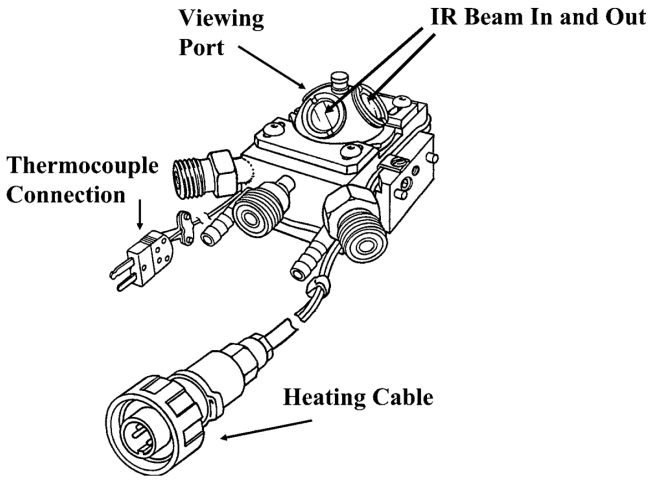


Figure 3.1.: High temperature reaction chamber accessory for DRIFTS (Harrick Scientific's Praying Mantis) [32]

via OPUS v 8.0 software. The ambient temperature reactor was designed according to figure 3.2

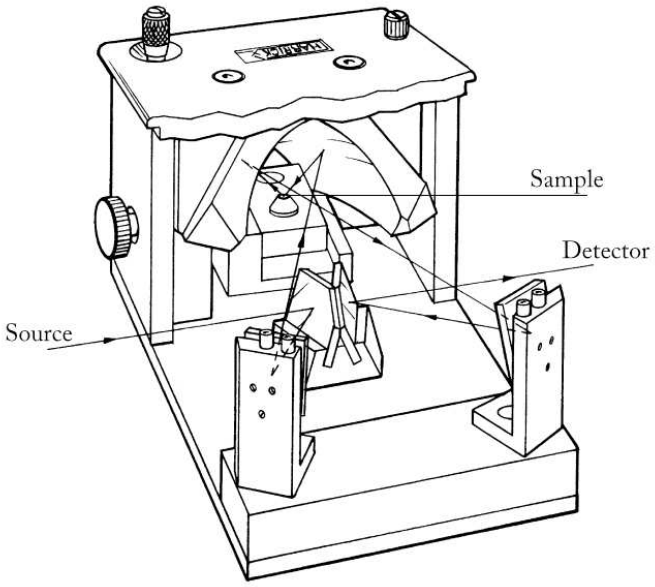


Figure 3.2.: Off-axis optical geometry designed accessory for ambient temperature DRIFTS (Harrick Scientific's Praying Mantis, adapted from [32])

**Attenuated Total Reflectance** ATR was carried out on the same equipment as DRIFTS with Golden Gate ATR accessory (Specac Ltd., Orpington, UK)

**Raman**
All Raman measurements were realized by utilization of a LabRAM HR800 confocal Raman microscope (Horiba Jobin Yvon, France, x50 lenses) equipped with a Synapse CCD detector. The detected laser signal was calibrated to a Raman shift of 520,7 cm-1 with

a pure silicon plate sample. The initial laser power was set to 50 mW, but yet also laser filters (x2, x4, x8) were applied, giving further deployed laser powers (12,9 mW, 5,9 mW, 3,21 mW, 1,27 mW). The penetrating laser power was measured with a LaserCheck (Coherent) equipment. Each sample was ultimately penetrated with a laser power of 3.21 mW, with layered olivine and the bark-chicken manure mix as exceptions (5.9 mW). At least 2 accumulations were performed. The presented results in chapter 4 are obtained by the application of the diode green laser (532 nm). All samples were submitted with equal preparation as the FTIR spectrometer to a Praying Mantis High-Temperature reaction chamber (Harrick Scientific Co., Ossining, NY) equipped with $SiO_2$ windows. Argon was introduced as the atmosphere with a flow speed of 30 mL/min. Each sample was dried at a temperature of 110 °C for 20 minutes. In-situ measurements were conducted in a temperature range between 25 °C and 500°C. Ambient temperature measurements were carried out in a Linkam-CCR1000 (Scientific Instruments Ltd, Waterfield, Surrey, England) equipped with quarts windows. Each sample was measured at least 3 times by the variation to different grains. The processed signal was recorded, smoothed, and baseline corrected by Labspec 5. Smoothing was applied with the Labspec5 internal median smoothing function. An average error of 1.3% was empirically observed.

**Preliminary aggregation of spectra**

The preliminary aggregation of the Raman spectra was carried out in two steps. Initially, a software aided fitting of bands was applied with Labspec5 by using the Gauss-Lorentz function. Bands exceeding an error 1.3% or a variation in intensity (>50%) were considered as a principal component and aggregated accordingly. All other spectra were processed due to averaging calculation by the software OriginPro 2019 (OriginLab).

# 4. Results

## 4.1. Active components on the surface

### 4.1.1. Active components on Layered Olivine (OU)

**Raman**

Due to the particularly high heterogeneity of the olivine samples, one set of measurements covered at least three measurements. Each measurement was carried out on a different grain. In addition, the effect of fluorescence was influencing the obtained results by adding visible noise and variable baseline within a single spectrum. The environment of the apparatus was screened against external influences by locking out the sun and ambient light. However, the monitor of the recording software might have had an influence on single measurements. Nevertheless, these were considered to be insignificant. As a result of this flat shoulders will not be considered as a substance-specific output if they occur only once and will be neglected.

Figure 4.1 shows two ambient Raman spectra of the measured OF sample and consists of six measurements. The most matching results were merged in order to provide two representative graphs as mean values. The displayed spectra include all bands that were detected in the six measurements. The only further manipulation of the curves was additional smoothing in OriginPro (Savitzky-Golay-function) in order to reduce the noise of the signal.

On "OF – 1,3,4,6" four doublets at a Raman shift of 225 $cm^{-1}$ and 244 $cm^{-1}$, 291 $cm^{-1}$ and 299 $cm^{-1}$, 408 $cm^{-1}$ and 432 $cm^{-1}$ with the last one at 584 $cm^{-1}$ and 608 $cm^{-1}$ can be observed. However, the most protruding signal occurs with the triplet consisting of the major bands at 822 $cm^{-1}$, 857 $cm^{-1}$, and a comparably tiny one at 881 $cm^{-1}$. Almost all bands, especially the strong ones, were matched to $SiO_4$ modes in assistance of literature. Chopelas et al. [16] report bands fitting to 302 $cm^{-1}$ and 329 $cm^{-1}$ as a phenomenon due to the translation of $Mg^{+}$-ions. $Fe_2O_3$ was found to cover the residual modes. "OF – 2,5" presents the same major bands but varies in the 200 $cm^{-1}$ to 700 $cm^{-1}$ range. A broad band at 678 $cm^{-1}$ is visible, but especially the formerly mentioned doublets are not clearly visible anymore. Both patterns were confirmed to be olivine with a research on literature. [49, 55]

Figure 4.2 shows the different Raman spectra of the measured OU sample. Due to the heterogeneity and the massive fluorescence 13 measurements have been made, which were divided into three different patterns. The "OU – 3,5" spectrum does not have any common bands with the fresh sample. A comparably less pronounced band at a Raman shift of 355 $cm^{-1}$ was found to be in common with the "OU – F1,F2,F4,6" spectrum. It occurred twice out of the 13 measurements. The "OU – F3,1,2,4,7,8,9" is comparable to the OF

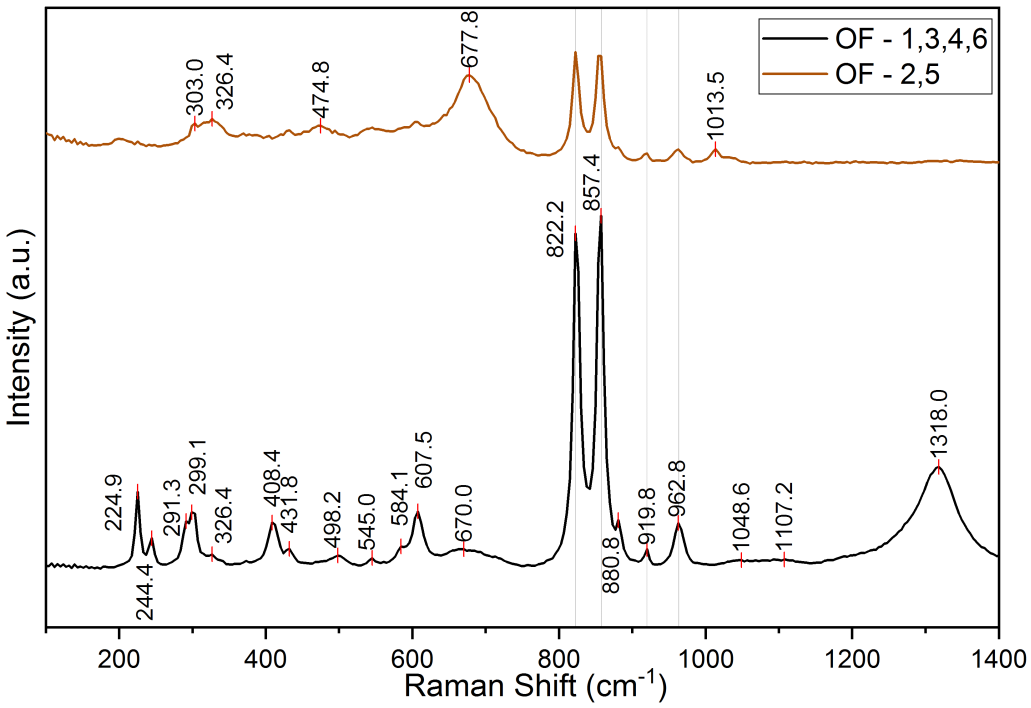


Figure 4.1.: Ambient Raman spectra of OF

sample. 7 of 13 measurements were assigned to this pattern. The characteristic triplet that has also been discovered on the OF sample reoccurs with a shift of $\Delta\omega = 1.3$ in average on all three bands.

However, two of three doublets discovered in OF are diminished drastically or even disappeared while the last one left was also lowered in its intensity. A new stretching beginning at a Raman Shift from 550 $cm^{-1}$ to 800 $cm^{-1}$ with the center at 705 $cm^{-1}$ and a comparably insignificant band at 1085 $cm^{-1}$ occurred. The remaining bands were also associated with the ones of the OF sample within a shift of $\Delta\omega = \pm 2.6$. The "OU – F1,F2,F4,6" spectrum has similarities to "OU – F3,1,2,4,7,8,9". It displays a doublet at the characteristic triplet position leaving the band around 882 $cm^{-1}$ out. A new stretching at 712 $cm^{-1}$ incorporates almost everything in the range between 500 $cm^{-1}$ and 900 $cm^{-1}$. By regarding single measurements additional information about the eventual structure of the curve below the stretching is provided. The range between 200 $cm^{-1}$ and 350 $cm^{-1}$ also differs from the OF sample. A stretching with two comparably small bands occurs at 247 $cm^{-1}$ and 276 $cm^{-1}$. The additional cropped range spectra in the background vary significantly from the average and contribute further information of discovered bands. Further new bands are 1086 $cm^{-1}$, 3619 $cm^{-1}$, and a comparably lower stretching around 1200 $cm^{-1}$. After a comparison of all three patterns with several measured metal oxides many common bands were observed. A combination of $CaCO_3$ and CaO matches six bands, including the wide stretching at a Raman shift of 712 $cm^{-1}$. Also, hematite, MgO, and MnO were showing similarities.

Alongside the ambient measurements, the samples were also investigated during a temperature treatment. Figure 4.3 displays the results of the temperature treatment. Both

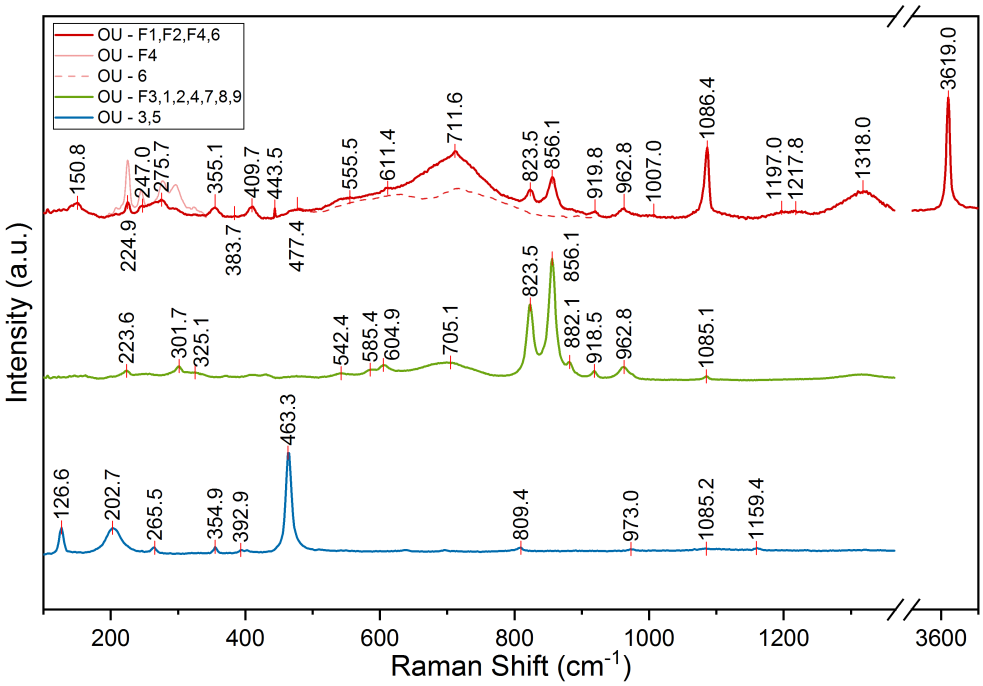


Figure 4.2.: Ambient Raman spectra of OU

patterns have in common that a wide stretching in the range of 1100 $cm^{-1}$ and 1700 $cm^{-1}$ occurs with an elevated temperature. The OF sample shows the mentioned stretching at a temperature around 500°C. An additional sample that was treated with 20 vol% O2 and Argon at 500°C does not show any bands or stretchings in the mentioned range at all. The OU sample gives another phenomenon about the intensities of the stretchings. While the base spectra at 25°C gives a strong band around a Raman shift of 1320 $cm^{-1}$ the intensity of it is slightly diminished at 100°C. However, a wide stretching in the range of 1100 $cm^{-1}$ and 1700 $cm^{-1}$ occurs. Even though 300°C is not the highest temperature, it induces the largest stretching in the mentioned range. However, the stretching is still present at a temperature of 500°C.

**ATR**

In figure 4.4 ATR spectra of the OF and OU samples are shown. While the intensities of the curves differ, common bands can be found in the wavenumber range of 600 $cm^{-1}$ to 1000 $cm^{-1}$. A strong negative band at around 630 $cm^{-1}$ and a band at around 3650 $cm^{-1}$ serve as the major differences between the OF and the OU spectra. OF was confirmed to be olivine with a research on literature. In regions between 800 and 1000 $cm^{-1}$, all bands are in correlation to $SiO_4$ modes. [23, 81]

### 4.1.2. K-Feldspar

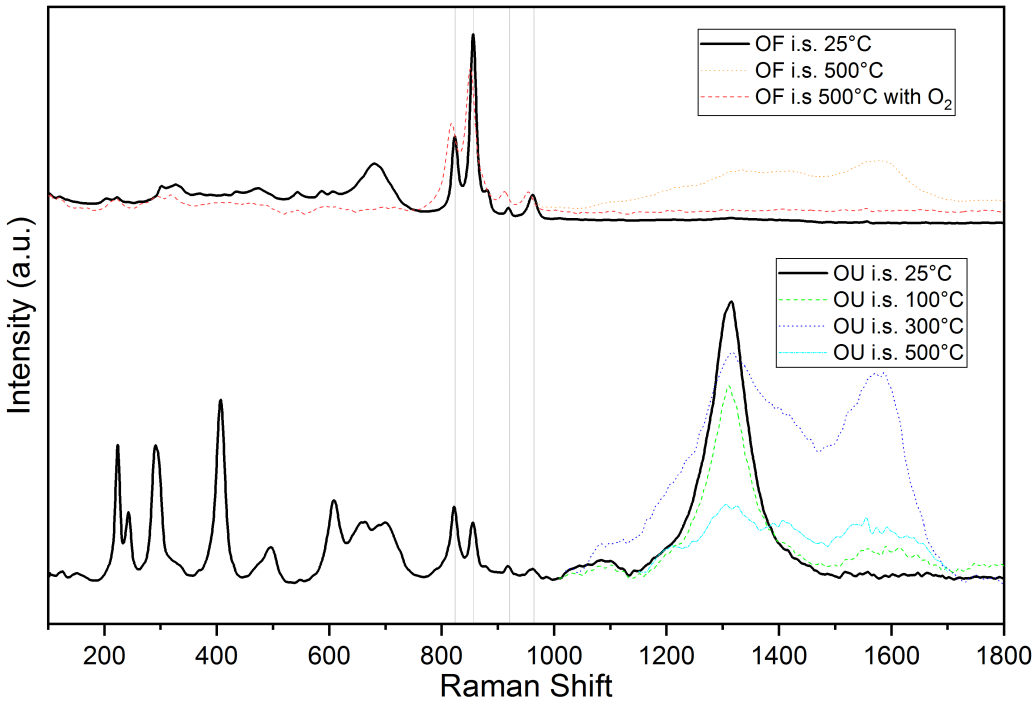


Figure 4.3.: Temperature Treatment Raman spectra of the OF and OU samples

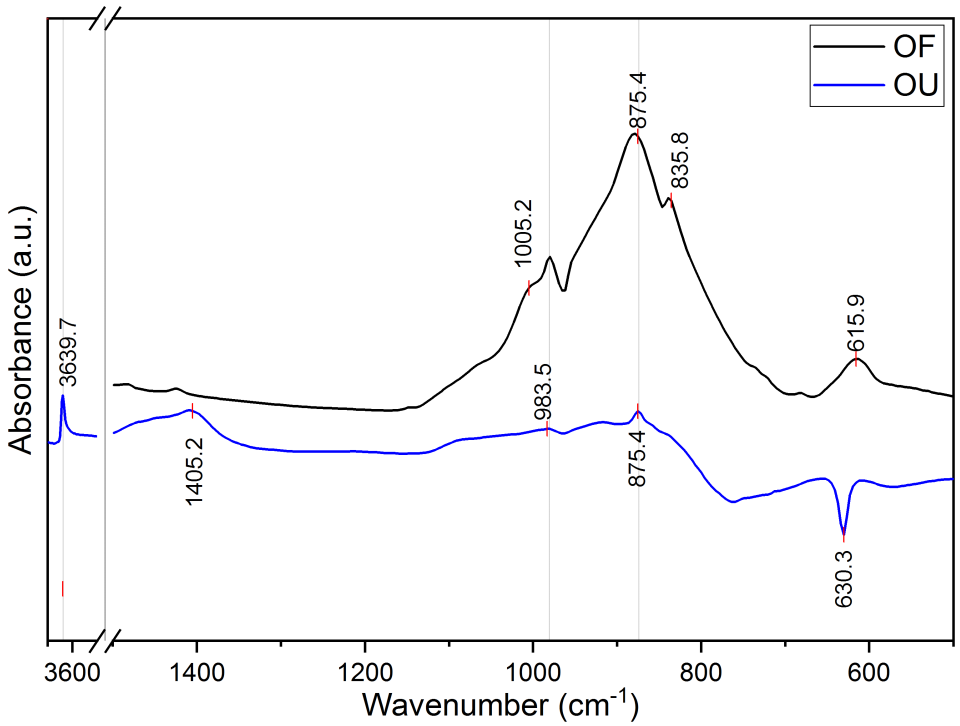


Figure 4.4.: Ambient ATR spectra of OF and OU

### 4.1.2.1. Active components on non-layered K-feldspar

**Raman**

K-Feldspar serves as a base for 5 different other samples, which will be described afterwards. Figure 4.5 shows two ambient Raman spectra of the measured FF sample and consists of six measurements.

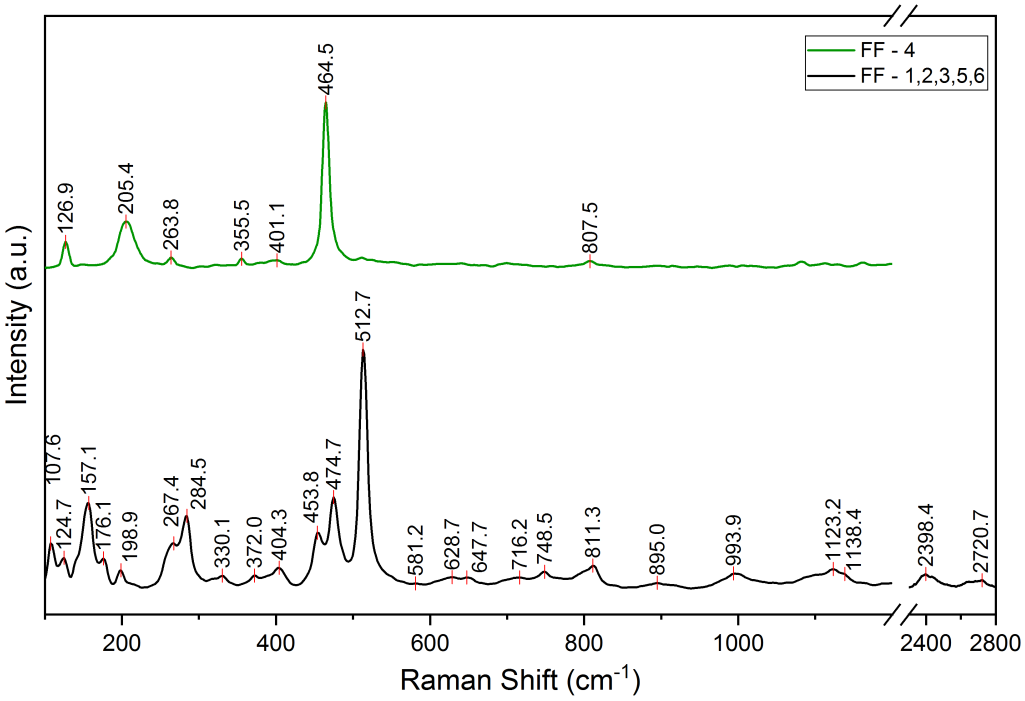


Figure 4.5.: Ambient Raman spectra of FF

The "FF – 1,2,3,5,6" spectrum can be characterized by two doublets and a triplet. Those are located at 157 $cm^{-1}$ and 176 $cm^{-1}$, 267 $cm^{-1}$ and 285 $cm^{-1}$ and the triplet's bands are located at 454 $cm^{-1}$, 474 $cm^{-1}$ and 513 $cm^{-1}$. Further comparably smaller bands have been observed in figure 4.5. The spectrum has also been identified as K-feldspar in literature. [28]

The "FF – 4" spectrum is fairly comparable to the "OU – 3,5" spectrum in figure **??**. Consequently, it can be assumed that the compound which is responsible for all three spectra is identical. Further, it gives the recognition that some grains of FF and OU have overlappings, even if on a comparably low level.

The measurement of the FF sample with the high-temperature reaction chamber range results in the same signals for 25 °C and 110°C. Increasing the temperature causes a very noisy signal that keeps rising until it got cut off from the recording software "Labspec5". The spectra are provided in the appendix and portrayed in figure A.4.

**ATR**

In figure 4.6 the ATR spectrum of the FF sample is displayed. The bands are distributed in

three ranges. The fingerprint range between 600 $cm^{-1}$ and 1250 $cm^{-1}$, the range between 1950 $cm^{-1}$ and 2700 $cm^{-1}$, and the range within 3600 $cm^{-1}$ and 3750 $cm^{-1}$. Also, the FT-IR ATR spectrum was identified to be K-feldspar with corresponding literature. [45]

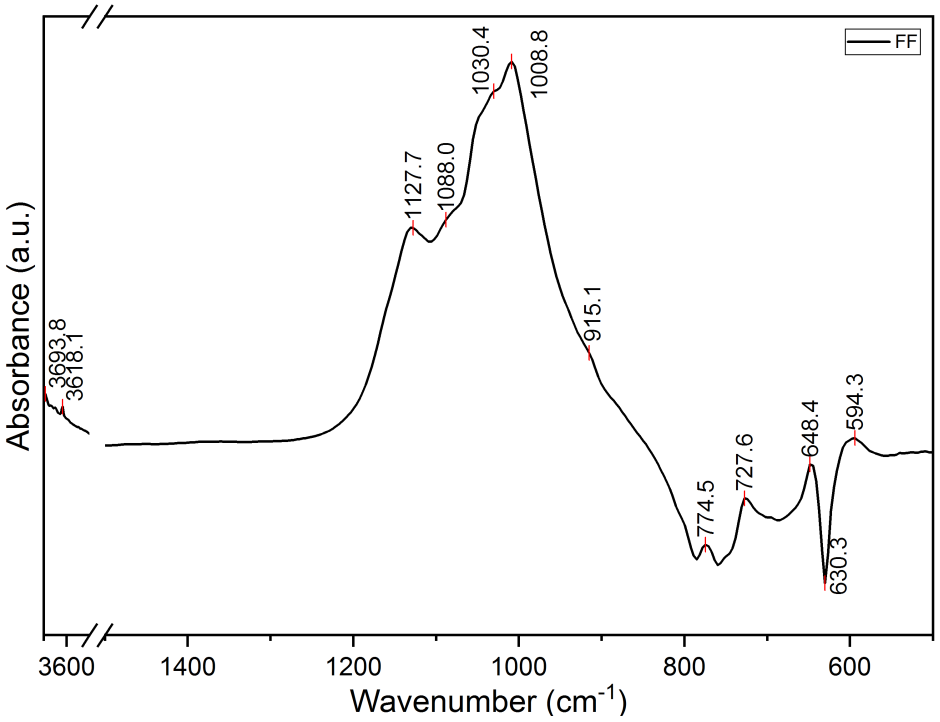


Figure 4.6.: Ambient ATR spectrum of FF

#### 4.1.2.2. Active components on layered K-feldspar with bark as fuel

K-Feldspar served as the bed material with bark as a fuel in a BFB combustion process. The altered K-feldspar bed material got sampled after 8 (B8) and 32 hours (B32) of operating time.

**Raman**

Bark was one of the feedstocks used in the FB combustion processes. The resulting measurements of the samples B8 and B32 are shown in figure 4.7. The B8 sample shows two different patterns, while the B32 sample can form just a single distinct pattern. The major difference of the B8 sample to the FF sample is a wide stretching that masks the Raman shift range between 550 $cm^{-1}$ and 750 $cm^{-1}$ in both patterns. The intensities on the "B8 - 1,3" spectrum is strongly diminished while three comparably small bands occur at 908 $cm^{-1}$, 960 $cm^{-1}$, and 1086 $cm^{-1}$. The discovered phenomena are also found in the B32 measurements with a stronger intensity. Especially the stretching in the range of 550 $cm^{-1}$ and 750 $cm^{-1}$ is clearly increased while the bands that recently occurred are just twice as intense. An additional flat stretching between 1150 $cm^{-1}$ and 1800 $cm^{-1}$ and a band occurred around 3616 $cm^{-1}$. Similarities with the CaO and $CaCO_3$ samples have

been found. The wide stretching between 550 $cm^{-1}$ and 750 $cm^{-1}$ on CaO and the strong band at around 1086 and 3616 $cm^{-1}$ on $CaCO_3$.

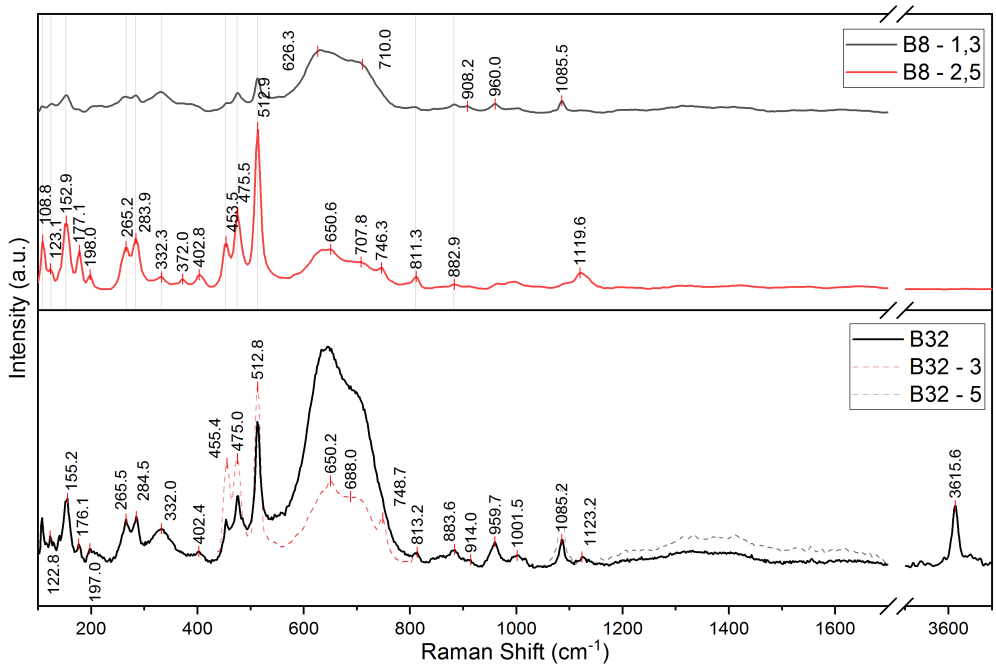


Figure 4.7.: Ambient Raman spectra of B8 and B32

The effects of a temperature treatment are shown in the figure 4.8. Again, a rise of the signal in the range of 800 $cm^{-1}$ and 1800 $cm^{-1}$ can be seen on both samples starting at 300°C for the B8 sample and at 500°C for the B32 sample. The residual sample B8 of the microreactor that was exposed to a temperature ramp that was rising up to 800°C was also measured under ambient conditions. It results in a sample that can be matched to the B32 spectrum.

**ATR**

In figure 4.9, the ATR spectra of the B8 and B32 samples are displayed. The most bands are distributed in the fingerprint range, beginning at around 500 $cm^{-1}$ and ending at 1500 $cm^{-1}$. The further common bands are located in the 1900 $cm^{-1}$ to 2200 $cm^{-1}$ range. The B8 sample shows an additional band at around 730 $cm^{-1}$, while the B32 sample releases a band at around 3650 $cm^{-1}$. In comparison to the FF sample also a comparably small stretching in the range from 1400 to 1500 $cm^{-1}$ is new. They have approx. the same size on both samples. A comparison with the measured CaO sample on FT-IR DRIFTS reveals that both samples have their new bands in common with CaO.

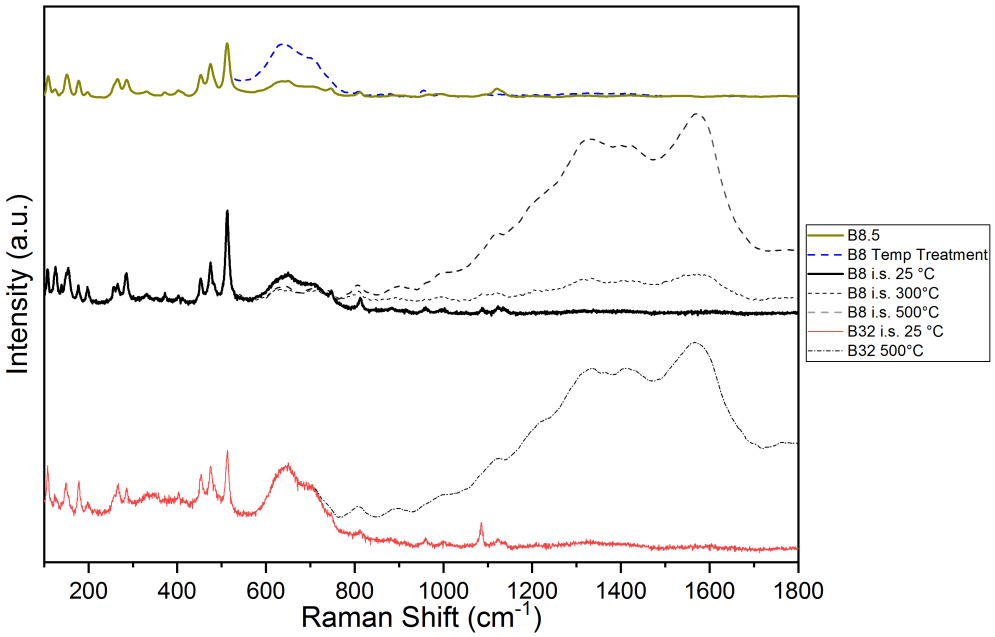


Figure 4.8.: Temperature Treatment of the B8 and B32 samples

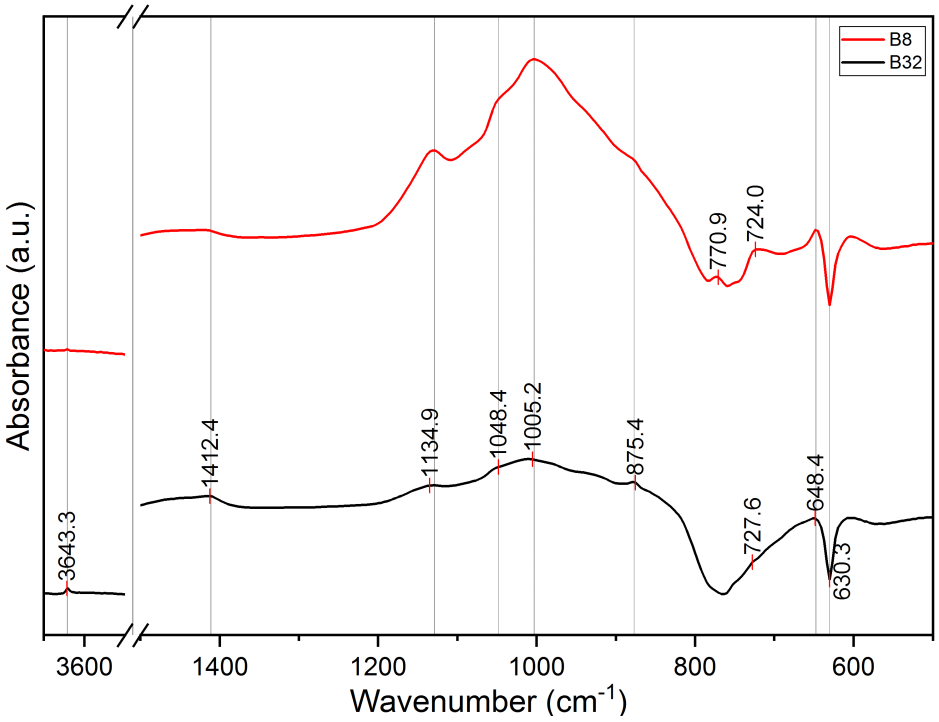


Figure 4.9.: Ambient ATR spectra of B8 and B32

#### 4.1.2.3. Active components on layered K-feldspar with chicken manure as fuel

K-Feldspar served as the bed material with chicken manure as a fuel in a BFB combustion process. The altered K-feldspar bed material got sampled after 8 (CM8) hours of operating time.

**Raman**

The second used feedstock was CM8. Figure 4.10 contains the results of the CM8 and also the M8 and M40 measurements. The Raman spectra show substantial overlaps and were therefore displayed commonly. The CM8 sample can also be divided into two patterns. The "CM8 – 1,3,4,6,7,8" spectrum occurred six times out of eight measurements and shows three major bands at a Raman shift of 962 $cm^{-1}$, 984 $cm^{-1}$, and 3620 $cm^{-1}$. Two additional bands occurred at 357 $cm^{-1}$ and 1085 $cm^{-1}$ for single measurements. Furthermore, a low stretching in the same range of 550 $cm^{-1}$ to 750 $cm^{-1}$ can be seen. The remaining bands between 153 $cm^{-1}$ and 454 $cm^{-1}$ show very small intensities compared to the main bands. The "CM8 – 2,5" spectrum looks more like the basic FF spectrum with the characteristic triplet in between of 454 $cm^{-1}$ and 513 $cm^{-1}$.

**4.1.2.3.1. Bark-chicken manure mix induced ash layer** K-Feldspar served as the bed material with a bark-chicken manure mix as a fuel in a DFB gasification process. The altered K-feldspar bed material got sampled after eight (M8) and 40 hours (M40) of operating time.

The M8 and M40 samples look very similar to the "CM8 – 1,3,4,6,7,8" spectrum with little differences. The stretching between 550 $cm^{-1}$ to 750 $cm^{-1}$ has much higher intensities, and another stretching between 1250 $cm^{-1}$ to 1700 $cm^{-1}$ occurred. The M40 sample misses the band around 3620 $cm^{-1}$, while the stretching around 550 $cm^{-1}$ to 750 $cm^{-1}$ gained more intensity compared to M8. Another comparison with the measured metal oxides results in some common bands with CaO and $CaCO_3$. Again, the stretching around 550 $cm^{-1}$ and 750 $cm^{-1}$ and the stronger bands at 1086 and 3616 $cm^{-1}$. It has to be mentioned that the M40 sample has decreased intensities of the 1086 band and does not show the last band at 3616 $cm^{-1}$. According to literature, $PO_4^{3-}$ modes are responsible for the bands at a Raman shift of 962 $cm^{-1}$ and 984 $cm^{-1}$. The M40 sample lacks the band at 3615 $cm^{-1}$ ($OH^-$ - mode) and has a weaker one at 1086 $cm^{-1}$ ($CO_3^{2-}$ - mode).

A temperature treatment of the CM8 sample did not result in any variations of the ambient Raman spectra. In figure **??**, the temperature dependency of the M8 and M40 Raman spectra are displayed. A large stretching can be observed in the range of 1000 $cm^{-1}$ and 1700 $cm^{-1}$, starting from 300°C on the M40 sample.

**ATR**

In figure **??**, the ATR spectra of the CM8, M8, and M40 samples are displayed. The most bands are distributed in the fingerprint range again, beginning at around 500 $cm^{-1}$ and ending at 1500 $cm^{-1}$. A further common band is located in the range around 2200 $cm^{-1}$ on the CM8 and the M40 sample. All samples show an additional band at around 3640

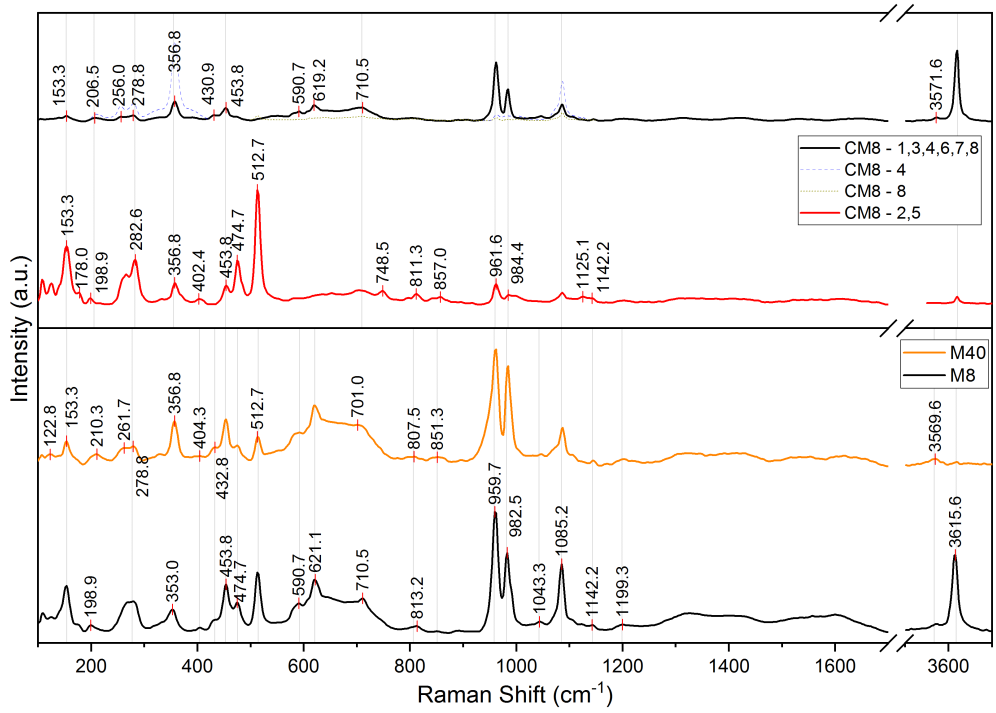


Figure 4.10.: Ambient Raman spectra of CM8, M8 and M40

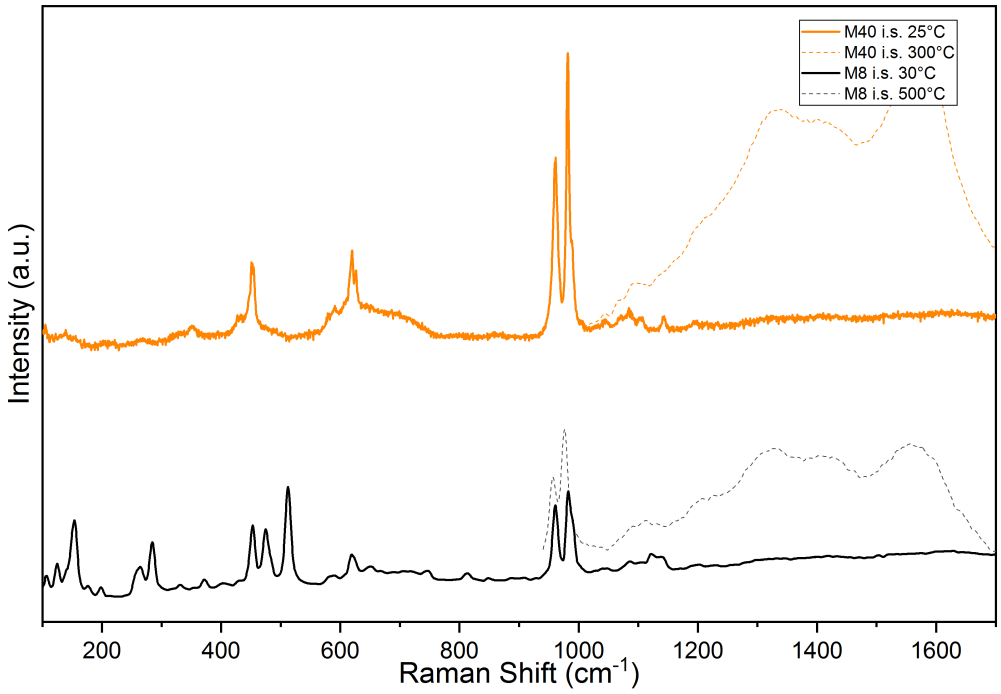


Figure 4.11.: Temperature Treatment of the M8 and M40 samples

$cm^{-1}$ and a stretching between 1400 and 1500 $cm^{-1}$ that was linked to CaO on the other samples earlier. A new stretching in the range of 900 – 1100 $cm^{-1}$ has appeared that does not match any of the measured samples.

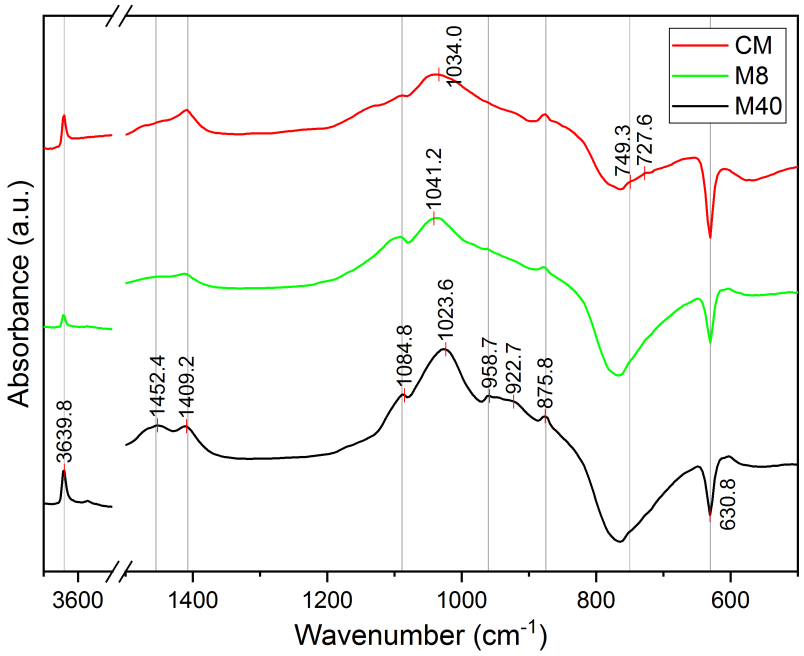


Figure 4.12.: Ambient ATR spectra of CM8, M8 and 40 samples

## 4.2. Reactivity

### 4.2.1. Temperature programmed reduction

#### 4.2.1.1. Olivine

In figure **??**, a TPR of the olivine samples is displayed. While the OF sample does not change the CO and the $CO_2$ concentrations drastically, a massive band can be discovered at a temperature of 600 °C on the OU sample. Besides this phenomenon, the rest of the shape of the $CO_2$ yield of the OF sample has a similar but less intense shape.

The conversion of OF kicks off at already 2%, which is a result of the smoothed signal of the massively staggering signal of the sample. However, after around 5:45 h and 600 °C, a comparably light increment of the CO conversion takes place. Noticeably, the $CO_2$ yield pattern differs from the conversion by showing a temperature-ramp related pattern. This behavior was repeated by almost all samples. With each rise of temperature beginning from 400 °C, the $CO_2$ yield increases. 800 °C delivers the highest $CO_2$ - yield.

The negative CO-conversion of the OU sample from the beginning until 3:30 h after the measurements kick-off can be characterized as a highly staggering signal. According to

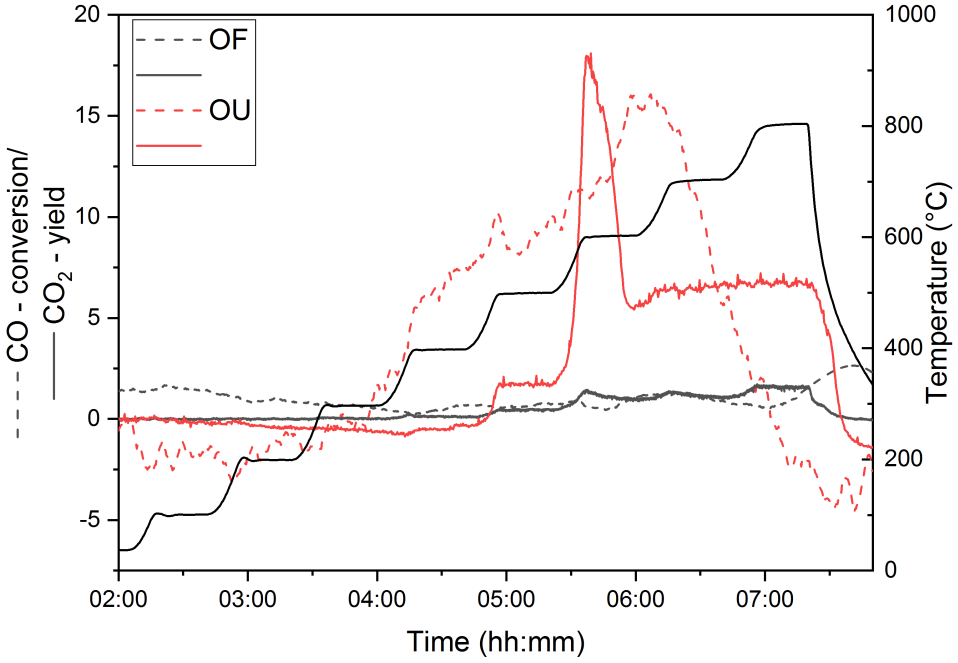


Figure 4.13.: TPR - CO conversion and $CO_2$ yields of the OF and OU samples

the signal, a CO well must be active under these thermodynamic and kinematic circumstances. The TPR reaches 200 °C after 3:30 h. At this state, an increase of the CO – conversion signal is visible. A light band at 500 °C can be seen after five hours resulting in a CO – conversion of 10%. The CO- conversion increases until a temperature of 700°C resulting in the maximum CO – conversion of 15%.

A difference was observed when the amount of OU in the micro-reactor was increased from 25 mg up to 40 mg. The "OU40mg" abbreviation refers to an OU sample with 40mg in the microreactor. While the conversion of CO is still staggering at temperatures between ambient temperature and 600°C, the conversion of CO and also the yield of $CO_2$ increase simultaneously with the beginning of 700°C. Both trends rise at 800 °C before they decrease drastically with the reduction of the temperature.

#### 4.2.1.2. Layered K-feldspar with bark-chicken manure mix as fuel

In figure **??**, the TPR CO – conversion and $CO_2$ – yields of the M8 and M40 are portrayed. Negative yields occur on the M8 sample indicating that CO was not consumed, but formed. In a temperature range between 400 – 700 °C, CO is consumed again until its formation begins again above 700°C. Nevertheless, it must be mentioned that the yield of $CO_2$ does not match the trend of the CO-conversion. The conversion and the yields given by the M40 sample can be linked together. Both curves display only small changes until a temperature of 700 °C. Following this, a significant rise in conversion and yield occurs. However, the decay does not occur at the same time. The conversion decreases

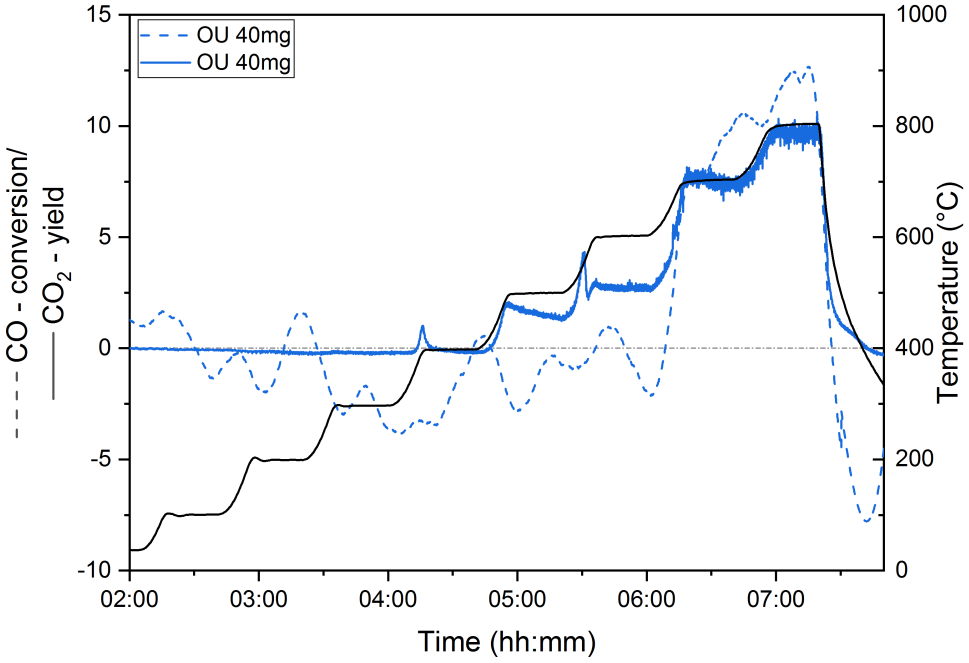


Figure 4.14.: TPR - CO conversion and $CO_2$ yields of the and OU 40 mg samples

already by reaching 800 °C while the yield stays constant with the temperature. Another interesting fact is the missing $CO_2$ release at 600°C.

### 4.2.2. Metal Oxides

In order to determine active sites of the layered bed materials, several adsorption experiments under controlled temperature and atmosphere were conducted. In the course of the experiment, various probe molecules were introduced into the reactor at ambient temperature. FT-IR measurements should prove the presence of the probe molecule on the surface of the layered bed materials. Unfortunately, no traces of any probe molecules were detected on any layered bed materials.

Since the experiments on the actual samples were unsuccessful, the presumed compounds on the surfaces were also investigated with Acetic Acid, MeOH, and $NH_3$ as probe molecules. The compounds were chosen as a result of the observed metal oxides on Raman and FT-IR spectroscopy.

All three probe molecules were active on CaO on the full temperature range. However, the adsorption of MeOH did not result in clearly visible MeOH bands. The spectrum displayed several band shifts and absorbance intensities. Especially the temperature range beginning from 400°C is noticeable. Initially, acetic acid shows its specific bands on $SiO_2$ until 100°C. This behavior switches into a difference in absorbance intensities in the 3200 $cm^{-1}$ to 3750 $cm^{-1}$. The application of $NH_3$ on ZnO results in a weak absorbance difference at a wavenumber of 3300 $cm^{-1}$. MgO shows no visible absorbance on the $NH_3$

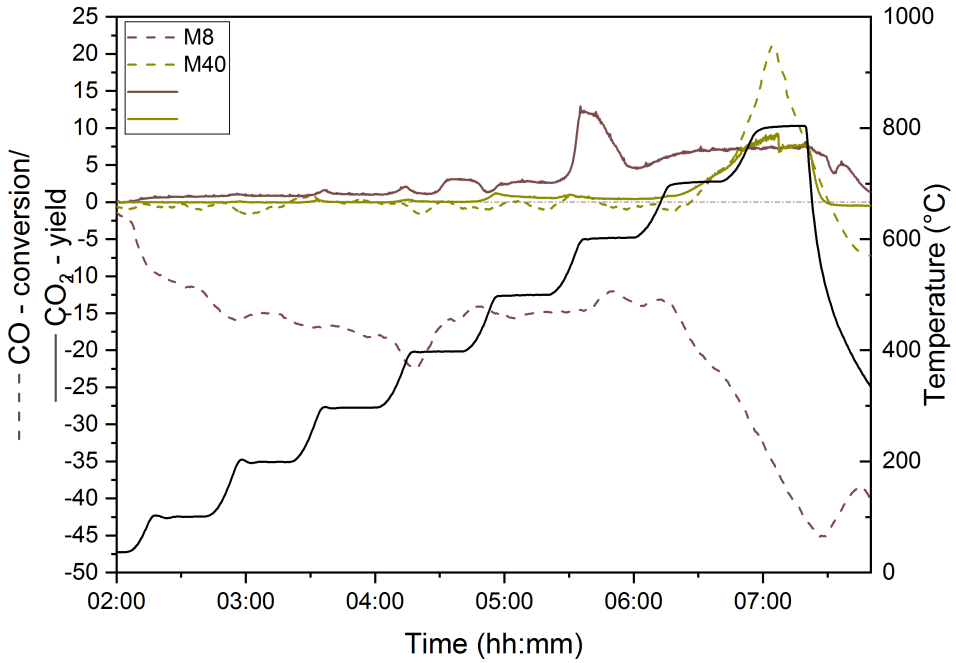


Figure 4.15.: TPR - CO conversion and $CO_2$ yields of the M8 and M40 samples

Table 4.1.: Investigated probe molecules in dependence of the temperature

| Temperature [°C] | Acetic Acid | MeOH | $NH_3$ |
|---|---|---|---|
| 40 | CaO, $CaCO_3$, MgO, $Fe_2O_3$, $SiO_2$ | CaO*, MgO, $SiO_2$ | CaO, ZnO* |
| 100 | CaO, $CaCO_3$, MgO, $Fe_2O_3$, $SiO_2$ | CaO*, MgO, $SiO_2$ | CaO, ZnO* |
| 200 | CaO, $CaCO_3$, MgO, $Fe_2O_3$, $SiO_2$* | CaO*, MgO, $SiO_2$ | CaO, |
| 300 | CaO, $CaCO_3$*, MgO, $Fe_2O_3$, $SiO_2$* | CaO*, MgO, $SiO_2$ | CaO, |
| 400 | CaO, MgO, $SiO_2$* | CaO*, MgO, $SiO_2$ | CaO, MgO* |
| 500 | CaO, MgO, $SiO_2$* | CaO*, MgO, $SiO_2$ | CaO, MgO* |

*..... unclarified activity

characteristic positions but displays a new band in around 2200 $cm^{-1}cm^{-1}$ beginning from 400°C. Samples that are marked with a (*) displayed an activity. However, the activity manifested itself with a shift of the bands towards a wavelength that does not match the sample of the corresponding probe molecule or the used sample either.

# 5. Discussion

## 5.1. Identification of Species

Raman and FT-IR ATR were used as independent techniques to detect the distributed compounds on the surfaces. All measurements were taken in arbitrary units and therefore cannot be quantified to concentrations. All spectra were assigned with literature in addition to self-measured reference samples consisting of chosen metal oxides.

Both, "OU – 3,5" in Figure 4.2 as well as "FF – 4" in Figure 4.5, were identified as $\alpha$-Quartz. The used FF contains several impurities with Na-Feldspar and $\alpha$-Quartz among them. An earlier contamination of OF before it was used is possible but should also lead to a detection of $\alpha$-Quartz in OF. However, this was not the case. Therefore, it is unclear where the $\alpha$-Quartz in OU originates from. [6, 89]

Ca was detected on every sample on both Raman and ATR measurements. More exposure time in the reactor results in a proportional increase of the Ca response on the Raman spectra of layered olivine and K-feldspar samples. Ca detected on CM8 and M40 but in another context resulting in a less comparative spectrum to the bark and olivine samples. A relatively high P-content originating from the feedstock was also discovered on CM8 and M40. $PO_4^{3-}$ and Ca related modes were associated with an Apatite related compound on the surface layers. This also results in a shift of $Ca^{2+}$ modes. $PO_4^{3-}$ was the dominant compound that was discovered on the CM8, M8, and M40 samples. Furthermore, $Fe_2O_3$ and MnO were observed on OU. Nevertheless, also traces of several other metal oxides and carbonates are possible and indicated by the Raman results. Taking this into account, a mixture of several metal oxides, metal carbonates, and other impurities could result in a superposition of the specific bands in a brief range of Raman shift.

It is presumable that Ca occurs as CaO as well as $Ca(OH)_2$ and $CaCO_3$ on OU, B8, and B32. All three compounds are indicated by Raman and mostly supported by observed CaO- and $Ca(OH)_2$ modes on ATR. CM8, M8, and M40 also carry CaO and $CaCO_3$ on their surfaces, but their spectra are shifted by $PO_4^{3-}$ modes forming a hydroxyapatite spectra. [69]

The intensity of the $SiO_4$ modes observed in Raman as well as in ATR has decreased from OF to OU. This phenomenon was found to be linked to a rise of intensities of Ca related modes as a result of the coverage of the outer surface layer with new Ca compounds. Since no shift of the $SiO_4$ mode was observed, it is presumed that the $SiO_4$ compound is not affected during the accumulation of Ca.

The B8 and B32 samples show the same development in a lighter form. It can be assumed that the tectosilicate compound is not involved in the rise of the Ca concentration.

Table 5.1.: Summary of the observed compounds on Raman of the investigated bed materials

| Compound | Raman Shift ($cm^{-1}$) | Sample | |
|---|---|---|---|
| $Fe_2O_3$ | 291 | OF, OU | |
| | 1070 | OU | |
| | 1318 | OF, OU | |
| $PO_4^{3-}$ | 433 | CM8, M8, M40 | [87] |
| | 591 | CM8, M8, M40 | [87] |
| | 960 | B8, B32, CM8, M8, M40 | [87] |
| | 984 | CM8, M8, M40 | [87] |
| | 1142 | CM8, M8, M40 | [69] |
| CaO | 355 | OU, CM8, M8, M40 | |
| | [550-750] | OU, B8, B32, CM8, M8, M40 | |
| | 619 | CM8, M8, M40 | [8] |
| $CaCO_3$ | 153 | OU, B8, B32, CM8, M8, M40 | |
| | 712 | OU, CM8, M8, M40 | |
| | 1086 | OU, B8, B32, CM8, M8, M40 | |
| MgO | 275 | OU | |
| MnO | 475 | OU, B8, B32 | |
| $OH^-$ | 3619 | OU, B8, CM8, M8, M40 | |

Table 5.2.: Summary of the observed compounds on ATR of the investigated bed materials

| Compound | Raman Shift ($cm^{-1}$) | Sample | |
|---|---|---|---|
| $PO_4^{3-}$ | 958 | CM8, M8, M40 | [12] |
| | 1000 - 1100 | CM8, M8, M40 | [12] |
| CaO | 875 | OU, B8, B32 | [12] |
| | 1132 | B8, B32, CM8, M8, M40 | |
| | 1400 - 1500 | OU, B8, B32, CM8, M8, M40 | |
| $CaCO_3$ | 771 | B8 | |
| $OH^-$ | 3637 | OU, B32, CM8, M8, M40 | [12] |

Again, the tectosilicate related intensities are decreased on the used samples while Ca-related modes are more intense with increased bed material reactor exposure time. A thicker layer between the actual tectosilicate compound would result in less intensity.

Even though the spectra of CM8, M8, and M40 differ from the other used samples, they mostly share the same development. CM8 leaves only marginal tectosilicate mode intensities over. With this as an indication for CM8 to have the thickest ash barrier for the penetrating laser light, it can be concluded that it also has the thickest ash layer. M8 and M40 share a common but less distinctive result with low differences. The major difference between M8 and M40 was found in a variation of the intensity of CaO and $PO_4^{3-}$ modes, which rise with the exposure time in the reactor. Also, a decrease of $CaCO_3$ and $Ca(OH)_2$ modes were observed.
All detected modes are listed and linked to related compounds in table 5.1 for Raman and table 5.2 for ATR.

Table 5.3.: Overview of the initial appearance of the stretching in the range of a Raman shift between 1200 – 1700 $cm^{-1}$ during the temperature treatment.

| Temperature [°C] | OF | FF | OU | B8 | B32 | CM8 | M8 | M40 |
|---|---|---|---|---|---|---|---|---|
| 25 | - | - | - | - | - | d.n.p. | - | - |
| 100 | - | - | ✓ | - | - | | - | - |
| 300 | - | - | ✓ | ✓ | - | | ✓ | - |
| 500 | ✓ | - | ✓ | ✓ | ✓ | | ✓ | ✓ |

d.n.p. = detection not possible

Neither Raman nor ATR could provide the actual concentration of the discovered compounds on the surface. Nevertheless, an increase of intensities can be assumed to be a rise in the concentration of molecular quantities. Starting with Raman, the bed materials used in a feedstock that gasifies/combusts woody feedstocks show a common increase of a stretching in the range of 550 $cm^{-1}$ and 750 $cm^{-1}$ and a strong band at 1085 $cm^{-1}$ and 3620 $cm^{-1}$ with the rising exposure time of the bed material in the reactor. These spectra were matched to CaO, $OH^-$, and $CO_3^{-2}$ modes. This results in a co-existence of CaO, $Ca(OH)_2$, and $CaCO_3$. Though, it is questionable if the Ca-compound is always present as CaO or in a different form. In addition, $PO_4^{3-}$ was found as a result of the utilization of P-rich feedstocks. Following this, the number of possible compounds that could take action on the surface is increased. [14]
Given the fact that the reactor is operated around 800 °C further investigations in this thermodynamic environment are suggested. A first investigation up to 500 °C did not result in a shift of the spectra but in a difference in the intensities. This indicated an influence on the crystalline structure of the available compounds.

## 5.2. Activity

The major result of the temperature treatment can be observed in the Raman spectra on the range of 1200 to 1700 $cm^{-1}$ of every used sample. The spectra show a comparably large intensity of two bands at higher temperatures beginning between 100 and 500 °C.

The observed bands in this range were linked to carbonaceous deposits on the sample. Those could either be molecules that consist of C-C or C-H bonds. No sample shows any signs of carbonic compounds on the surface besides the observed carbonates. However, a release of volatiles, which are trapped under the surface of the samples alongside to desorption mechanisms of $CO_2$ is possible. Furthermore, the spectra of the TPR analysis support this statement. The WGS reaction should result in an equivalent consumption of CO and formation of $CO_2$. Besides the negative CO – conversion on some samples (Figure 4.15), the $CO_2$ formation does not match the CO trend of the reaction on the most samples. The actual WGS reaction was only observed on M40 and “OU40mg” in the range of 700 – 800 °C, with yields around 15% on both samples (Figure 4.14, Figure 4.15). Both samples have the highest content of ash and BET surface areas. The observed quantity of $CO_2$ seems to be rather connected to the surface morphology than the actual chemical compounds on the surface. [26, 44, 76]

In order to evaluate the thermodynamic and kinematic properties in terms of the WGS reaction, several metal oxides were investigated. Especially CaO, and MgO show positive affinities to act as a basic center at elevated temperatures. Li et al. support this statement by reporting that CaO enhances the WGS reaction by acting as a catalyst by attracting $H_2O$ and forming OH*, H* radicals. [57] Hydrogen molecules get attached to the basic sites of Ca. Also, the formation of CO* radicals is reported. However, the investigations of this work do not confirm any interactions between CaO and CO. The formation of $CaCO_3$ can be a limiting factor. It occupies active sites of CaO and its formation will lead to a lower porosity of the particles. The $PO_4^{3-}$ content could have a similar effect by occupying some basic sites of Ca. Therefore, a strong driving force towards a layer formation might reduce the reactivity of Ca on bed materials with a low reactor exposure time. Regarding the used bed materials, it can be assumed that the $CO_2$ releases are more connected to the trapped carbonaceous deposits. Only the ash-rich samples M40 and "OU40mg" can be assumed to provide the necessary kinematic conditions in terms of surface area. [33,57]

Fe can be assumed to be a reason for OF's initial activity during WGS reaction. It is also used as a high temperature catalyst in WGS reaction. MgO was only observed on OU. This is an indication that it originates from the fresh sample and not from the ash.

## 5.3. Layer Formation

The layer formation processes for woody feedstocks on olivine and K-feldspar have already been reportedly proposed. However, it is obvious that P does play a role in the formation of the surface environment on the mixed (M) and the chicken manure (CM8) samples. Regarding the Raman spectra, it can be presumed that especially calcium phosphates are located on the very surface of the particles. Ren et al. [72] reported that P may have a significant influence in preventing K to be consumed into the gaseous phase in the reactor. Grimm et al. also discovered a decreased melting behavior due to extended amounts of P in the reactor. [33] It is already known that K supports Ca diffusion towards the particle core. This would result in a formation of Ca rich central layers. In this case, P might act as an important K attractor. However; it must be also mentioned that no spectra found a compound that consists of K-Ca-P. So further research must take place in order to clarify if such an interaction can be observed. Furthermore, it must be considered that the WGS reaction takes place on the surface of the particles, and Ca was already revealed to have a catalytic effect on it. The presence of $PO_4^{3-}$ must also be investigated.

## 5.4. Limitations of the Methods

### 5.4.1. Raman and FT-IR

Raman is not able to detect every mode that occurs due to the monochromatic light. Following this, FT-IR measurements have to be done and vice versa. A more specific surface assessment of the surface was demanded, which is less precise on Raman and FT-IR than

other technologies like XPS. Both technologies penetrate their samples significantly more than 10 nm into the particle. Furthermore, the temperature limit of 500°C was a negative feature which did now allow to come closer to the actual used gasifying temperature conditions. Distinguishing between metal oxides can be challenging due to their similar results within common Raman shifts in the fingerprint range. Further drawbacks are the massive fluorescence on several samples resulting in a very noisy signal and fact that a quantitative analysis was not possible.

### 5.4.2. Precision of QIC 20 – Mass Spectrometer

He as a carrier gas has a low m/z ratio close to $H_2$. Due to the ionization of He, it is possible that some of it was detected as $H_2$ influencing the final result of it. A similar problem was found for $CH_4$ and $H_2O$. In the following, only the $CO_2$ signal was considered to be really reliable. The stability of the measurement signal was also a reported problem. Another major drawback was the very noisy signal. Therefore, a substantial bias had to be accepted.

# 6. Conclusion

Ultimately, all results and the researched statements can be summarized in the following conclusion:

- The chemical composition and the share of the ash of the feedstock are a major influence on the distribution of the chemical compounds on the surface of the bed material that is exposed to the reactor. Eight samples were investigated whereof six were used in the WGS reaction in the reactor. CM8 provides the strongest intensities, followed by the mixed samples. This corresponds with the amount of ash their feedstocks generate. [10]

- Especially Ca-compounds were observed on all used samples appearing as CaO, $Ca(OH)_2$ as well as $CaCO_3$. Bed materials that were exposed to chicken manure also inherit $CaPO_4^{3-}$ and possibly other $PO_4^{3-}$-compounds. Comparably lower amounts of MgO and other Metal Oxides have also been found.

- It is assumed that the layer formation mechanism is influenced by the P-content of the feedstock. The appearance of Ca is certainly modified due to the presence of P. Nevertheless, the interaction of K, Ca, and P has to be investigated more in detail.

- CaO is catalytically active. It generates OH* and O* radicals. It is reported to have the capability to generate CO* radicals as well. However, the attempt to adsorb CO failed on all samples and metal oxides in this work.

- Due to the different intensities on the Raman spectrum at high temperatures, it is presumed that temperature influences the crystalline structure of the bed materials. Besides that, it can also be presumed that higher temperatures increase the concentration of oxides over carbonates due to the calcinating effect.

- An activity of the samples was only detected on some samples by the utilization of a TPR. A very limited and non-selective reaction was recorded, while no interaction was observed with other methods. However, a substitution of the bed materials with CaO and MgO indicates the capability of a catalytic activity of the bed materials.

- Carbonaceous compounds are revealed at higher temperatures. It is assumed that carbonaceous deposits are trapped under the surface of the bed materials.

- In order to obtain a complete characterization of the influence on the use of olivine as well as K-feldspar in the DFB gasifier, further quantitative investigations are suggested. It can be stated that Raman, as well as FT-IR, are precise enough for a qualitative detection of compounds on the surface. However, as the surface is more demanded in this objective a more selective analytic method can provide even more precise results.

- The variation of excess steam should be investigated on the operation of the DFB gasifier in order to evaluate a suitable ratio of possible active sites to steam.

# Bibliography


[1] Abdalla M. Abdalla, Shahzad Hossain, Ozzan B. Nisfindy, Atia T. Azad, Mohamed Dawood, and Abul K. Azad. Hydrogen production, storage, transportation and key challenges with applications: A review. *Energy Conversion and Management*, 165(March):602–627, 2018.

[2] Fouad Al-Mansour and Jaroslaw Zuwala. An evaluation of biomass co-firing in Europe. *Biomass and Bioenergy*, 34(5):620–629, 2010.

[3] Wulf Amelung, Hans-Peter Blume, Heiner Fleige, Rainer Horn, Ellen Kandeler, Ingrid Kögel-Knabner, Ruben Kretzschmar, Karl Stahr, and Berndt-Michael Wilke. *Anorganische Komponenten der Böden – Minerale und Gesteine*, pages 11–62. 2018.

[4] A Andoni. *A flat model approach to Ziegler-Natta olefin polymerization catalysts*. Dissertation, Technische Universiteit Eindhoven, 2009.

[5] Aprentas. *Laborpraxis Band 4: Analytische Methoden*. Springer International Publishing, Cham, 2017.

[6] Jean F. Asell and Malcolm Nicol. Raman Spectrum of $\alpha$ Quartz at High Pressures. *The Journal of Chemical Physics*, 49(12):5395–5399, 1968.

[7] Tobias Aurelio and Julio Diaz. Heat Waves, Human Health, and Climate Change. In *Global Environmental Change*, chapter Heat Waves, pages 447–453. 2014.

[8] Ayorinde Awonusi, Michael D. Morris, and Mary M.J. Tecklenburg. Carbonate assignment and calibration in the Raman spectrum of apatite. *Calcified Tissue International*, 81(1):46–52, 2007.

[9] Md Azhar Uddin, Hiroshi Tsuda, Shengji Wu, and Eiji Sasaoka. Catalytic decomposition of biomass tars with iron oxide catalysts. *Fuel*, 87(4-5):451–459, 2008.

[10] Mustafa Balat. Production of bioethanol from lignocellulosic materials via the biochemical pathway: A review. *Energy Conversion and Management*, 52(2):858–875, 2011.

[11] Mattia Bartoli, Luca Rosi, Marco Frediani, Andrea Undri, and Piero Frediani. Depolymerization of polystyrene at reduced pressure through a microwave assisted pyrolysis. *Journal of Analytical and Applied Pyrolysis*, 113:281–287, 2015.

[12] Liga Berzina-Cimdina and Natalija Borodajenko. Research of Calcium Phosphates Using Fourier Transform Infrared Spectroscopy. *Infrared Spectroscopy - Materials Science, Engineering and Technology*, 2012.

[13] A. V. Bridgwater. Review of fast pyrolysis of biomass and product upgrading. *Biomass and Bioenergy*, 38:68–94, 2012.

[14] Nicolae Buzgar and A. I. Apopei. The Raman study of certain K-Na Micas. 1(1973):45–49, 2009.

[15] Stefan Candefjord. *Combining the Tactile Resonance Method and Raman Spectroscopy for Tissue Characterization towards Prostate Cancer Detection.* Dissertation, Lulea University of Technology, 2011.

[16] A. Chopelas. Single crystal Raman spectra of forsterite, fayalite, and monticellite. *American Mineralogist*, 76(7-8):1101–1109, 1991.

[17] Maria Joana Neiva; Correia and David Mateus, M. Margarida; Fernandes, Maria Cristina; Riazi, M.R.; Chiaramonti. Chemistry and Nature of Biofuels. In M.R. Riazi and David Chiaramonti, editors, *Biofuels Production and Processing Technology*, pages 11–48. CRC Press, Boca Raton : Taylor & Francis, a CRC title, part of the Taylor & Francis imprint, a member of the Taylor & Francis Group, the academic division of T&F Informa, plc, 2018., oct 2017.

[18] Trine M.H. Dabros, Magnus Zingler Stummann, Martin Høj, Peter Arendt Jensen, Jan Dierk Grunwaldt, Jostein Gabrielsen, Peter M. Mortensen, and Anker Degn Jensen. Transportation fuels from biomass fast pyrolysis, catalytic hydrodeoxygenation, and catalytic fast hydropyrolysis. *Progress in Energy and Combustion Science*, 68:268–309, 2018.

[19] A. Davydov. *Molecular Spectroscopy of Oxide Catalyst.* Edmonton: Wiley, 2003.

[20] Vaibhav Dhyani and Thallada Bhaskar. A comprehensive review on the pyrolysis of lignocellulosic biomass. *Renewable Energy*, 129:695–716, 2018.

[21] L. Di Felice, C. Courson, D. Niznansky, P. U. Foscolo, and A. Kiennemann. Biomass gasification with catalytic tar reforming: A model study into activity enhancement of calcium- and magnesium-oxide-based catalytic materials by incorporation of iron. *Energy and Fuels*, 24(7):4034–4045, 2010.

[22] Max Diem. *Modern Vibrational Spectroscopy and Micro-Spectroscopy.* John Wiley & Sons, Ltd, Chichester, UK, aug 2015.

[23] Myriam Eckes, Benoit Gibert, Domingos de Sousa Meneses, Mohammed Malki, and Patrick Echegut. High-temperature infrared properties of forsterite. *Physics and Chemistry of Minerals*, 40(4):287–298, 2013.

[24] Eurostat. *Energy, transport and environment indicators. 2018 edition.* 2018.

[25] H. Fatehi, Y. He, Z. Wang, Z. S. Li, X. S. Bai, M. Aldén, and K. F. Cen. LIBS measurements and numerical studies of potassium release during biomass gasification. *Proceedings of the Combustion Institute*, 35(2):2389–2396, 2015.

[26] A. C. Ferrari and J. Robertson. Resonant Raman spectroscopy of disordered, amorphous, and diamondlike carbon. *Physical Review B - Condensed Matter and Materials Physics*, 64(7):1–13, 2001.

[27] Andrea Foglar. *Asche - Bettmaterial - Interaktionen während thermischer Wirbelschichtumwandlungen von Rinde , Gülle und landwirtschaftlichen Abfällen*. Master's thesis, Technische Universität Wien, 2018.

[28] John J. Freeman, Alian Wang, Karla E. Kuebler, Bradley L. Jolliff, and Larry A. Haskin. Characterization of natural feldspars by raman spectroscopy for future planetary exploration. *Canadian Mineralogist*, 46(6):1477–1500, 2008.

[29] Manfred H. Gey. *Instrumentelle Analytik und Bioanalytik*. Springer-Lehrbuch. Springer Berlin Heidelberg, Berlin, Heidelberg, 2015.

[30] F. M. Gírio, C. Fonseca, F. Carvalheiro, L. C. Duarte, S. Marques, and R. Bogel-Łukasik. Hemicelluloses for fuel ethanol: A review. *Bioresource Technology*, 101(13):4775–4800, 2010.

[31] Jens Götze and Matthias Göbbels. *Einführung in die Angewandte Mineralogie*. Springer Berlin Heidelberg, Berlin, Heidelberg, 2017.

[32] Peter R. Griffiths and James A. de Haseth. *Fourier transform infrared spectrometry*. John Wiley and Sons, Inc, Hoboken, New Jersey, 2007.

[33] Alejandro Grimm, Nils Skoglund, Dan Boström, Christoffer Boman, and Marcus Öhman. Influence of phosphorus on alkali distribution during combustion of logging residues and wheat straw in a bench-scale fluidized bed. *Energy and Fuels*, 26(5):3012–3023, 2012.

[34] John Grotzinger and Thomas Jordan. Die Baustoffe der Erde: Minerale und Gesteine. In *Allgemeine Geologie*. 2017.

[35] H. Hassan, J. K. Lim, and B. H. Hameed. Recent progress on biomass co-pyrolysis conversion into high-quality bio-oil. *Bioresource Technology*, 221:645–655, 2016.

[36] Fabian Havlik. *Catalytic Investigations Regarding Alternative Bed Materials for Dual Fluidized Bed Gasification of Biomass*. Maste's thesis, Technische Universität Wien, 2015.

[37] Hanbing He, Xiaoyan Ji, Dan Boström, Rainer Backman, and Marcus Öhman. Mechanism of Quartz Bed Particle Layer Formation in Fluidized Bed Combustion of Wood-Derived Fuels. *Energy and Fuels*, 30(3):2227–2232, 2016.

[38] Hanbing He, Nils Skoglund, and Marcus Öhman. Time-Dependent Crack Layer Formation in Quartz Bed Particles during Fluidized Bed Combustion of Woody Biomass. *Energy and Fuels*, 31(2):1672–1677, 2017.

[39] Hanbing He, Nils Skoglund, and Marcus Öhman. Time-Dependent Layer Formation on K-Feldspar Bed Particles during Fluidized Bed Combustion of Woody Fuels. *Energy and Fuels*, 31(11):12848–12856, 2017.

[40] Willinton Y. Hernández, Jeroen Lauwaert, Pascal Van Der Voort, and An Verberckmoes. Recent advances on the utilization of layered double hydroxides (LDHs) and related heterogeneous catalysts in a lignocellulosic-feedstock biorefinery scheme. *Green Chemistry*, 19(22):5269–5302, 2017.

[41] John W. Honour. Benchtop mass spectrometry in clinical biochemistry. *Annals of Clinical Biochemistry*, 40(6):628–638, nov 2003.

[42] IEA. Global Energy and CO2 Status Report. *Oecd-Iea*, (March):15, 2018.

[43] IPCC:, O. Hoegh-Guldberg, D. Jacob, M. Taylor, M. Bindi, S. Brown, I. Camilloni, A. Diedhiou, R. Djalante, K.L. Ebi, F. Engelbrecht, J. Guiot, Y. Hijioka, S. Mehrotra, A. Payne, S.I. Seneviratne, A. Thomas, R. Warren, and G. Zhou. , 2018: Impacts of 1.5ºC Global Warming on Natural and Human Systems. In: Global Warming of 1.5°C. An IPCC Special Report on the impacts of global warming of 1.5°C above pre-industrial levels and related global greenhouse gas emission pathways. Technical report, 2018.

[44] Daniel Eugen Janisch. *Surface morphology and catalyst characterization of bed material in dual fluidized bed biomass gasification*. Master's thesis, Technische Universität Wien.

[45] Gligor Jovanovski and Petre Makreski. Minerals from macedonia. XXX. Complementary use of vibrational spectroscopy and X-ray powder diffraction for spectra-structural study of some cyclo-, phyllo- and tectosilicate minerals. A review. *Macedonian Journal of Chemistry and Chemical Engineering*, 35(2):125–155, 2016.

[46] M Kaltschmitt, H Hartmann, and H Hofbauer. *Energie aus Biomasse*. Springer Berlin Heidelberg, Berlin, Heidelberg, 2016.

[47] Stefan Kern, Christoph Pfeifer, and Hermann Hofbauer. Reactivity tests of the water-gas shift reaction on fresh and used fluidized bed materials from industrial DFB biomass gasifiers. *Biomass and Bioenergy*, 55:227–233, 2013.

[48] Friedrich Kirnbauer and Hermann Hofbauer. Investigations on bed material changes in a dual fluidized bed steam gasification plant in Güssing, Austria. *Energy and Fuels*, 25(8):3793–3798, 2011.

[49] B. A. Kolesov and C. A. Geiger. A Raman spectroscopic study of Fe-Mg olivines. *Physics and Chemistry of Minerals*, 31(3):142–154, 2004.

[50] Meng Kong, Jinhua Fei, Shuai Wang, Wen Lu, and Xiaoming Zheng. Influence of supports on catalytic behavior of nickel catalysts in carbon dioxide reforming of toluene as a model compound of tar from biomass gasification. *Bioresource Technology*, 102(2):2004–2008, jan 2011.

[51] Joanna Kryca, Juraj Priščák, Joanna Łojewska, Matthias Kuba, and Hermann Hofbauer. Apparent kinetics of the water-gas-shift reaction in biomass gasification using ash-layered olivine as catalyst. *Chemical Engineering Journal*, 346(November 2017):113–119, 2018.

[52] Matthias Kuba, Hanbing He, Friedrich Kirnbauer, Dan Boström, Marcus Öhman, and Hermann Hofbauer. Deposit build-up and ash behavior in dual fluid bed steam gasification of logging residues in an industrial power plant. *Fuel Processing Technology*, 139(2015):33–41, 2015.

[53] Matthias Kuba, Hanbing He, Friedrich Kirnbauer, Nils Skoglund, Dan Boström, Marcus Öhman, and Hermann Hofbauer. Mechanism of layer formation on olivine bed particles in industrial-scale dual fluid bed gasification of wood. *Energy and Fuels*, 30(9):7410–7418, 2016.

[54] Matthias Kuba and Hermann Hofbauer. Experimental parametric study on product gas and tar composition in dual fluid bed gasification of woody biomass. *Biomass and Bioenergy*, 115(April 2018):35–44, 2018.

[55] Karla E. Kuebler, Bradley L. Jolliff, Alian Wang, and Larry A. Haskin. Extracting olivine (Fo-Fa) compositions from Raman spectral peak positions. *Geochimica et Cosmochimica Acta*, 70(24):6201–6222, 2006.

[56] Krishendu Kundu, Tamashree Chatterjee, Ayoma Bhattacharyya, Madhuka Roy, and Ajit Kaur. Thermochemical Conversion of Biomass to Bioenergy: A Review. In *Prospects of Alternative Transportation Fuels*, page Prospects of Alternative Transportation Fuels. Springer Nature Singapore Pte Ltd., Ludhiana, 2018.

[57] Bin Li, Liangyuan Wei, Haiping Yang, Xianhua Wang, and Hanping Chen. The enhancing mechanism of calcium oxide on water gas shift reaction for hydrogen production. *Energy*, 68:248–254, 2014.

[58] Linna Li, Qiangqiang Ren, Shiyuan Li, and Qinggang Lu. Effect of phosphorus on the behavior of potassium during the Co-combustion of wheat straw with municipal sewage sludge. *Energy and Fuels*, 27(10):5923–5930, 2013.

[59] Alya Limayem and Steven C. Ricke. Lignocellulosic biomass for bioethanol production: Current perspectives, potential issues and future prospects. *Progress in Energy and Combustion Science*, 38(4):449–467, 2012.

[60] Chanchal Loha, Malay K. Karmakar, Santanu De, and Pradip K. Chatterjee. Gasifiers: Types, Operational Principles and Commercial Forms. In *Coal and Biomass Gasification: Recent Advances and Future Challenges*, pages 63–91. Springer Nature Singapore Pte Ltd., Durgapur, 2018.

[61] Aneta Magdziarz, Ajay K. Dalai, and Janusz A. Koziński. Chemical composition, character and reactivity of renewable fuel ashes. *Fuel*, 176:135–145, 2016.

[62] Gregor Markl. *Minerale und Gesteine*. Springer Berlin Heidelberg, Berlin, Heidelberg, 2015.

[63] Jonathan R. Mielenz. Ethanol production from biomass: Technology and commercialization status. *Current Opinion in Microbiology*, 4(3):324–329, 2001.

[64] J. W. Niemantsverdriet. *Spectroscopy in Catalysis*. Wiley-VCH Verlag GmbH & Co. KGaA, Eindhoven, 2003.

[65] Poonam Singh Nigam and Anoop Singh. Production of liquid biofuels from renewable resources. *Progress in Energy and Combustion Science*, 37(1):52–68, 2011.

[66] Thomas Nordgreen, Truls Liliedahl, and Krister Sjöström. Metallic iron as a tar breakdown catalyst related to atmospheric, fluidised bed gasification of biomass. *Fuel*, 85(5-6):689–694, 2006.

[67] Martin Okrusch and Siegfried Matthes. *Mineralogie*. Springer-Lehrbuch. Springer Berlin Heidelberg, Berlin, Heidelberg, 2010.

[68] Prakash Parthasarathy and K. Sheeba Narayanan. Hydrogen production from steam gasification of biomass: Influence of process parameters on hydrogen yield - A review. *Renewable Energy*, 66(November 2019):570–579, 2014.

[69] G. Penel, G. Leroy, C. Rey, and E. Bres. MicroRaman spectral study of the PO4 and CO3 vibrational modes in synthetic and biological apatites. *Calcified Tissue International*, 63(6):475–481, 1998.

[70] Patrycja Piotrowska, Maria Zevenhoven, Kent Davidsson, Mikko Hupa, Lars Erik Åmand, Vesna Barišić, and Edgardo Coda Zabetta. Fate of alkali metals and phosphorus of rapeseed cake in circulating fluidized bed boiler part 2: Cocombustion with coal. *Energy and Fuels*, 24(8):4193–4205, 2010.

[71] R. Prathiba, M. Shruthi, and Lima Rose Miranda. Pyrolysis of polystyrene waste in the presence of activated carbon in conventional and microwave heating using modified thermocouple. *Waste Management*, 76:528–536, 2018.

[72] Qiangqiang Ren and Linna Li. Co-combustion of Agricultural Straw with Municipal Sewage Sludge in a Fluidized Bed: Role of Phosphorus in Potassium Behavior. *Energy and Fuels*, 29(7):4321–4327, 2015.

[73] R. Saidur, E. A. Abdelaziz, A. Demirbas, M. S. Hossain, and S. Mekhilef. A review on biomass as a fuel for boilers. *Renewable and Sustainable Energy Reviews*, 15(5):2262–2289, 2011.

[74] Tadaaki Shimizu, Jun Han, Sunyong Choi, Laehyun Kim, and Heejoon Kim. Fluidized-bed combustion characteristics of cedar pellets by using an alternative bed material. *Energy and Fuels*, 20(6):2737–2742, 2006.

[75] Ewen Smith and Geoffrey Dent. *Modern Raman Spectroscopy - A Practical Approach*. John Wiley & Sons, Ltd, Chichester, UK, dec 2004.

[76] G. Socrates. *Infrared and Raman characteristic group frequencies. Tables and charts*. 2001.

[77] H. Sogawa, C. Koike, H. Chihara, H. Suto, S. Tachibana, A. Tsuchiyama, and T. Kozasa. Infrared reflection spectra of forsterite crystal. *Astronomy & Astrophysics*, 451(1):357–361, may 2006.

[78] Michael Stöcker. Biofuels and biomass-to-liquid fuels in the biorefinery: Catalytic conversion of lignocellulosic biomass using porous materials. *Angewandte Chemie - International Edition*, 47(48):9200–9211, 2008.

[79] Karl Strauß. *Kraftwerkstechnik*. Springer Berlin Heidelberg, Berlin, Heidelberg, 2009.

[80] Zhongxin Tan and Anders Lagerkvist. Phosphorus recovery from the biomass ash: A review. *Renewable and Sustainable Energy Reviews*, 15(8):3588–3602, 2011.

[81] Christopher J. Thompson, John S. Loring, Kevin M. Rosso, and Zheming Wang. Comparative reactivity study of forsterite and antigorite in wet supercritical CO2 by in situ infrared spectroscopy. *International Journal of Greenhouse Gas Control*, 18:246–255, 2013.

[82] Rutger A. van Santen, editor. *Modern Heterogeneous Catalysis*. Wiley-VCH Verlag GmbH & Co. KGaA, Weinheim, Germany, apr 2017.

[83] Stanislav V. Vassilev, David Baxter, Lars K. Andersen, and Christina G. Vassileva. An overview of the chemical composition of biomass. *Fuel*, 89(5):913–933, 2010.

[84] Stanislav V. Vassilev, David Baxter, and Christina G. Vassileva. An overview of the behaviour of biomass during combustion: Part I. Phase-mineral transformations of organic and inorganic matter. *Fuel*, 112:391–449, 2013.

[85] Stanislav V. Vassilev, David Baxter, and Christina G. Vassileva. An overview of the behaviour of biomass during combustion: Part II. Ash fusion and ash formation mechanisms of biomass types. *Fuel*, 117(PART A):152–183, 2014.

[86] Stanislav V. Vassilev, Christina G. Vassileva, Yun Cai Song, Wen Ying Li, and Jie Feng. Ash contents and ash-forming elements of biomass and their significance for solid biofuel combustion. *Fuel*, 208:377–409, 2017.

[87] Christian Vogel, Christian Adam, and Don McNaughton. Determination of phosphate phases in sewage sludge ash-based fertilizers by Raman microspectroscopy. *Applied Spectroscopy*, 67(9):1101–1105, 2013.

[88] K. Wagner, C. Hammerl, M. Kuba, and H. Hofbauer. Time-dependent catalytic activation of inactive k-feldspar by layer formation during fluidized bed conversion with residual fuels. In *European Biomass Conference and Exhibition Proceedings*, number May 2019, pages 779–785, 2019.

[89] Katharina Wagner, Anna Magdalena Mauerhofer, Matthias Kuba, and Hermann Hofbauer. Suitability of K-feldspar as Alternative Bed Material in Dual Fluidized Bed Steam Gasification in Combination with Ash-Rich Feedstocks. *23rd International Conference on FBC*, 2018.

[90] Yang Zhang, Xun Gong, Biao Zhang, Wenqiang Liu, and Minghou Xu. Potassium catalytic hydrogen production in sorption enhanced gasification of biomass with steam. *International Journal of Hydrogen Energy*, 39(9):4234–4243, 2014.

# List of Figures

# List of Tables

# A. Appendix

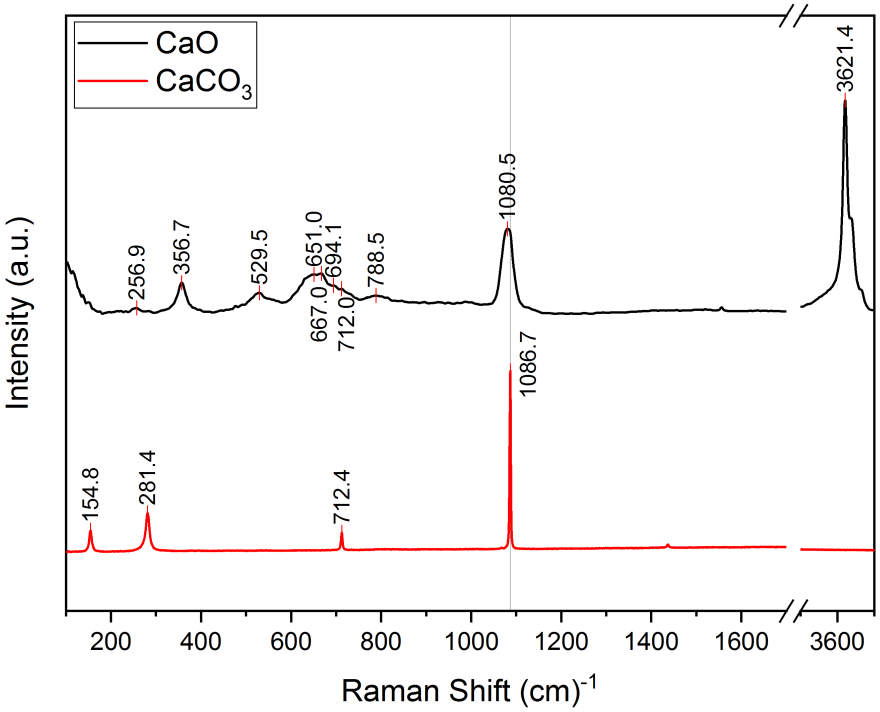


Figure A.1.: Ambient Raman spectra of CaO and $CaCO_3$

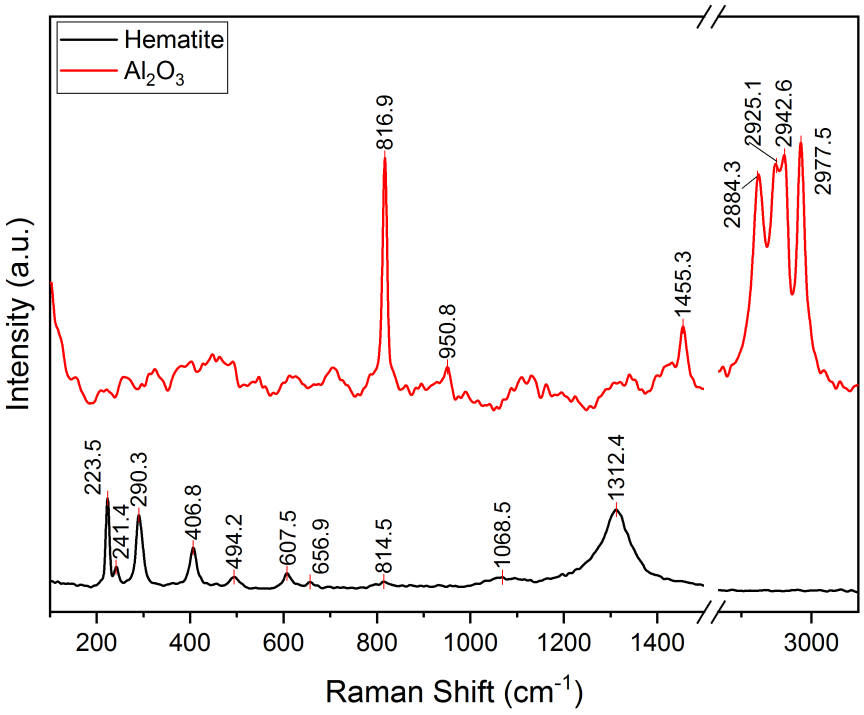


Figure A.2.: Ambient Raman spectra of $Al_2O_3$ and Hematite

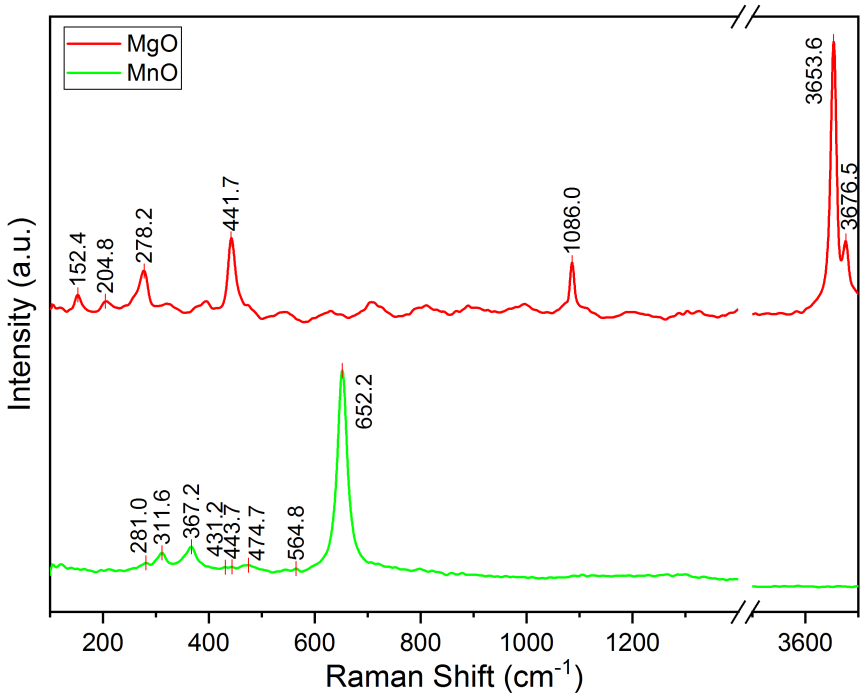


Figure A.3.: Ambient Raman spectra of MgO and MnO

Table A.1.: List of all discovered Raman modes derived from non-used bed materials

| Functional group | Raman Shift ($cm^{-1}$) | Sample | |
|---|---|---|---|
| $SiO_4$ | 225($Fe^{+2}$/Mg) | OF, OU | [49] |
| | 244($Fe^{+2}$/Mg) | OF | [49] |
| | 299($Fe^{+2}$/Mg) | OF | [49] |
| | 303($Fe^{+2}$/Mg) | OF, OU | [49] |
| | 326($Fe^{+2}$/Mg) | OF, OU | [49] |
| | 408 | OF | [49] |
| | 432 | OF | [49] |
| | 545 | OF, OU | [49] |
| | 584 | OF, OU | [49] |
| | 608 | OF, OU | [49] |
| | 822 | OF, OU | [49] |
| | 857 | OF, OU | [49] |
| | 881 | OF, OU | [49] |
| | 920 | OF, OU | [49] |
| | 963 | OF, OU | [49] |
| $Fe_2O_3$ | 291 | OF, OU | |
| | 1318 | OF, OU | |
| T-O-T | 108 | FF, B8, B32 | [28] |
| | 125 | FF, B8, B32 | |
| | 157 | FF | |
| | 176 | FF, B8, B32, CM8, M8, M40 | |
| | 199 | FF, B8, B32, CM8, M8, M40 | |
| | 267 | FF, B8, B32 | |
| | 285 | FF, B8, B32 | |
| | 330 | FF, B8, B32 | |
| | 372 | FF, B32 | |
| | 404 | FF, B8, B32, CM8, M8, M40 | |
| | 454 | FF, B8, B32, CM8, M8, M40 | |
| | 475 | FF, B8, B32, CM8, M8, M40 | |
| | 513 | FF, B8, B32, CM8, M8, M40 | |
| | 581 | FF | |
| | 629 | FF | |
| | 648 | FF | |
| | 749 | FF, B8, B32 | |
| | 811 | FF, B8, B32 | |
| | 895 | FF | |
| | 994 | FF | |
| | 1123 | FF | |
| | 1138 | FF | |

Table A.2.: List of all discovered ATR modes derived from non-used bed materials

| Modes | Wavenumber ($cm^{-1}$) | Samples | |
|---|---|---|---|
| $SiO_4$ | 616 | OF | [23] |
| | 836 | OF | [77] |
| | 875 | OF | [77] |
| | 984 | OF, OU | [23, 77] |
| | 1005 | | |
| CaO | 876 | OU | [12] |
| $OH^-$ | 3639 | | [12] |

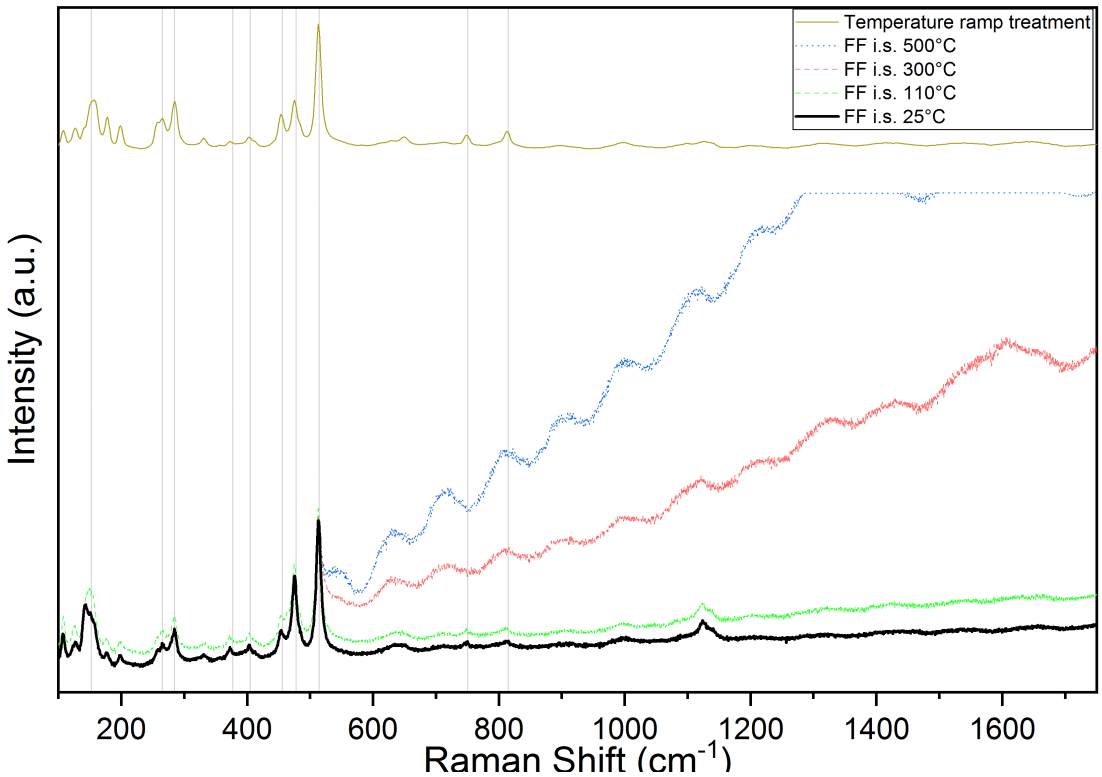


Figure A.4.: Temperature Treatment of the FF sample

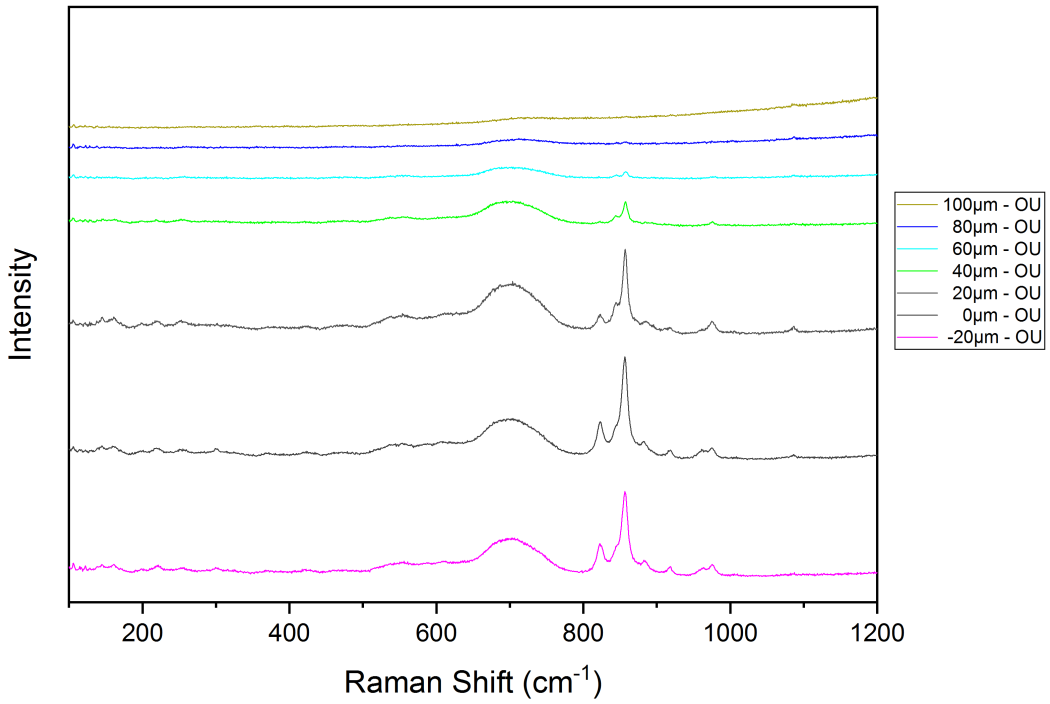


Figure A.5.: Confocal measurement of the OU sample in 20 µm steps

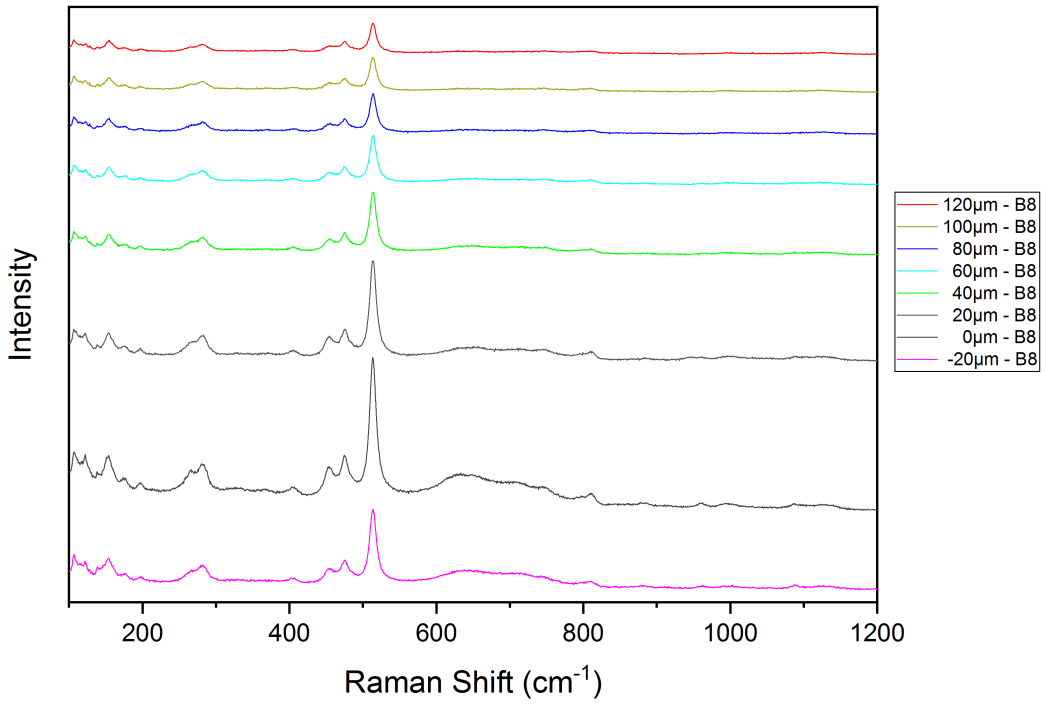


Figure A.6.: Confocal measurement of the B8 sample in 20 µm steps

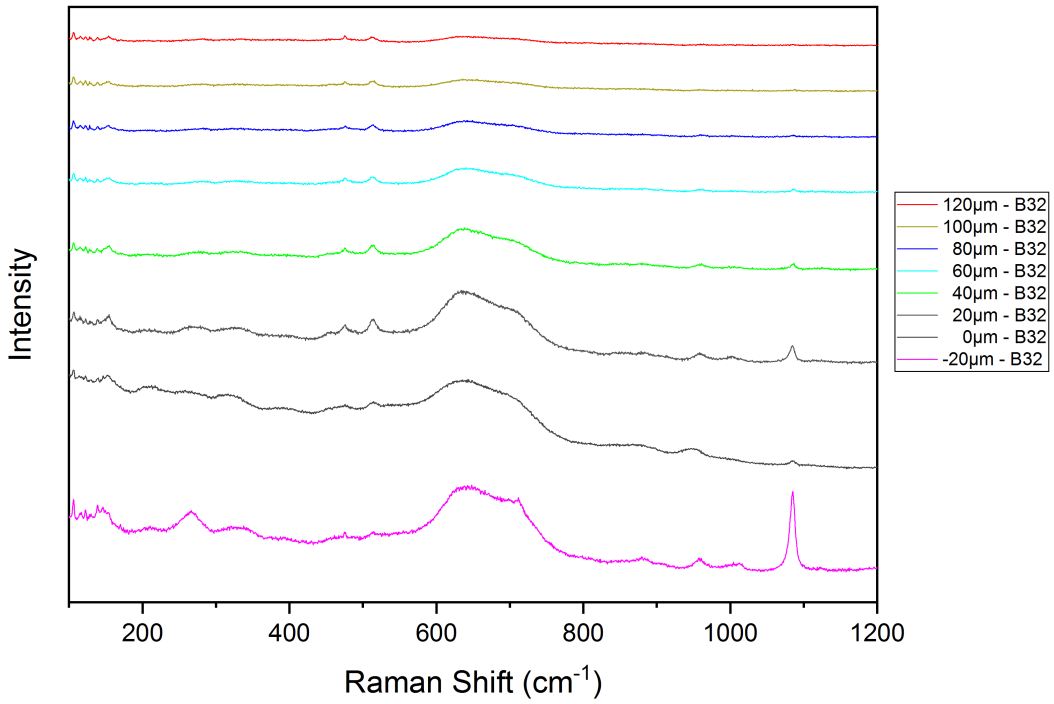


Figure A.7.: Confocal measurement of the B32 sample in 20 µm steps

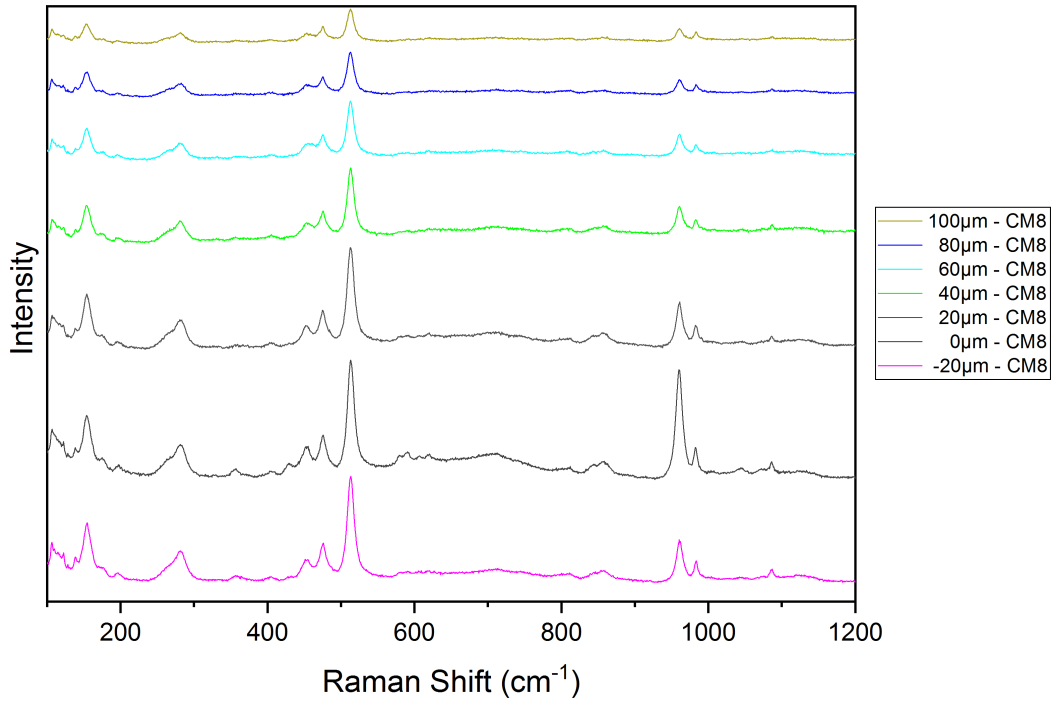


Figure A.8.: Confocal measurement of the CM8 sample in 20 µm steps

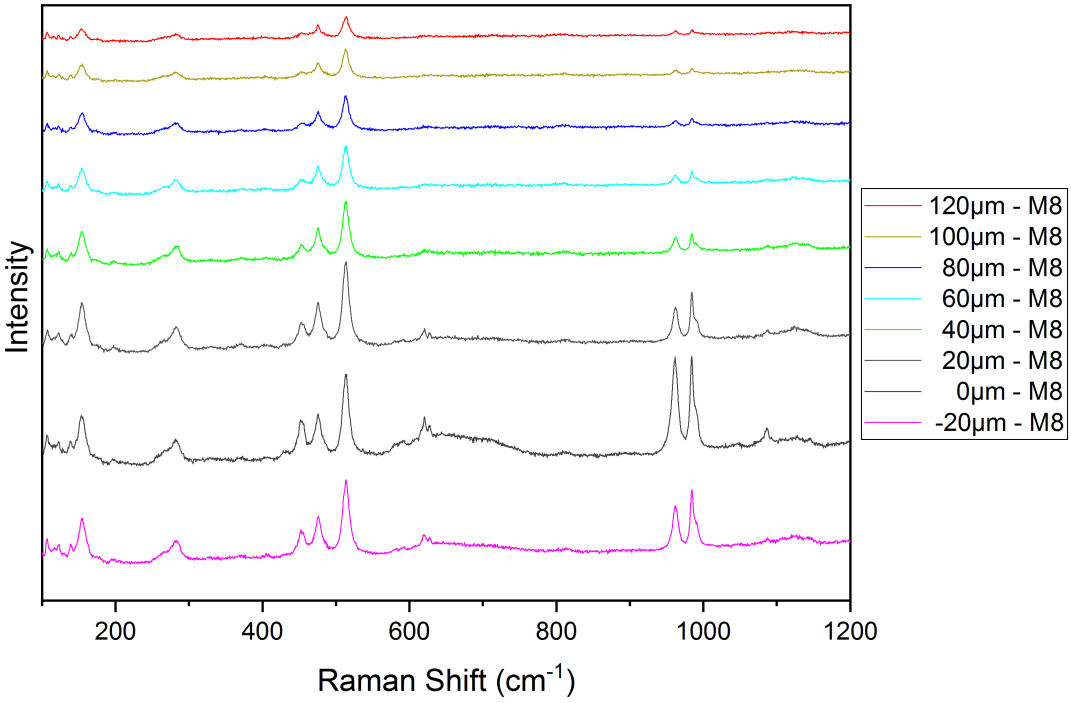


Figure A.9.: Confocal measurement of the M8 sample in 20 µm steps

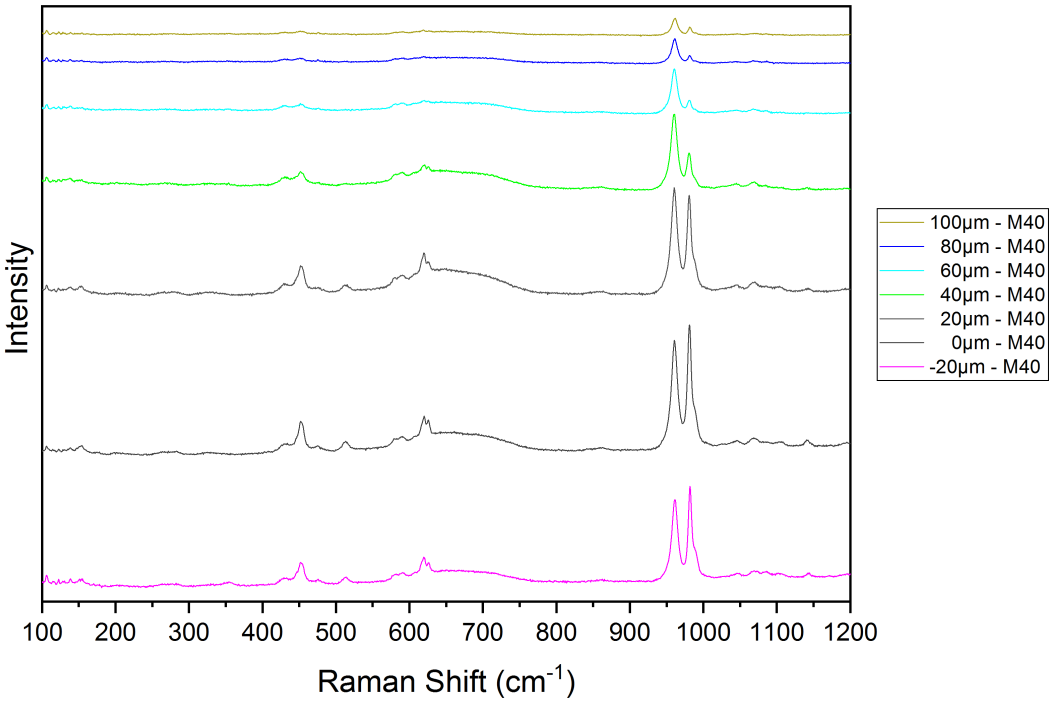


Figure A.10.: Confocal measurement of the M40 sample in 20 µm steps